EFFECT OF ICE ACCRETION SIMULATION FIDELITY ON LOW-REYNOLDS NUMBER SWEPT-WING AERODYNAMIC PERFORMANCE

STEPHANIE CHEN CAMELLO

A thesis
submitted in partial fulfillment of the
requirements for the degree of

Master of Science in Aeronautics & Astronautics

University of Washington
2017

Committee:
Michael B. Bragg
Christopher Lum

Program Authorized to Offer Degree:
Aeronautics & Astronautics

University of Washington

Abstract

EFFECT OF ICE ACCRETION SIMULATION FIDELITY ON LOW-REYNOLDS NUMBER SWEPT-WING AERODYNAMIC PERFORMANCE

Stephanie Chen Camello

Chair of the Supervisory Committee:
Dr. Michael B. Bragg
Aeronautics & Astronautics

Understanding how ice accretion affects the aerodynamics of swept-wing aircraft is a vital part of aircraft design, fabrication, and testing. Previous work focused on iced airfoil aerodynamics which did not take into account the geometric complexities of a swept wing. A method to create a series of full-span artificial ice shapes for a swept wing was developed so aerodynamic testing could be performed for a variety of ice shapes. Due to icing scaling limitations and icing wind tunnel size restrictions, ice accretions could not be produced for the full span of a swept wing. Instead, ice was accreted for small sections of the leading edge, laser scanned, and digitally manipulated to manufacture a full-span artificial ice shape. These full-span artificial ice shapes were used in low Reynolds number experimental testing. Wind tunnel testing was performed at Reynolds numbers of 1.8 x 10^6, 1.6 x 10^6, and 2.4 x 10^6 and Mach numbers of 0.09, 0.18, and 0.27, respectively, for model angles of attack ranging from -6° to 16°. The swept-wing model used was a scaled version of the NASA Common Research Model wing, which is representative of modern commercial airliner. Force balance, oil-flow visualization, fluorescent mini-tuft visualization, and surface pressure

data were collected for 18 leading-edge configurations including 7 high-fidelity ice shapes, 10 low-fidelity versions of these ice shapes, and the clean leading edge without artificial ice shapes present. The goal of this study is to determine how each artificial ice shape configuration affects the aerodynamic performance of the swept-wing model and the role ice shape simulation fidelity plays.

Acknowledgements

The success of this project was dependent on many people and I would like to extend a huge thank you to everyone that made this work possible. First, I want to thank my advisor, Dr. Michael Bragg, for not only the opportunity to participate in this project but also his continued guidance and support throughout both my undergraduate and graduate careers. I also want to acknowledge the FAA for their sponsorship of this work and Dr. Jim Riley and Tim Smith.

I want to thank Dr. Brian Woodard for initially getting me involved in this project and for all that he has taught me. Dr. Sam Lee and Dr. Andy Broeren from the Icing Branch at NASA Glenn Research Center were vital in the process of creating full-span ice shapes for wind tunnel testing and analyzing the aerodynamic performance results. Thank you to Dr. Sam Lee for spending countless hours teaching me Geomagic Studio and to Dr. Andy Broeren for helping me further understand the performance data.

I want to thank Chris Lum for organizing the manufacturing of artificial ice shapes and preparing them for the wind tunnel testing and the numerous undergrads, notably Kevin Ho, for pressure tapping and fit checking each removable leading edge to ensure the wind tunnel testing went smoothly. In addition, I want to thank Gustavo Fujiwara for his mentorship throughout my undergraduate and graduate studies, Jeff Diebold for sharing his vast knowledge on swept-wing icing with me, and Chris Triphahn for all his support

and teaching. Thank you to William Yoshida for providing me the pressure contour plots for aerodynamic performance analysis.

Finally, I want to thank my friends and fellow graduate students for their encouragement and making Seattle feel like home as well as my family: my parents, Bob and Shary, my grandma, Nancy, and my sister, Jennifer for your love and confidence in me. Thank you for being my inspiration.

Table of Contents

Nomenclature

α	Angle of attack
AoA	Angle of attack
AR	Aspect ratio
BL	Butt-line
c	Chord
CFD	Computational fluid dynamics
CRM	Common Research Model
$CRM65$	65% Scale Common Research Model
FAA	Federal Aviation Administration
FS	Fuselage station
IRT	Icing Research Tunnel
LWC	Liquid Water Content
MAC	Mean Aerodynamic Chord
$MCCS$	Maximum Combined Cross Section
MVD	Median Volume Diameter
$NASA$	National Aeronautics and Space Administration
$ONERA$	Office National d'Etudes et de Recherches Aérospatiales
T	Temperature
T_o	Stagnation temperature
V	Velocity

Chapter 1 Introduction

Ice accretion on aircraft during flight contribute to unfavorable conditions and their effect on the aerodynamic performance of swept-wings is not well understood. The majority of previous work studied the aerodynamic effects of ice accretion on airfoils, and it is important to continue research on swept-wings to improve the design, testing, and certification of aircraft [1,2]. These effects may be assessed through dry-air flights, which can be expensive, or CFD methods, which may not always be as accurate as experimental tests. As a result, the effects of ice accretion on aerodynamic performance of swept-wings are often assessed through aerodynamic wind tunnel tests. Further research on these effects will also help create more accurate computational prediction tools. This thesis is part of a collaborative research program involving NASA, the FAA, ONERA, the Boeing company, the University of Washington, and the University of Illinois Urbana-Champaign to better understand the effects of icing on swept-wing aerodynamics [3].

1.1 Experimental Ice Accretion Data

Experimental ice accretion data are obtained through icing wind tunnel testing. Icing wind tunnels reproduce conditions that an aircraft might encounter during flight through a uniform cloud. Parameters such as the liquid water content and water droplet size of the cloud can be controlled to simulate a wide variety of flight conditions. The icing wind tunnel used for this research project was the Icing Research Tunnel (IRT) at the NASA Glenn Research Center. The IRT has a 6 ft x 9 ft x 20 ft test section and can produce airspeeds from 50 knots to 350 knots and temperatures down to -25 °C [4].

1.2 Artificial Ice Shapes

Collecting aerodynamic data from a model with ice accretion in an icing wind tunnel is a difficult and impractical process. Therefore, to determine the performance of a swept-wing with ice accretion, replicas of the ice accretion geometries obtained from icing wind tunnel tests are required. These replicas are referred to as artificial ice shapes and exist for a variety of fidelities.

Ice shape fidelity provides an evaluation of the geometric features of artificial ice shapes. High-fidelity artificial ice shapes are direct replicas that maintain the highly detailed geometries of the original ice accretion such as scallops, roughness, and feathers. High-fidelity ice shapes can be created by methods such as molds and castings or a laser scanning process. Low-fidelity artificial ice shapes do not maintain the highly detailed features and may not be created directly from the original ice accretion geometry. Aerodynamic tests conducted on iced, swept-wings were previously only conducted using low-fidelity ice shapes.

One type of low-fidelity artificial ice shape is created by lofting 2D ice shape geometries from LEWICE 3D along the leading edge of a swept-wing. LEWICE 3D is a grid based code that outputs 2D ice shapes based on cloud properties such as droplet trajectories and heat transfer [5]. The process of creating low-fidelity ice shape geometries using LEWICE 3D for swept-wing aerodynamic testing is a well-researched and well-documented method [6,7,8]. Other methods for creating low-fidelity ice shapes for swept-wings include, but are not limited to, lofting through 2D cuts of the high-fidelity ice shape and filling in the gaps between scallops in the ice shape geometry. The process for creating low- and high-fidelity artificial ice shapes for both airfoils and swept wings will be further described in Chapter 2 and Appendices A and B.

1.3 Motivation, Objectives, and Approach

The goal of the overall research program is to study the aerodynamic effects of full-span, leading edge ice shapes on a swept-wing of a transport jet. Previous work focused on the aerodynamics effects of ice shapes on airfoils and did not take into account the 3D effects created from the twist, taper, sweep, and change in ice shape geometry along the leading edge of a swept wing. Another goal of this research program is to determine the amount of ice shape fidelity required to reproduce the same aerodynamic effects as the high-fidelity ice shapes. The specific objectives of the current study are to:

1. Develop a method to create a full-span ice shape from a limited set of experimental ice shape data.
2. Identify the differences in aerodynamic performance of low- and high-fidelity ice shapes.
3. Determine how ice shape fidelity affects the aerodynamic performance of the swept wing model.

To achieve the objectives of the current study, aerodynamic performance data previously collected from a swept-wing model with artificial ice shapes were used. This thesis is divided into three main chapters. The following chapter, Experimental Methods, discusses the classification of ice shapes, how full-span ice shapes representing a variety of these classifications were obtained for this research project, and the low Reynolds number testing conducted. The next chapter, Results and Discussion, presents aerodynamic data collected from wind tunnel testing and analyzes how low- and high-fidelity ice shapes affect the performance of the swept-wing model. The final chapter of this thesis is the Summary, Conclusions, and Recommendations which provides a summary of the work done and presents future work that could be conducted for the project.

Chapter 2 Experimental Methods

2.1 Background

Expanding the knowledge of how ice accretion affect aircraft aerodynamics is vital to the development of tools for aircraft design, testing, and certification. One way to achieve this is by documenting the different types of ice accretion geometries that may form during flight. Previous work focused on the aerodynamic effects of ice accretion on airfoils [1,2]. Because many studies have been conducted on iced-airfoil aerodynamics, research is expanding to the study of more three-dimensional geometries such as swept wings. Currently, minimal data exists for the flowfields of iced, swept wings due to their complexity. It is important to study 3D iced wings in addition to 2D iced airfoils as this more accurately represents the complexities.

2.1.1 Classification of ice shapes on 3D wings

The ice shape classifications on 3D wings were proposed by Diebold et al. [9], an extension of the work of Bragg et al. [10]. There were four main classifications of 3D ice shapes described by Diebold et al. [9]: roughness ice, horn ice, streamwise ice, and spanwise-ridge ice. Roughness ice occurs during the first few minutes of the accretion process. It is characterized by its ice roughness element height, density, and location along the airfoil surface. Roughness ice consists of a rough zone, feather region, and for some roughness ice shapes, a smooth zone. It was found that for swept wings with a large sweep angle, a smooth zone may not accrete [9].

Horn ice geometry is characterized by the ice height, angle with respect to the chord line, and location on the airfoil surface. 3D horn ice can be further divided into three subcategories: scallops, incomplete scallops, and no scallops [9]. Each one of these

subcategories may accrete on a swept wing depending on its sweep angle and the icing conditions it is exposed to. An illustration depicting these three types of swept-wing horn ice is shown in Fig. 2.1 [9].

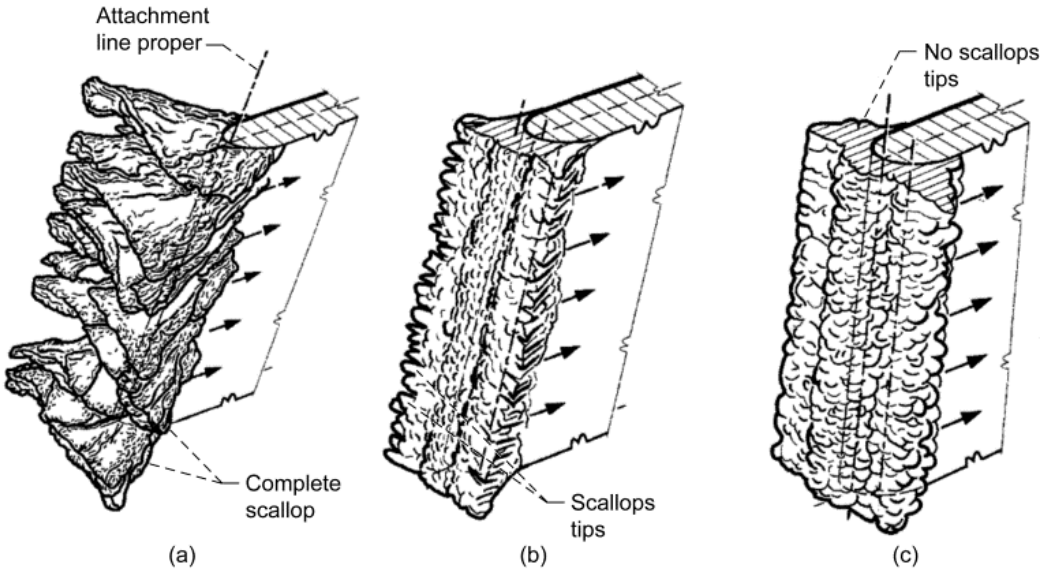

Fig. 2.1 Types of swept-wing horn ice. Courtesy of Diebold et al. [9]

Streamwise ice forms during rime icing conditions and follows the contour of the airfoil. Spanwise-ridge ice occurs further downstream from the leading edge and usually accrete due to the use of ice-protection systems.

2.1.2 Methods of creating artificial ice shapes

The development of artificial ice shapes is essential to the study of iced aerodynamics. Icing wind tunnels are not practical for aerodynamic testing, so replicas of the ice accretions produced from icing wind tunnel tests are created. These are referred to as artificial ice shapes. Artificial ice shapes can represent a variety of fidelities, a measurement of the geometric detail retained from the experimental ice accretion, but their goal is to accurately represent the flowfield of the original experimental ice accretion.

2.1.2.1 2D tracing method

This method was previously used to document simplified ice shape geometries. To make a 2D tracing, a heated metal sheet was used to melt through an experimental ice shape after accretion in an icing wind tunnel. The airfoil shape was cut out from the metal sheet to obtain the most accretion data in the tracing. The heated metal sheet was then replaced with a cardboard sheet of the same shape and a pencil was used to draw the outline of the ice accretion onto the cardboard [11]. This resulted in a simplified documentation of the ice accretion.

Fig. 2.2 Example of 2D tracing method. Courtesy of Lee et al. [12]

2.1.2.2 Mold and casting method

This method was previously used to create high-fidelity artificial ice shapes. High-fidelity artificial ice shapes retain the geometric detail of the original ice accretion including scallops, roughness, and feathers. The most recent mold and casting method was developed by Reehorst and Richter [13] and was often used at the IRT at the NASA Glenn Research Center. This method utilized molds created from ice accretions during icing wind tunnel tests which were then used to make artificial ice shape casts that could be used for testing in aerodynamic wind tunnels. This required making an extremely stiff mold in the low

temperatures of an icing wind tunnel that could only be used to create a single cast. Each mold and cast took a few hours to cure [11]. As a result, this was a tremendously time consuming process which only resulted in one copy of each documented ice accretion.

2.1.2.3 Laser scanning and rapid prototyping method

The laser scanning and rapid prototyping method is the current method used to create artificial ice shapes from ice accretions. This method is superior to both those previously mentioned because it provides a digital documentation of ice shapes that can be manipulated to create new ice shape geometries. A laser scanner, such as the Romer Absolute system [14] used by the NASA Glenn Research Center, is used to create a digitized point cloud of the ice accretion. This digitized point cloud can be made into a solid shape through 3D modeling programs, such as Geomagic Studio [15], which can then be rapid prototyped. This method is described in more detail by Lee et al. [12].

2.2 Acquiring ice accretion data for aerodynamic testing

In order to perform iced-aerodynamic wind tunnel tests, ice-shape geometries are required. Ice accretions for this project were obtained through icing wind tunnel tests at the NASA Glenn Research Center Icing Research Tunnel (IRT) which can simulate uniform cloud conditions during flight. Because the test section of the IRT is too small to fit a full-scale, swept wing of a transport jet, three spanwise locations of the leading edge were used to create ice accretions [17].

2.2.1 Common Research Model

For this research program, the wing of a 65% scale version of the Common Research Model (CRM65) was chosen as the baseline configuration [17]. The Common Research Model was designed in a previous program between NASA and the Boeing Company [18,19]

for CFD validation exercises. All the geometric data on the CRM are available to the public which made it an ideal candidate for this project.

A 65% scale version of the CRM (CRM65) was chosen to improve the confidence of accurately accreting full-scale ice accretions of the wing near the root where model blockage in the IRT would be the greatest. For simplicity, the 1-g wing loading was removed to eliminate the dihedral, thus resulting in a straight leading edge. Table 2.1 shows the CRM65 geometry compared to existing transport jets and Fig. 2.3 shows the CRM design without the engine nacelle and pylon.

Table 2.1 Summary of CRM65 geometry compared to similar aircraft. Courtesy of Broeren et al. [17]

Airplane	**Wingspan (ft)**	**Area (ft^2)**	**Sweep Angle, $c/4$ (deg)**	**AR**	**MAC (ft)**
CRM 65	125.3	1,745	35	9.0	15.0
Airbus A320	112.0	1,320	25	9.5	14.1
Boeing 737-800	112.6	1,341	25	9.5	13.0
Boeing 757-200	124.8	1,847	25	7.8	16.7

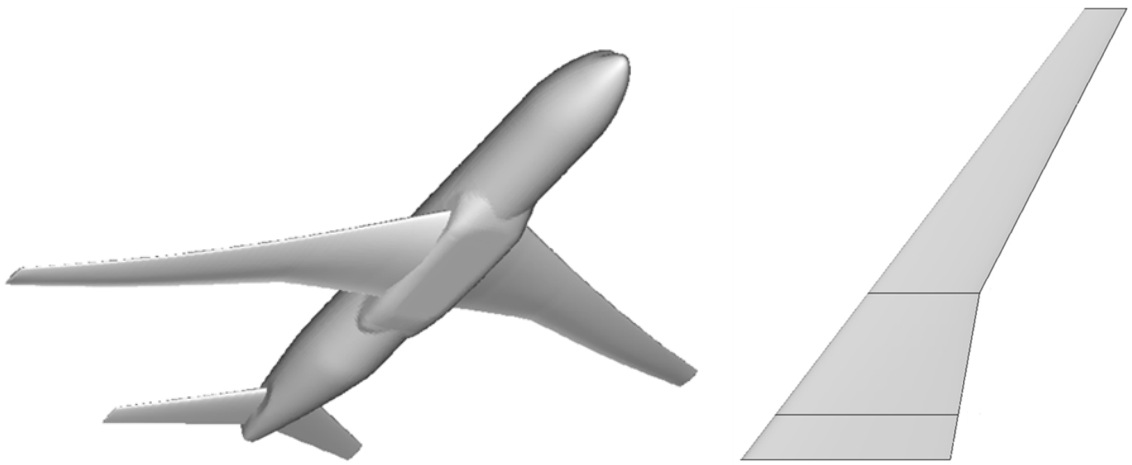

Fig. 2.3 a) CRM body without the engine and nacelle b) Semispan wing planform design. Courtesy of Broeren et al. [17]

2.2.2 Hybrid airfoils

Three spanwise locations on the CRM65 wing were tested and are referred to as the Inboard (η = 20%), Midspan (η = 64%), and Outboard (η = 83%). These locations were determined using LEWICE3D results and the selection process is described in more detail by Broeren et al [17]. Because the span of the full size CRM65 is much larger than the test section of the IRT, hybrid models were created for each of the three spanwise locations. Figure 2.4 shows the IRT test section compared to the full-scale CRM65 wing [20].

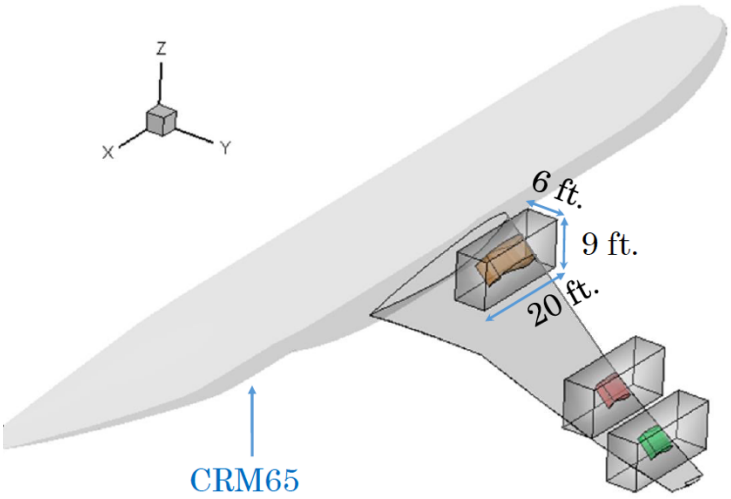

Fig. 2.4 IRT test section compared to the full-scale CRM65. Courtesy of Fujiwara et al. [20]

These hybrid models retain a full-scale leading edge but include a redesigned aft section with a truncated chord length. By retaining a full-scale leading edge and adding a flap, the flowfield produced at the leading edge is similar to the full-scale, free-air wing. This results in full-scale ice shapes, eliminating or reducing the icing scaling [21,22] required when the entire airfoil geometry is scaled to fit in the IRT. Fujiwara et al. [23] provides a more in depth discussion of the hybrid airfoil design process for swept wings. Figure 2.5 shows the hybrid model leading-edge normal cross sections at the chosen spanwise locations compared to the full-scale model.

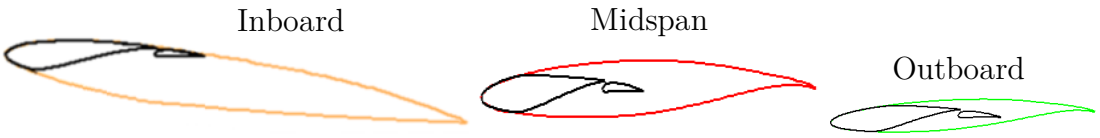

Fig. 2.5 Hybrid model airfoil section geometries compared to the full-scale sections. Courtesy of Fujiwara et al. [23]

2.2.3 IRT ice accretion data

Ice accretion testing was conducted in the IRT at a variety of cloud conditions for all three hybrid models. Broeren et al. [24] described the testing process and ice accretion results in further detail. From these results, seven ice accretions were chosen for aerodynamic testing to represent a large range of the ice accretion classifications previously described. The ice accretions for each of these cases were documented using the laser scanning method previously described. Only the center 1 ft. span of each hybrid model was scanned. Digitally capturing more than this area would have been prohibitively time consuming and, due to the hybrid model design, the flowfield outside the center 1 ft. span was not necessarily representative of the full-scale wing. This provided a digital database of the experimental ice accretions. Table 2.2 summarizes these ice accretions and the IRT cloud conditions used to create them [25].

Table 2.2 Summary IRT cloud conditions. Adapted from Camello et al [25]

Run ID	**T_0 (°C)**	**V (kts)**	**MVD (μm)**	**LWC (g/m^3)**	**AoA (deg)**	**t (min)**
Venetian Blind	-3.8	130	25	1.0	3.7	29
Maximum Scallop	-6.3	130	25	1.0	3.7	29
Small Gap Scallop	-8.7	130	25	1.0	3.7	29
Incomplete Scallop	-11.2	130	25	1.0	3.7	29
Streamwise/Rime	-17.9	130	25	0.6	3.7	23
Maximum Scallop Low AoA	-6.3	130	25	1.0	2.1	29
WB33	-3.1	130	25	0.9	3.7	49

The maximum combined cross section (MCCS) method was developed to use the laser scanned data on 3D ice accretions to generate and compare 2D cross sections of

digitally processed ice shapes. In addition to comparing one laser scanned ice shape to another, the MCCS can be used to compare to LEWICE3D [16] results. To obtain the 2D cross section using this method, 30 normal cuts of the ice accretion were made perpendicular to the leading edge of the wing model 0.2 inches apart. The series of cuts were plotted in two-dimensions and the outer boundary of the geometry was defined. This is the MCCS geometry. This method is similar to the 2D tracing method in that it broadly defines the outline of an ice accretion. The process of creating a MCCS is shown in Fig. 2.6. Images of the IRT ice accretions [25] and the MCCS for the Midspan station for these selected conditions are shown in Figs. 2.7-2.13. A comparison between the MCCS of all the ice shapes is shown in Fig. 2.14.

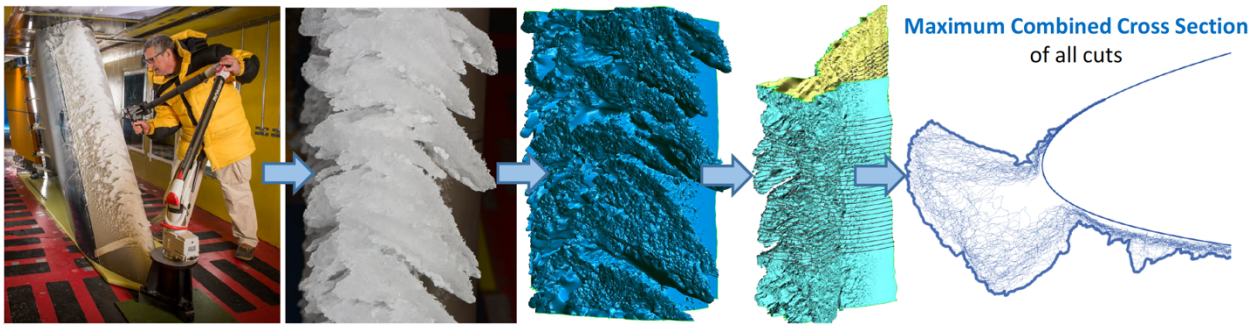

Fig. 2.6 Process of creating a MCCS. Courtesy of Fujiwara et al. [20]

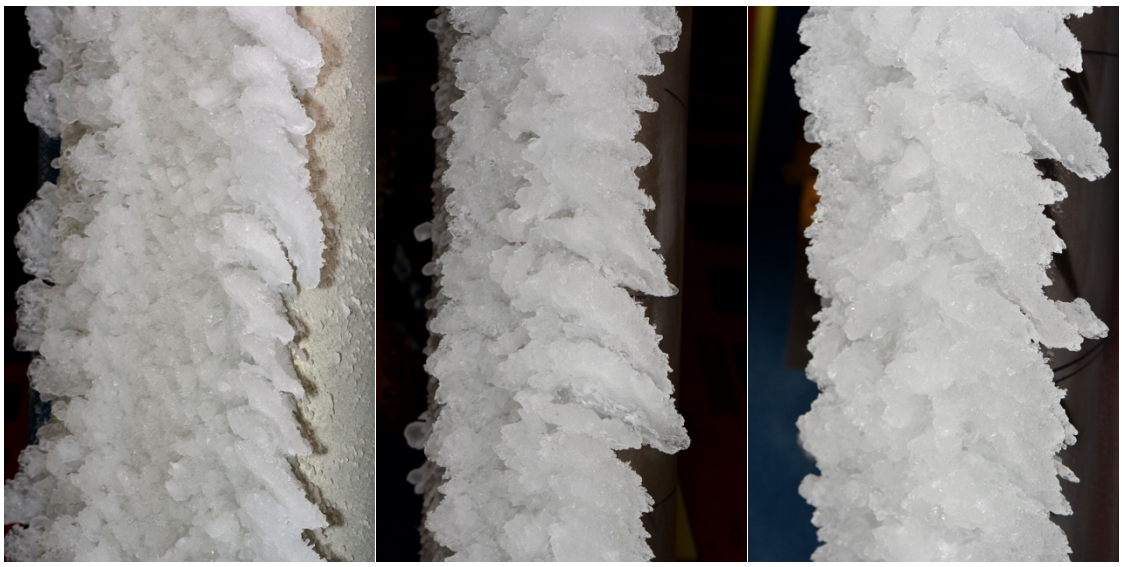

a) Inboard, Midspan, and Outboard model ice accretions, respectively courtesy of Camello et al. [25]

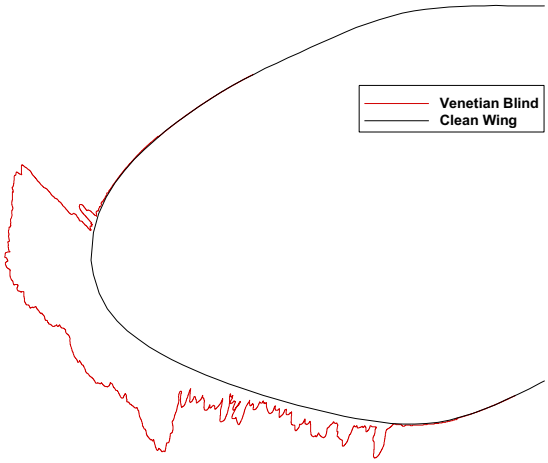

b) Midspan ice accretion MCCS.

Fig. 2.7 Venetian Blind ice accretion.

a) Inboard, Midspan, and Outboard model ice accretions, respectively courtesy of Camello et al. [25]

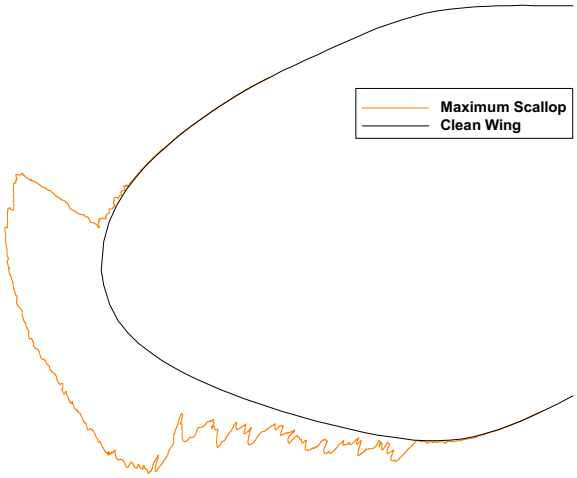

b) Midspan ice accretion MCCS.

Fig. 2.8 Maximum Scallop ice accretion.

a) Inboard, Midspan, and Outboard model ice accretions, respectively courtesy of Camello et al. [25]

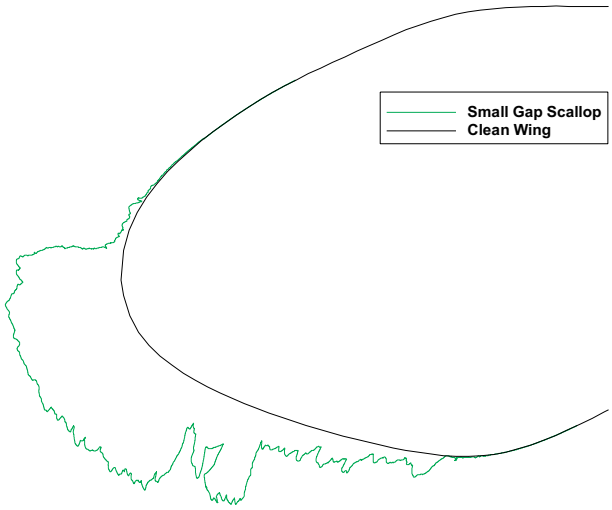

b) Midspan ice accretion MCCS.

Fig. 2.9 Small Gap ice accretion.

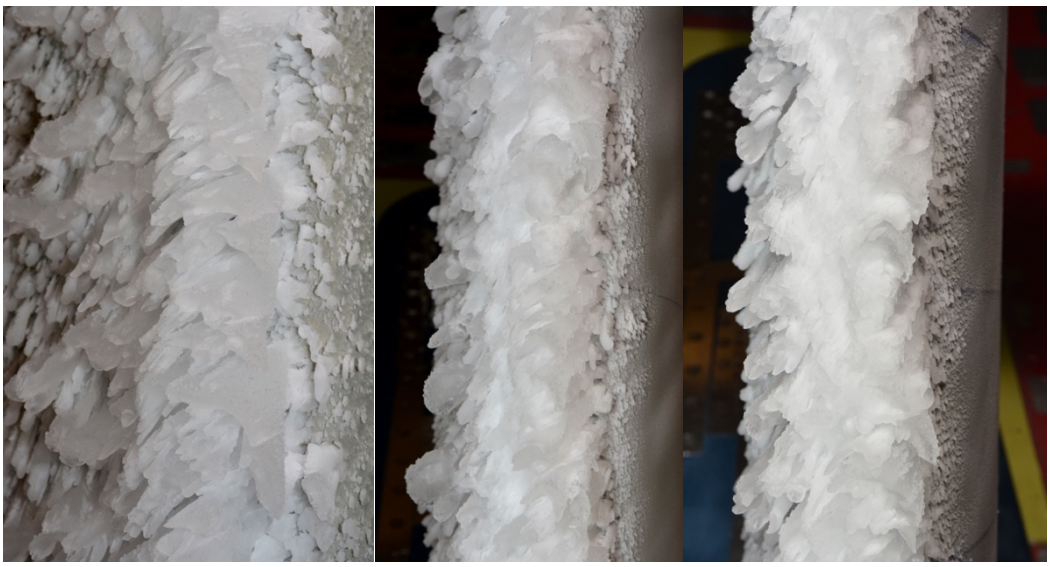

a) Inboard, Midspan, and Outboard model ice accretions, respectively courtesy of Camello et al. [25]

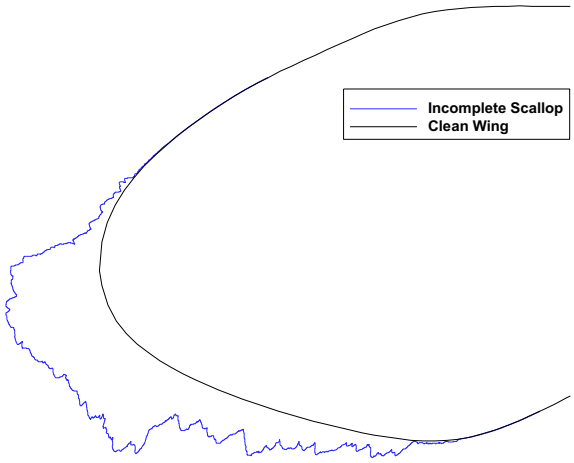

a) Midspan ice accretion MCCS.

Fig. 2.10 Incomplete Scallop ice accretion.

a) Inboard, Midspan, and Outboard model ice accretions, respectively courtesy of Camello et al. [25]

b) Midspan ice accretion MCCS.

Fig. 2.11 Streamwise/Rime ice accretion.

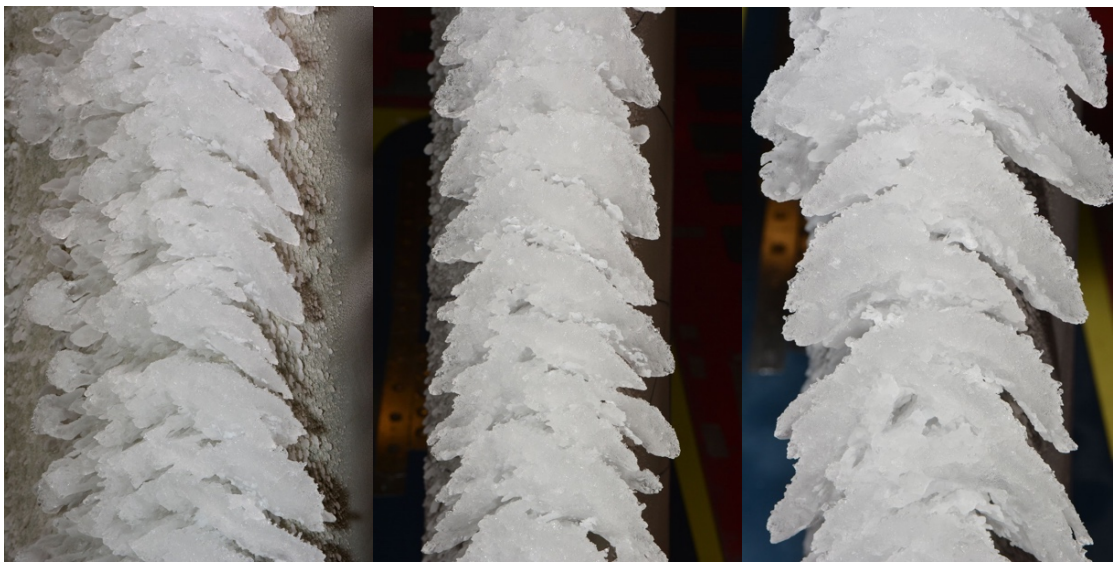

a) Inboard, Midspan, and Outboard model ice accretions, respectively courtesy of Camello et al. [25]

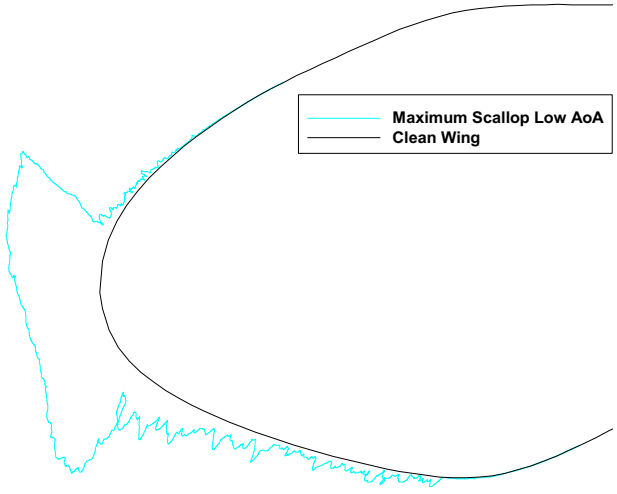

c) Midspan ice accretion MCCS.

Fig. 2.12 Maximum Scallop Low AoA ice accretion.

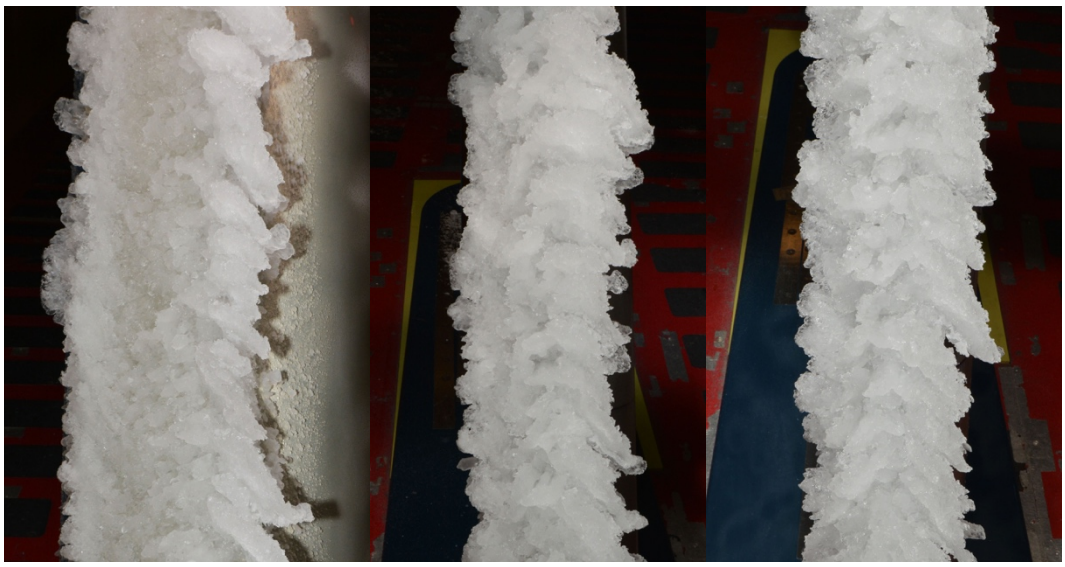

a) *Inboard, Midspan, and Outboard model ice accretions, respectively courtesy of Camello et al. [25]*

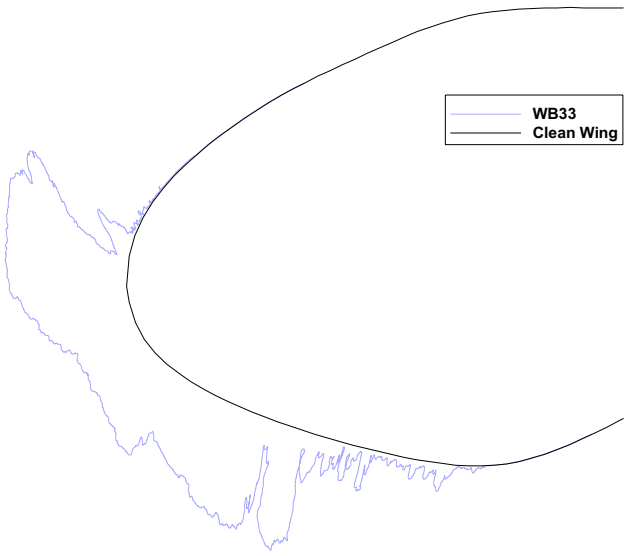

b) Midspan ice accretion MCCS.

Fig. 2.13 WB33 ice accretion.

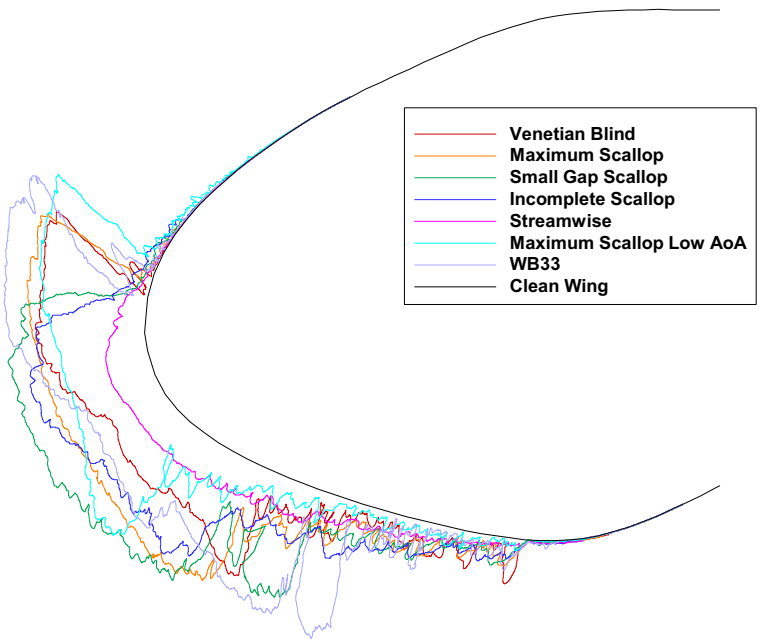

Fig. 2.14 Comparison of MCCS for Midspan ice accretion.

A comparison of the MCCS for the high-fidelity ice shapes in Fig. 2.14 shows 3 main groups of ice shape geometries. The Streamwise ice shape remained closest to the geometry of the leading edge of all the ice shapes while the Venetian Blind, Maximum Scallop, Maximum Scallop Low AoA, and WB33 ice shapes extended towards the upper surface the most. Both the Small Gap Scallop and Incomplete Scallop ice accretion geometries were between the Streamwise ice shape and the larger scalloped ice accretion geometries.

2.3 Generating full-span ice shapes

2.3.1 Digitally documenting and post processing ice accretion

The process of digitally documenting ice accretion using a laser scanner was developed by Lee et al. [12]. They implemented the same test procedure in the IRT for a variety of commercially available laser scanners and determined that the articulated-arm system of the Romer Absolute SI [14] was best suited for the future development of the IRT. The following process was used to digitally document ice accretions in the IRT:

- Accrete ice on the hybrid model
- Photograph the ice accretion
- Spray the ice accretion with white paint
- Determine reference points to orient the digital ice shape
- Scan the ice accretion

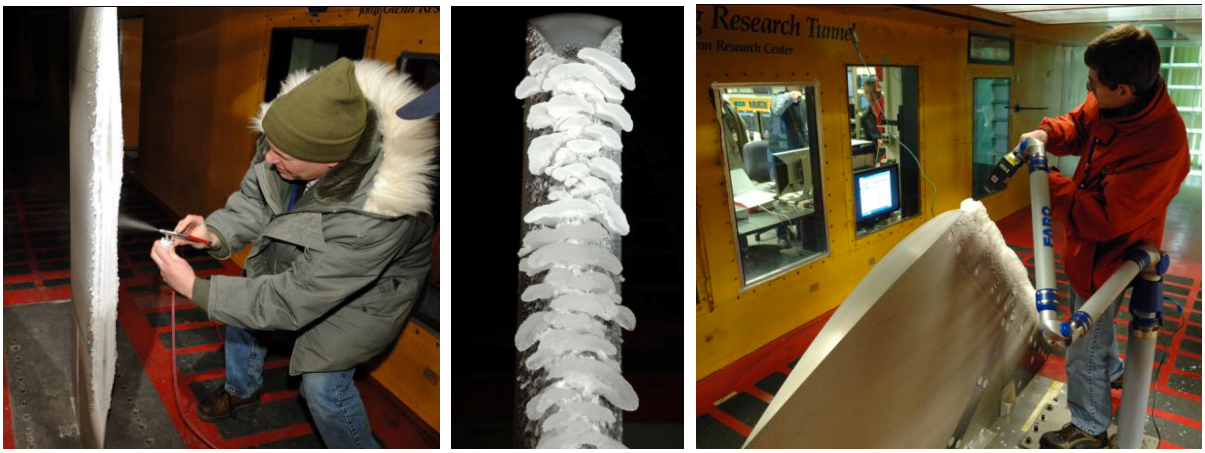

Fig. 2.15 Digital documentation of ice shapes. Courtesy of Lee et al. [26]

Once a data point cloud was obtained from the laser scan, it was post processed to create a watertight, or fully closed, surface while maintaining the complex geometry of the original ice accretion. To accomplish this task, the Geomagic software package was chosen. [25] It is able to post-process irregular and complicated surfaces and create geometries that are compatible with many different rapid prototyping processes.

To create a watertight ice shape surface, the laser scan data were post processed. Because the laser scanning method was not perfect and the ice shape was scanned in multiple passes, there were holes in the data as well as overlapping data. These defects were eliminated before the ice shape geometry was further manipulated. The steps taken to process the data are outlined below.

- Start with ice shape scan data from IRT tests
- Align the series of scans
- Reduce the number of data points – much more detail is scanned than can be realistically rapid-prototyped
- Evenly distribute data points along the ice shape surface

- Create a triangular mesh from the data points to create a surface
- Fill in holes in data to create a water-tight mesh until the ice shape is a single, continuous surface

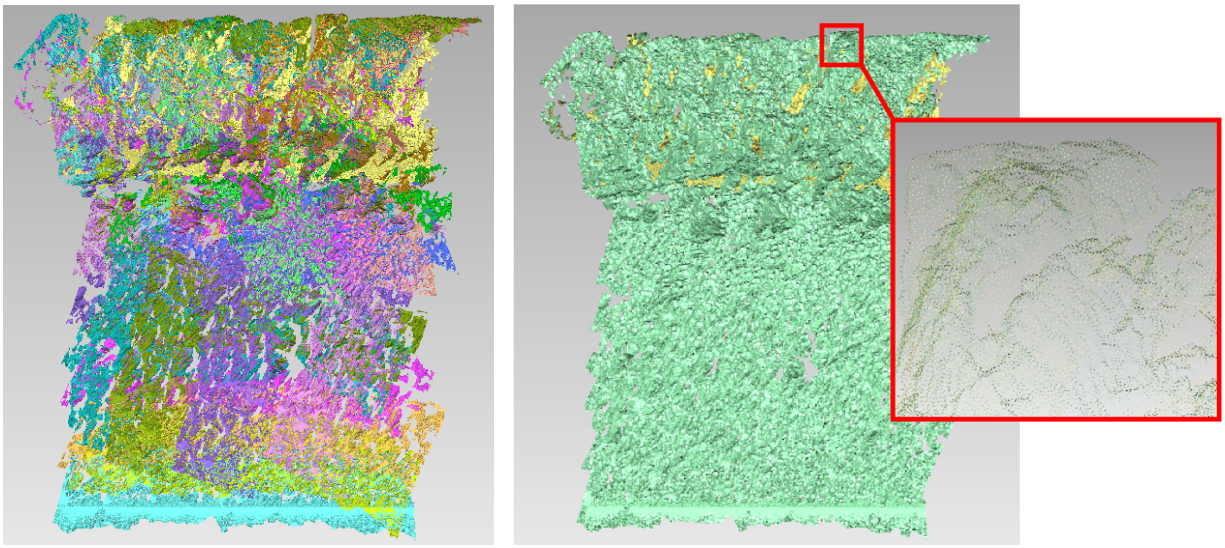

a) *b)*

Fig. 2.16 a) Raw ice shape laser scan data b) Reduced and evenly distributed data points of ice shape geometry.

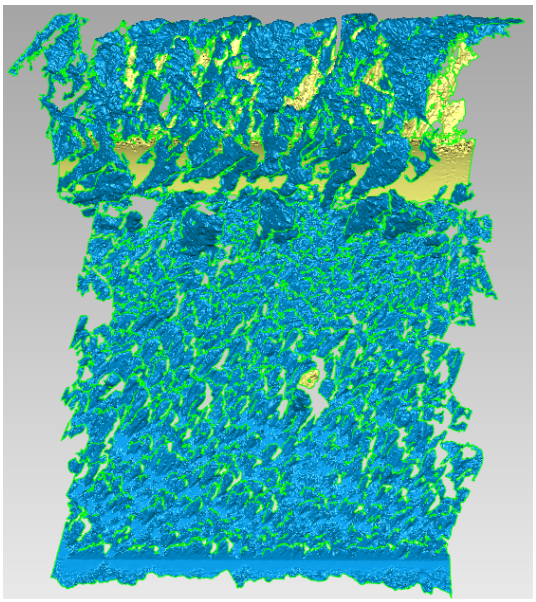

Fig. 2.17 Triangular mesh created from data points.

Once a triangular mesh was generated, Geomagic Studio differentiated between the inner surface and the outer surface of the ice shape by labeling them yellow and blue,

respectively. In Fig. 2.17 the surface showed many visible yellow areas and gaps that needed to be filled to create a single, continuous surface. This was done using a series of functions in Geomagic Studio. For completely separated sections, two bridges were created to connect the mesh of the separated piece to the mesh of the main ice shape as shown in Fig. 2.18. This created a closed off area that was filled with the hole-filling function which placed a mesh over an enclosed area with triangles tangent to its parent triangles at the edges so it followed the correct contour over the hole.

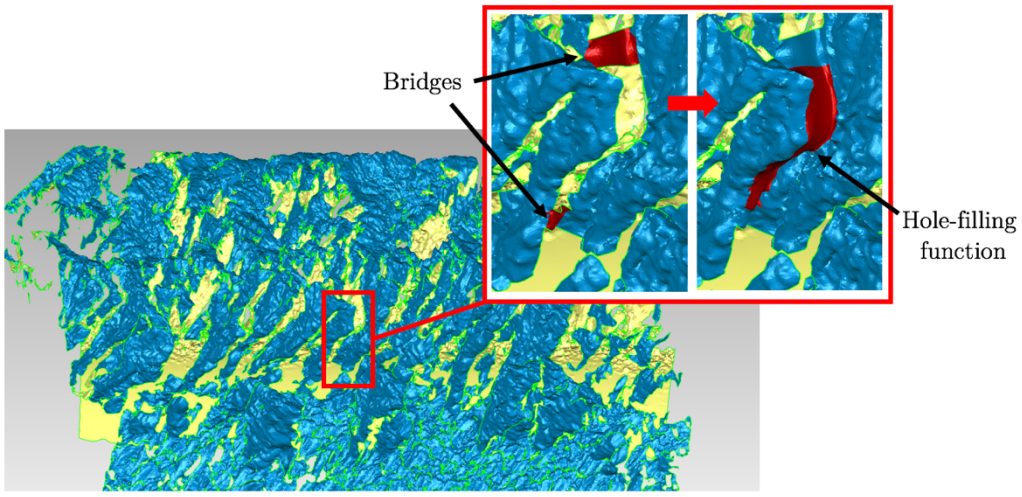

Fig. 2.18 Reattaching separated sections of a scanned ice shape.

Once all the separate pieces were combined, a built-in function in Geomagic studio, the "Mesh Doctor", was used to eliminate some imperfections. However, many of these problem areas needed to be fixed by hand which was an extremely time consuming process. Once a single, continuous surface of the ice shape was created, the edges of the geometry were trimmed to eliminate rough edges. This ice shape could now be used for interpolation.

Both the laser scanning and digital processing methods were validated by Monastero [11]. An example of an IRT ice accretion compared to its laser scanned, digitally processed ice shape counterpart is shown in Fig 2.19.

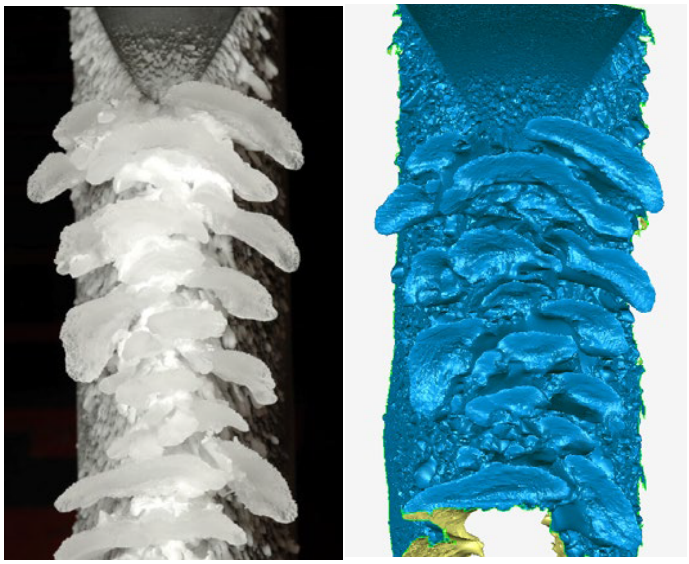

Fig. 2.19 Real ice shape compared to digitized ice shape. Courtesy of Lee et al. [12]

2.3.2 Method to create full-span ice shapes

Previous artificial ice shapes for aerodynamic testing were based on methods created for airfoils and straight wings, and did not allow for any twist or taper of the wing [26]. A spanwise segment of the ice accretion was extruded to cover the span of the aerodynamic model which resulted in a quasi-2D ice shape. This extrusion method included local variations in the geometry, but it could still be considered two-dimensional in an overall sense. While this process may work for straight wings, this research utilizes a swept wing and requires a full-span ice shape for aerodynamic testing of the CRM65.

Generating a full-span ice shape for a swept wing is a much more complex process than generating a full-span ice shape for a straight wing because the leading edge changes along the span in size and orientation due to twist and taper. Furthermore, the ice shape geometries vary greatly between the root and the tip because the geometry and local flowfield changes along the span of swept-wings. Appendices A and B detail the process used to create full-span ice shapes for a swept-wing using the Geomagic software package.

2.3.2.1 Method to create a high-fidelity, full-span ice shape

The full-span ice shapes were derived from the full-scale ice accretions obtained from the hybrid airfoil models. The hybrid airfoil models represent three locations on the wing of the CRM65: the Inboard, the Midspan, and the Outboard. Because these three locations only account for a fraction of the CRM65 wing span, the geometries for the areas between the wing root, these three locations, and the wing tip were interpolated or extrapolated from the existing ice accretion data. It is vital that these interpolated and extrapolated ice shapes retain similar geometric characteristics to the ice shapes they were derived from because they account for such a large fraction of the wing span.

An interpolation method was developed to obtain ice shape geometries between the scanned sections of the Inboard, Midspan, and Outboard full-scale ice shapes. The following steps summarize this process:

- Eliminate any poorly scanned sections near the edges of the ice shape
- Apply Geomagic's weighted averaging function between two ice shapes
- Repeat weighted averaging until the span between the original two ice shapes is filled and there is a smooth transition

The weighted averaging function allowed the creation of a new, averaged ice shape. To achieve this, copies of an ice shape were created to produce the specific amount of weighting. For example, five copies of the Midspan ice shape and one copy of the Outboard ice shape were used in a 5:1 averaging to create "Interpolated Ice 1" shown in Fig 2.20b). [25] This type of weighting resulted in an ice shape the was much closer in geometry to the Midspan ice shape than the Outboard ice shape. To create "Interpolated Ice 2", five copies of "Interpolated Ice 1" were averaged with one copy of the Outboard ice shape. This process was repeated to obtain all the ice shape geometries between the Inboard ice shape and the Outboard ice shape as shown in Fig. 2.20d).

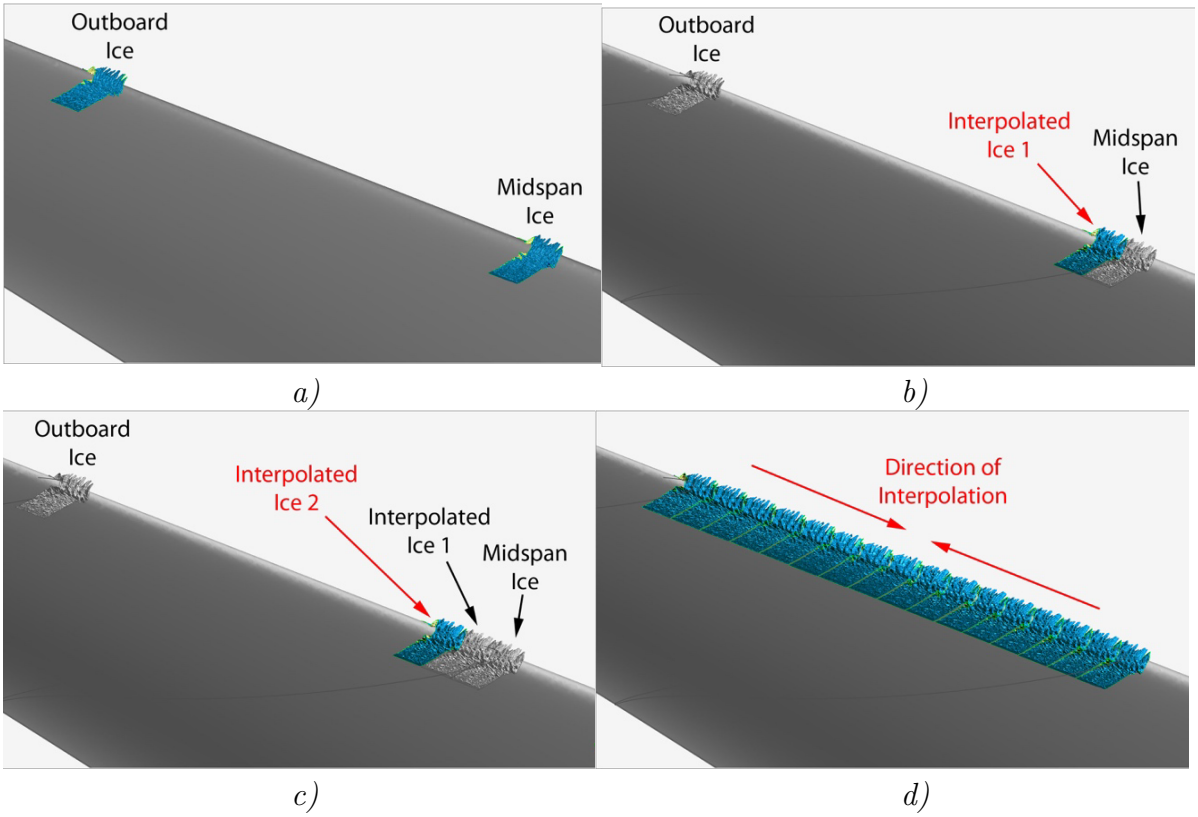

Fig. 2.20 Summary of ice interpolation process. Courtesy of Camello et al. [25]

An extrapolation method was developed to obtain the ice shapes between the wing root and Inboard ice, and the Outboard ice and the wing tip. Because experimental ice accretions did not exist for the tip and the root of the CRM65 wing, these ice shapes were created by modifying the Inboard and Outboard ice shapes using LEWICE3D results as a guide. LEWICE3D results were not available for conditions for all the experimental ice accretions, and the results from the CRM65 wing-body for WB33T-13 [24] were used to determine the horn height and thickness of ice at the tip and root of the wing. These results are shown in Fig. 2.21 [25].

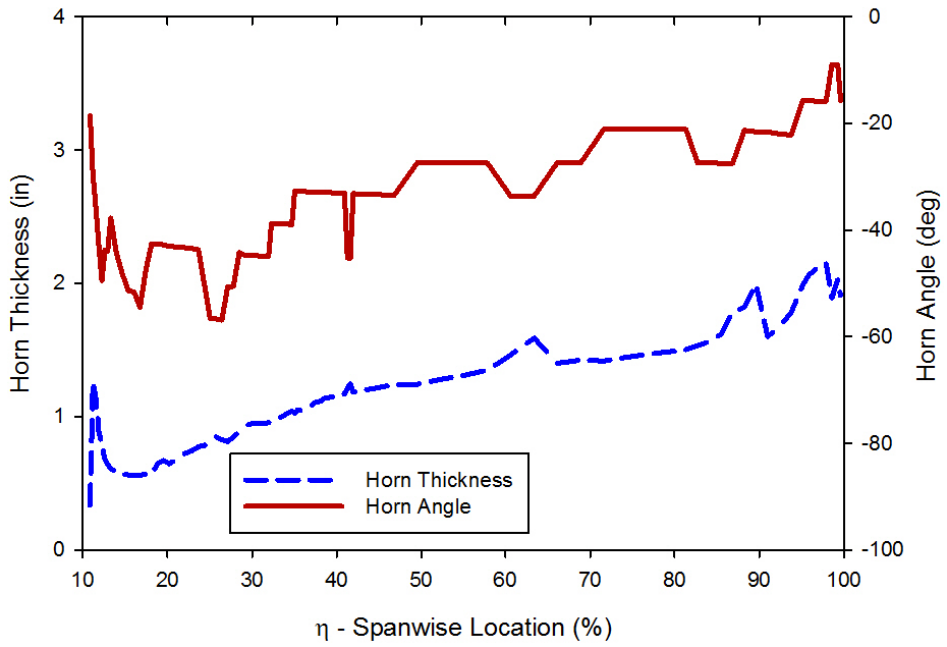

Fig. 2.21 LEWICE3D computational ice accretions for the CRM65 at WB33T-13. Courtesy of Camello et al. [25]

These results provided a target horn thickness and angle for the root and tip ice shapes. An example of the process to create a tip ice shape is shown in Fig. 2.22. [25] A copy of the Outboard station ice shape was translated to the tip of the CRM65 wing geometry. In Fig. 2.22a) The Outboard copy was translated away from the leading edge to increase the horn thickness according to the LEWICE3D results. In Fig. 2.22b), the translated copy was rotated to a high horn angle.

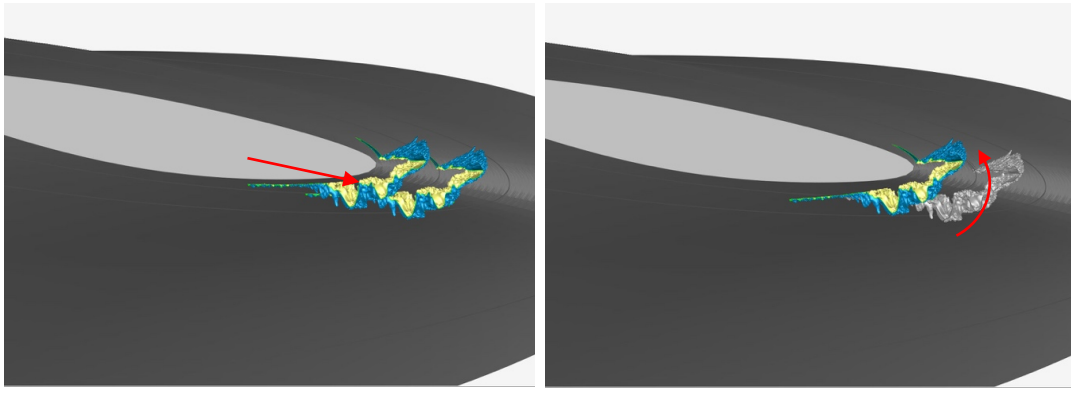

a) *b)*

Fig. 2.22 Determining horn thickness and angle of the tip ice shape. Courtesy of Camello et al. [25]

Because the radius of the wing leading edge at the tip is smaller than the radius at the Outboard station, the copy of the Outboard ice shape was split at the locations depicted in Fig. 2.23b). These locations were chosen because they were downstream of the main ice shape geometry. The downstream sections were translated until they were flush with the surface of the leading edge. Finally, the sections were reattached using the previously described bridge and hole filling process. The same process was applied to obtain the root ice shapes.

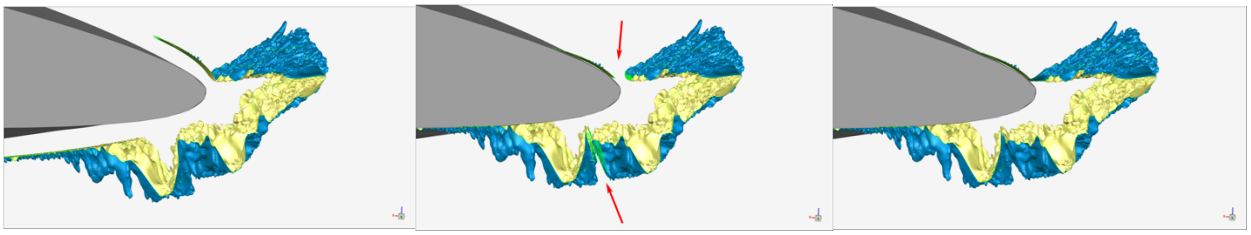

a) *b)* *c)*

Fig. 2.23 Fitting the tip ice shape to the wing leading edge. Courtesy of Camello et al. [25]

Once the geometries were obtained for the root and tip ice shapes, the interpolation process previously described was applied. This created a series of separate ice shapes with a gap between them as shown in Fig. 2.24.

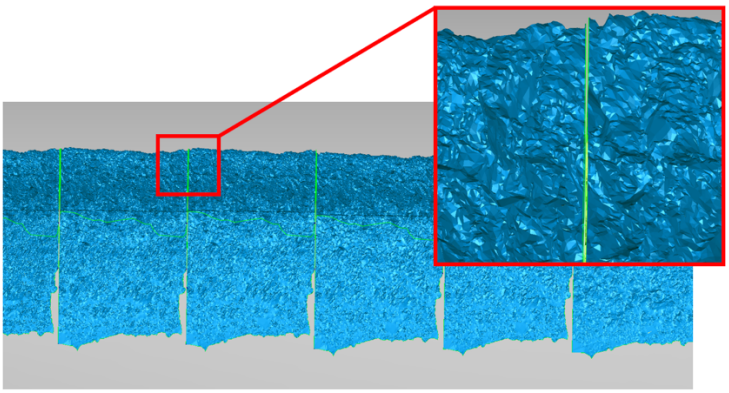

Fig. 2.24 Gaps between interpolated ice shapes

To create an artificial, full-span ice shape that could be rapid prototyped, the ice shape geometries must be a continuous surface. The separate interpolated ice shapes were attached to each other using the bridge and hole-filling process previously described. This process was repeated for the extrapolated ice shapes to result in a full-span, leading edge ice shape. At this point, the ice was only a surface and not a solid object so it need to be attached to the leading-edge of a wing model before it could be rapid-prototyped.

2.3.2.2 Method to create a low-fidelity, full-span ice shape

Low-fidelity ice shapes are ice shape geometries that do not retain the highly detailed features of high-fidelity ice shapes such as roughness, feathers, or scallops. Several methods to create low-fidelity ice shapes currently exist. The methods developed for this research were used to generate 2D smooth and 2D smooth with grit roughness low-fidelity ice shapes based on a high-fidelity ice shape geometry.

To create a 2D smooth low-fidelity version of a high-fidelity ice shape, a series of three 2D cuts were created perpendicular to the leading edge over a small area of the span of the high-fidelity ice shape. The cuts were made approximately 1 inch apart to capture any spanwise variations of the high-fidelity ice shape. A simple, smoothed outline was then created from these three cuts by placing a spline along key features of the geometry. An

example of the smoothed outline compared to the three 2D cuts is shown in Fig. 2.25. The smoothed outlines were created along the span of the ice shape until there were enough cuts to loft to create a full-span, 2D smooth ice shape.

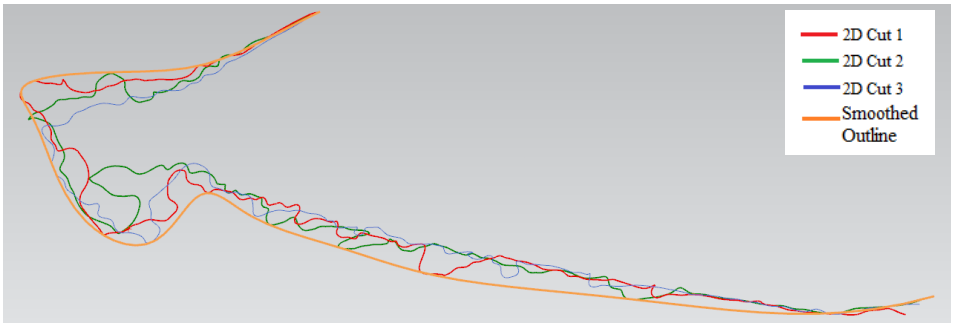

Fig. 2.25 Example of 2D smoothed outline. Courtesy of Camello et al. [25]

To create a 2D smooth with grit roughness low-fidelity ice shape, silicon carbide 60-grit was adhered to the leading edge of an existing 2D smooth low-fidelity rapid prototyped ice shape using double-sided tape. An example of a 2D smooth with grit roughness low-fidelity ice shape is shown in Fig. 2.26.

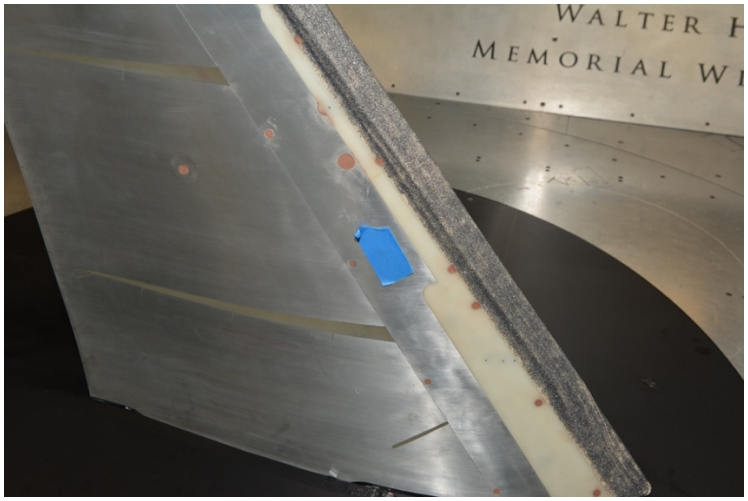

Fig. 2.26 2D smooth ice shape with grit roughness applied

2.4 Low Reynolds number wind tunnel testing

2.4.1 Wind tunnel facility

Low Reynolds number wind tunnel tests were performed at the Walter H. Beech Wind Tunnel at Wichita State University to determine the aerodynamic effects of ice shapes on the CRM65 wing. This wind tunnel contains a 7 ft x 10 ft test section and is an atmospheric, closed-return type, subsonic wind tunnel. A summary of approximate maximum flow values for test section of this wind tunnel is shown in Table 2.3 [27].

Table 2.3 Summary of Walter H. Beech Wind Tunnel maximum flow values [27]

Measurement	Maximum value
Speed	350 ft/s
Reynolds number	1.8×10^6 per ft
Dynamic pressure	125 psf

A 6-component pyramidal style force balance was used to obtain load measurements during the wind tunnel tests. [16] It measured the normal and axial forces on the model and a coordinate rotation was utilized to determine the lift and drag in the wind axes. [27] The range of this force balance is summarized in Table 2.4.

Table 2.4 Range of the force balance in the Walter H. Beech Wind Tunnel [27]

Measurement	Range
Normal force (F_N)	±1984 lb_f
Axial force (F_A)	±794 lb_f
Moment (M_{bal})	±839 lb_f -ft

An Esterline miniature electronic pressure scanning module (ESP-32HD) was used to acquire surface pressures from the surface pressure taps on the model.

2.4.2 Scaled CRM65 swept-wing model

An 8.9% scale model of the CRM65 wing with the 1-g cruise condition loading removed was designed for low-Reynolds number wind tunnel testing [28]. The model parameters and dimensions are shown in Table 2.5 and Fig. 2.27.

Table 2.5. Parameters of the 8.9% scale model of the CRM65 [28]

Wing Parameter	Value
Span	5.00 ft (60.0 in)
MAC	1.39 ft (16.67 in)
Area	6.01 ft^2 (865.3 in^2)
Volume	0.617 ft3 (1069 in3)
Aspect ratio	8.30
Taper ratio	0.23
Root chord	2.25 ft (27.0 in)
Tip chord	0.52 ft (6.20 in)
Root AoA	4.40 deg
Tip AoA	-3.80 deg
1/4-chord sweep angle	35.0 deg
Leading edge sweep angle	37.2 deg

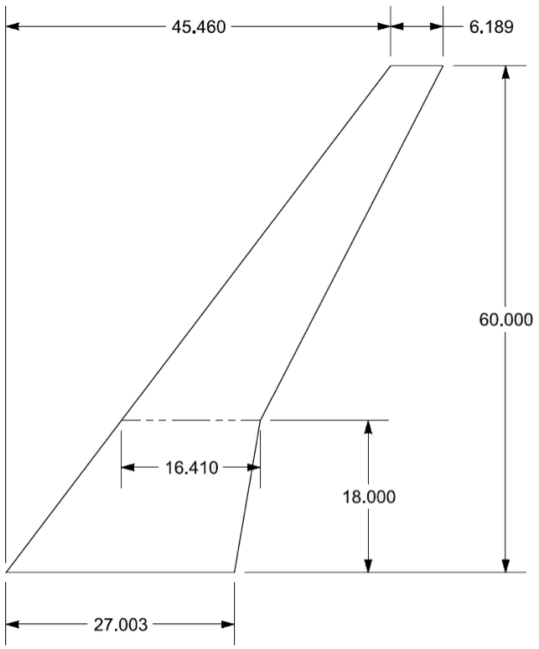

Fig. 2.27 8.9% scale model of the CRM65 dimensions in inches [28]

Because there were many ice shape geometries to be tested, the subscale model was designed with a removable leading edge that could be interchanged with the rapid-prototyped ice shapes. The main wing model and the clean leading edge without a full-span ice shape geometry were machined from aluminum, while the various iced leading edges with a full-span ice-shape geometry were rapid prototyped from SomosNeXt [29] material. The full-scale ice-shape geometries were scaled and merged with a CAD model of the clean leading edge using a processed developed in Geomagic Studio [15].

Surface pressure tap holes with a diameter of 0.036" were placed in the iced leading-edge geometry using Geomagic Studio before they were rapid prototyped for wind tunnel testing. Although the clean wing model has a total of 219 pressure tap locations, the pressure taps directly on the ice geometries of the iced leading edges were removed due to the complexity of the ice shapes. The removable leading-edge feature and pressure tap locations are shown in Fig. 2.28.

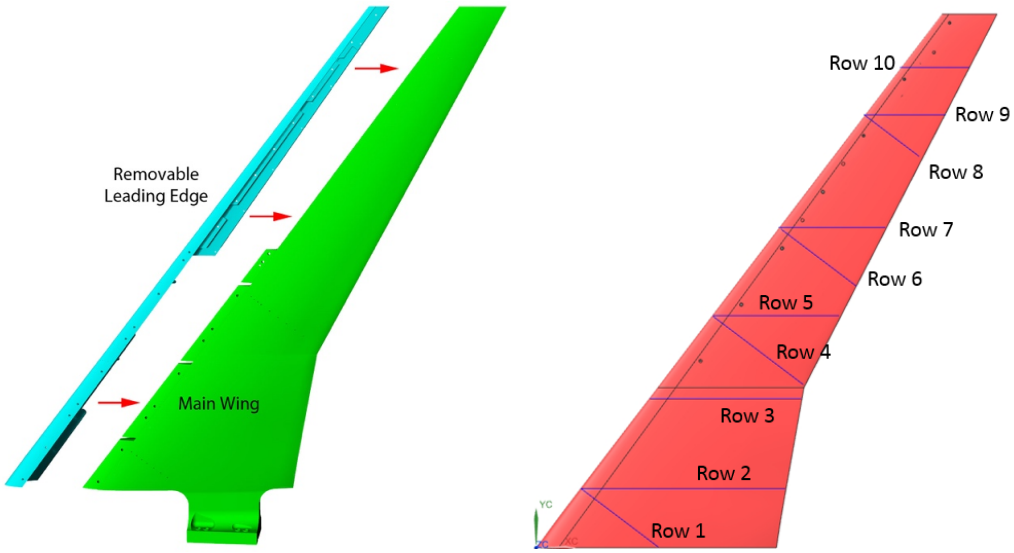

a) *b)*

Fig. 2.28 a) Removable leading edge feature b) Pressure tap locations of the wind tunnel model. Courtesy of Camello et al. [25]

2.4.3 Artificial ice shape manufacturing process

Once the full-span, leading-edge ice shapes were created they needed to be merged with the geometry of the removable leading edge of the swept-wing model using Geomagic Studio. To attach the full-span ice shape surface to the removable leading edge of the wing model, the full-scale, full-span ice shapes were scaled down to 8.9% of their original size so they could be merged with the removable leading edge of the scaled CRM65 wing for low Reynolds number wind tunnel testing. The CAD geometry of the removable leading edge was imported into Geomagic Studio. By using Geomagic Studio, as opposed to other 3D modeling programs, the removable leading edge geometry could be converted to a mesh and individual surfaces could be edited or removed. The removable leading edge converted to a mesh surface is shown in Fig. 2.29a) The leading-edge surface, where the mesh of the removable leading edge was combined with the mesh of the ice shape, was removed as shown in Fig. 2.29b). [25]

An area larger than the surface of the ice shape was removed to ensure a smooth blending between the two meshes. The ice shape mesh was placed in the location of the removed material and aligned to the ends of the removable leading edge mesh as shown in Fig. 2.29c). If the interpolation process was done correctly, the two meshes should match well without large steps between the edges. Finally, the two meshes were combined using the previously described bridge and hole-filling process. The combined ice shape and removable leading edge meshes are shown in Fig. 2.29d).

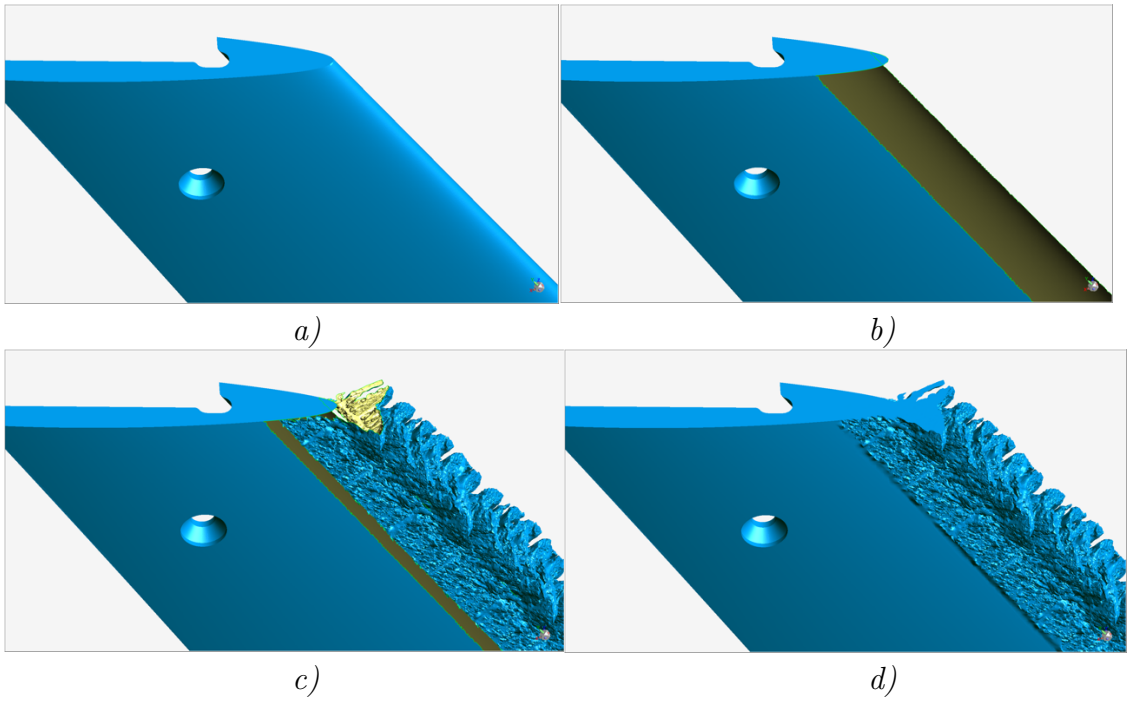

Fig. 2.29 Combining an ice shape mesh and a removable leading edge mesh. Courtesy of Camello et al. [25]

This process resulted in a solid iced leading edge that was 3D printed using stereolithography rapid prototype manufacturing with the Somos NeXt material. [29] This material was chosen based on its moisture resistance and thermal properties; these iced-leading edges would be stored for long periods of time and needed to be resistant to warping. Due to limitations of the machines used by the chosen manufacturer, the iced leading edges were rapid prototyped in two sections which were bolted onto the model during testing to minimize gaps and steps along the joint. All artificial ice shapes for these tests were produced using this method.

2.4.4 Experimental procedure

Force-balance, surface pressure, fluorescent mini-tuft, and surface oil-flow visualization data were collected during this test. The visualization methods were used to determine separated flow, vorticies, and other flow characteristics on the swept wing. Measurements were collected for Reynolds numbers of 0.8 x 10^6, 1.6 x 10^6, and 2.4 x 10^6,

Mach numbers of 0.09, 0.18, and 0.27, respectively, and the range of angle of attack of the model was changed from -6° to 16°. The procedure for collecting force balance data and surface pressure measurements was [27]:

- Set tunnel speed
- Measure tunnel conditions
- Record force balance data and surface pressure measurements
- Set new angle of attack and repeat steps

For the fluorescent mini-tuft visualization, 0.0019" diameter fluorescent monofilament pieces were attached to the model surface in a series of streamwise rows using cyanoacrylate adhesive. A UV black light filter was used to illuminate the tufts and the model was photographed at specific angles of attack while the tunnel was running.

For the surface-oil-flow visualization, black contact paper was applied to the model surface and a mixture of mineral oil and fluorescent dye was painted on with sponge paint rollers. The tunnel was run at a predetermined speed for two minutes from fan on to fan off, and a UV black light filter was used to illuminate the oil mixture and the model was photographed.

2.4.5 Wind tunnel wall corrections

A series of wind tunnel wall corrections were applied to all the aerodynamic data (C_L, C_D, C_M, C_P) using the method described by Pope et al. [30] and applied by Wichita State University [31]. By correcting for the effects of the wind tunnel walls, these data may be compared to future wind tunnel test results as well as CFD results. Ideally, wind tunnel models would be tested for freestream flight conditions; however, wind tunnel walls restrict the flow in the wind tunnel and alter the buoyancy, solid blockage, wake blockage, and streamline curvature [27].

The buoyancy of the wind tunnel model is affected by a streamwise gradient in the static pressure along the walls. It causes the flow to accelerate by effectively reducing the

cross-sectional area of the test section which increases the drag on the model [27]. The streamwise pressure gradient for this wind tunnel is known [31] and the effect on drag can be corrected [30].

The solid blockage of a wind tunnel depends on the geometries of the model and the test section [27]. When a model is placed in a test section, the cross-sectional area of the flow in the test section is reduced causing it to accelerate. The acceleration causes the wing model to experience a higher freestream dynamic pressure.

The wake blockage of a wind tunnel depends only on the size of the wake of the model. Slower flow in the wake of the model causes the surrounding flow to accelerate altering the freestream velocity [27].

The streamline curvature is created by the lift caused by the model. This curvature is altered by the constraints of the wind tunnel walls which in turn changes the flow around the model [27]. To compensate for the alteration of the streamline curvature, corrections are applied to the angle of attack (α), pitching moment, and induced drag [30].

Once these corrections are applied, the aerodynamic data from these wind tunnel tests conducted at the Walter H. Beech Wind Tunnel at Wichita State University may be compared to aerodynamic data from wind tunnel tests at other facilities. These correction methods are only approximations and ensuring the accuracy of these results requires the assessment of these results compared to various wind tunnels and CFD simulations [27].

Chapter 3 Results and Discussion

3.1 Summary of low-Reynolds number wind tunnel testing

Low-Reynolds number wind tunnel testing was conducted at the 7 ft x 10 ft Walter H. Beech Wind Tunnel at Wichita State University to study the aerodynamic performance of the swept-wing model with a variety of ice shape geometries and fidelities. Although the primary goals of this research are focused on the cruise condition for swept wings, features at higher angles of attack will still be explored in this thesis. The 8.9% scale model of the CRM65 was designed and fabricated with a removable leading edge to test the ice shape geometries accurately and efficiently. All the ice shape geometries were rapid prototyped using stereolithography and Somos NeXt material [29]. A total of 17 unique full-span ice shape configurations created from IRT experimental ice accretions using the interpolation and extrapolation methods described in Chapter 2 and Appendices A and B were rapid prototyped and tested. These are summarized in Table 3.1.

Table 3.1 Summary of ice shape configurations used for low Reynolds number wind tunnel testing

Ice Shape ID	Ice shape geometry	Fidelity
1.1.2	Maximum Scallop	High-fidelity
1.2.1		2D smooth
1.2.2		2D smooth with grit
3.1	Small Gap Scallop	High-fidelity
3.2.1		2D smooth
3.2.2		2D smooth with grit
2.1	Venetian Blind	High-fidelity
2.2.1		2D smooth
2.2.2		2D smooth with grit
5.1	Low AoA Scallop	High fidelity
5.2.1		2D smooth
5.2.2		2D smooth with grit
6.1.2	Streamwise	High-fidelity
6.2.1		2D smooth
6.2.2		2D smooth with grit
10.1	WB33	High-fidelity
4.1	Incomplete Scallop	High-fidelity

For all ice shape configurations, force balance, surface pressure, and mini-tuft flow visualization data were collected. Oil-flow visualization was conducted for a subset of the ice shapes. Only a subset was chosen due to time restrictions and similarities observed in the force balance data between ice-shape configurations.

3.1.1 Clean wing flowfield

Surface oil-flow visualization was conducted for the clean wing model for a Reynolds number of 1.6 x 10^6 and a Mach number of 0.18. Images were recorded over a range of angles of attack, however, the three presented in Fig. 3.1 at α = 9.0°, 11.1°, and 13.1° capture the aerodynamic features present as the model angle was increased through stall.

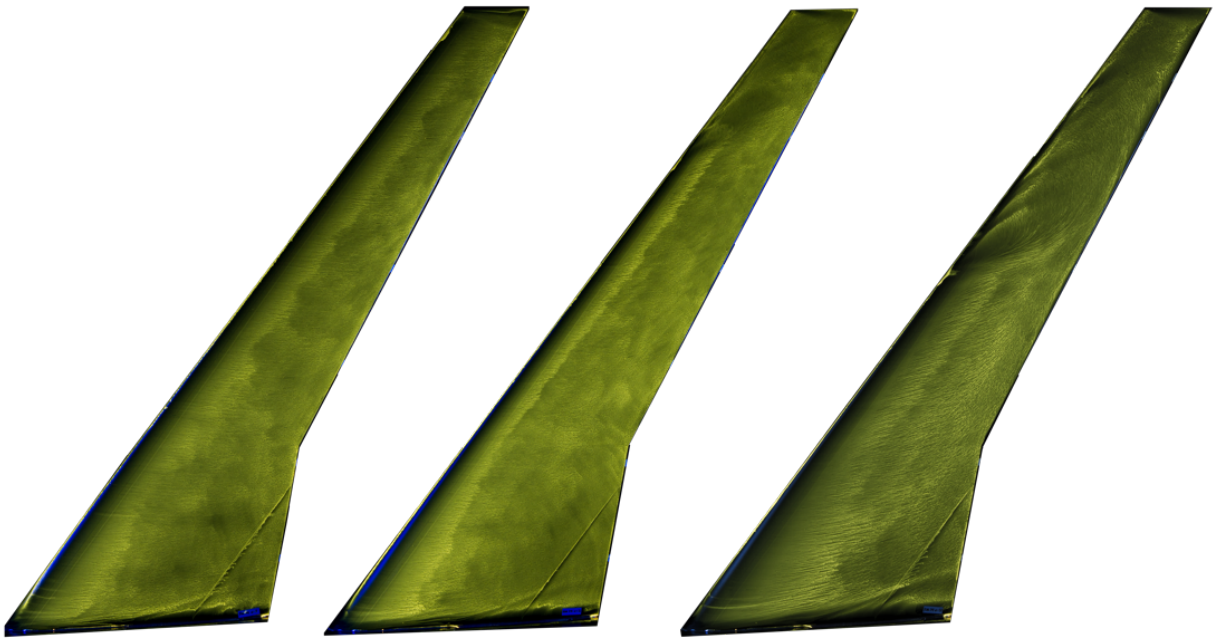

Fig. 3.1 Clean wing configuration oil-flow visualization at Re = 1.6 x 10^6 and M = 0.18 for α = 9.0°, 11.1°, and 13.1°, respectively.

In addition to oil-flow visualization, pressure contour plots were created from surface pressure data collected during the same runs as the aerodynamic performance data. A Matlab code to linearly interpolate and generate 75 virtual pressure tap rows from the existing rows was used to create the matrix for the contour plots. A griddata interpolator was applied to the matrix of experimental and virtual pressure taps to generate an initial color contour plot. Then a Matlab function, smooth2a [35], was used to smooth the interpolated data points. The distance from the root of the wing to the tip of the wing is defined as the butt-line (BL) in inches and the distance in the streamwise direction is defined as the fuselage station (FS) in inches. The pressure contour plots for the clean wing configuration at α = 9.0°, 11.1°, and 13.1° are shown in Fig. 3.2.

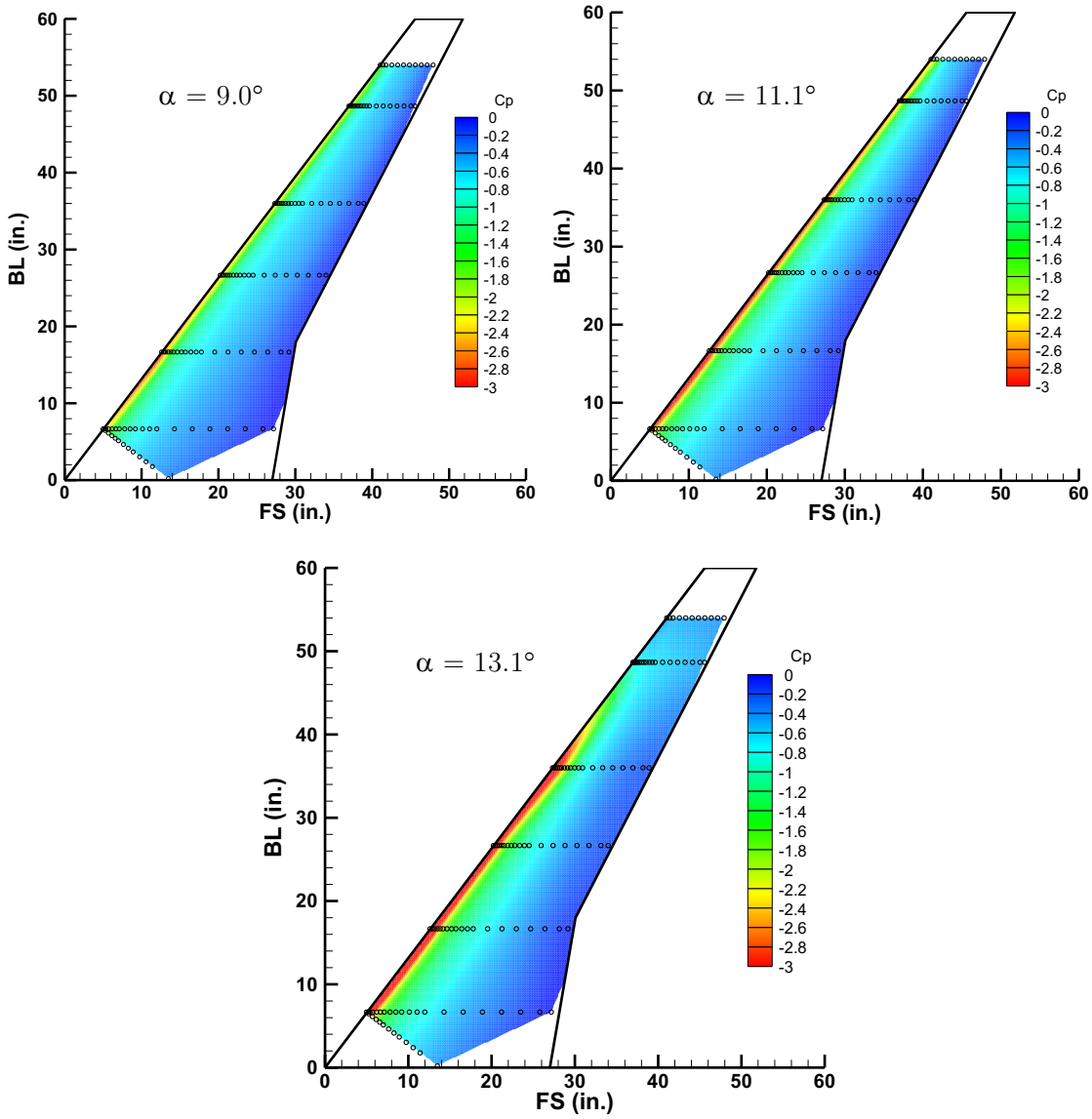

Fig. 3.2 Clean wing configuration pressure contour plots at Re = 1.6 x 10^6 and M = 0.18 for α = 9.0°, 11.1°, and 13.1°.

At α = 9.0°, the flow separated from the upper surface of the wing at the leading edge due to an adverse leading-edge pressure gradient. This initial flow separation is referred to as "Primary Separation" by Poll [32] which was characterized in Fig. 3.1 by an oil accumulation line at the leading edge of the swept-wing model. It was then inferred that the separated shear layer rolled up to form a vortex that reattached. The reattachment line of the leading-edge vortex was not visible in the oil-flow visualization as it may have been

in an area where the oil had been sheared away. The pressure contour plot in Fig. 3.2 clearly depicted the streamwise leading-edge vortex present at this angle of attack as a low pressure area at the leading edge over the span of the model.

At $\alpha = 11.1°$, the leading-edge vortex was shed into the wake near the tip of the wing causing a large area of separation. Initial flow separation at the tip is a commonly seen feature on swept wings due to a higher local lift coefficient and a lower local Reynolds number at the tip of the wing compared to the root of the wing. [33] At this higher angle of attack, the streamwise leading-edge vortex diameter increased to the point where it began to shed into the wake inboard of the tip. This was shown in the oil-flow visualization in Fig. 3.1 as a dark area bending away from the leading edge of the wing near the 80% span location. The turning of the leading-edge vortex into the wake of the wing was also previously observed in oil-flow visualization and wake survey data by Diebold [34] for a swept-wing model based on the CRM. When the model was increased past stall, about 30% of the wake of the model was dominated by the vortex shedding centered at the 70% span location [34]. The wake survey data by Diebold [34] is shown in Fig. 3.3.

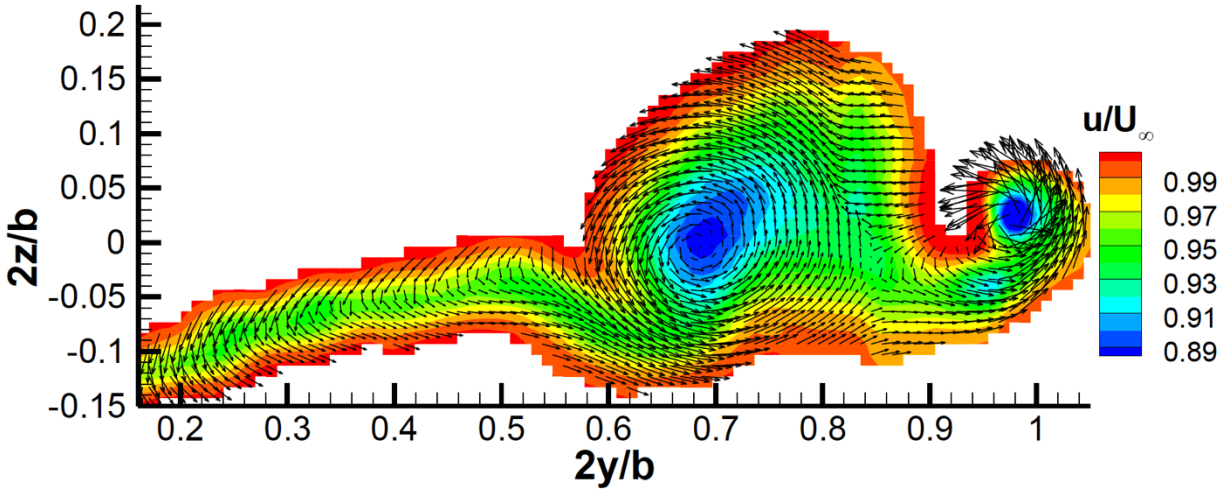

Fig. 3.3 Wake survey data for a swept-wing model based on the CRM at $\alpha = 10.7°$, $Re = 6 \times 10^5$ and $M = 0.15$. Courtesy of Diebold [34].

At $\alpha = 13.1°$, the streamwise leading-edge vortex began shedding into the wake near the midspan shown as the dark area at the 60% span location in Fig. 3.1. The suction significantly increased at the leading edge for the inboard 67% of the wing. This was shown as an increase in the area of red at the leading edge in Fig. 3.2. The outboard section, however, showed a decrease in leading-edge suction as the leading-edge vortex turned downstream and was shed into the wake and the wing tip experienced flow separation. This location of the change in leading-edge suction corresponded to the turning of the leading-edge vortex in the oil-flow visualization in Fig. 3.1.

For all three angles of attack, a thicker, brighter area of oil was present after the initial leading-edge separation. This is seen in the oil-flow visualization in Fig 3.1 at $\alpha = 9.0°$ where the thicker area of oil extended to about 30% of the chord near the wing root and about 50% of the chord near the wing tip. This may have been due to a drop-off in the shear stress at this location and does not necessarily indicate transition. Because a leading-edge vortex was present, the reattached flow was assumed turbulent.

3.1.2 Clean wing force balance data

The force balance performance data for the clean wing configuration at a Reynolds number of 1.6 x 10^6 and a Mach number of 0.18 is shown in Fig. 3.4. All force balance data have been corrected for wind tunnel effects including buoyancy, solid blockage, wake blockage, and streamline curvature using the methods previously described in Chapter 2. The lift and moment data reflect what was seen in the oil-flow visualization in Fig. 3.1 and our understanding of the flowfield. The nonlinear lift curve in Fig. 3.4 was due to flow separation at relatively low angles of attack and indicated a portion of the wing experienced flow separation as the angle of attack was increased. Determining stall for the entire swept wing can be a difficult and ambiguous process. While large portions of the flow on the wing

may be separated, a decrease in the integrated lift was not be observed in some cases in the angle of attack range tested.

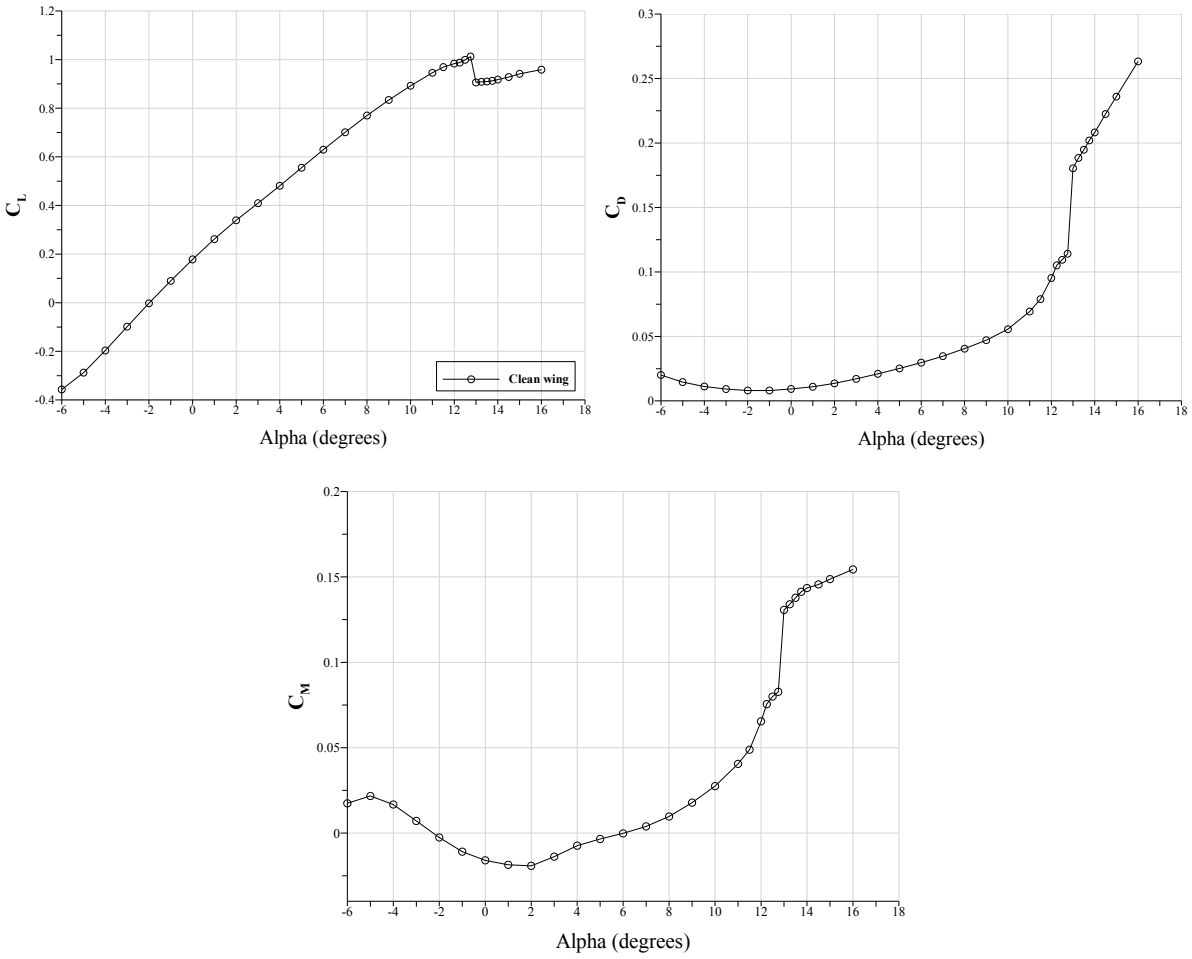

Fig. 3.4 Aerodynamic performance data for the clean wing configuration at Re = 1.6 x 10⁶ and M = 0.18.

From the oil-flow visualization and pressure contour plots at $\alpha = 9.0°$, the spanwise leading-edge vortex did not shed into the wake of the wing before reaching the wing tip. This was reflected in the lift data which continued increasing at a similar rate as the lower angles of attack as the model angle of attack was increased. There were no large changes in drag or moment present at $\alpha = 9.0°$ which confirmed that there was little or no separation present at the tip of the wing. Flow separation was present near the tip of the wing at $\alpha = 11.1°$ as the leading-edge vortex was swept into the wake. This caused an increase in pitching

moment and drag on the wing and a decrease in the lift curve slope. At $\alpha = 13.1°$, a greater area on the wing was separated as the streamwise leading-edge vortex was shed into the wake earlier along the span at the higher angle of attack. This was confirmed by the force balance data which showed a sharp increase in pitching moment and drag and a sharp decrease in the lift.

3.2 Iced wing configuration

3.2.1 Reynolds and Mach number effects

Force balance and pressure data were collected for Reynolds numbers of 0.8 x 10^6, 1.6 x 10^6, and 2.4 x 10^6 which correspond to freestream Mach numbers of 0.09, 0.18, and 0.27 are shown in Fig. 3.5. The differences in lift and drag of the model caused by the change in Reynolds number and Mach number for the same leading-edge configuration were small. This lack of Reynolds number and Mach number effect was also observed for ice shapes on airfoils by Broeren et al. [36], Bragg et al. [37], and Papadakis et al. [38]. Specifically, the Maximum Scallop configuration showed minimal change in lift and drag coefficients as the Reynolds number and Mach number were increased. The moment coefficients showed some slight differences mainly at the highest angles of attack tested, but they were after large increases in moment that indicated a portion of the wing was separated. Due to these results, the remainder of the data presented will be at a Reynolds number of 1.6 x 10^6.

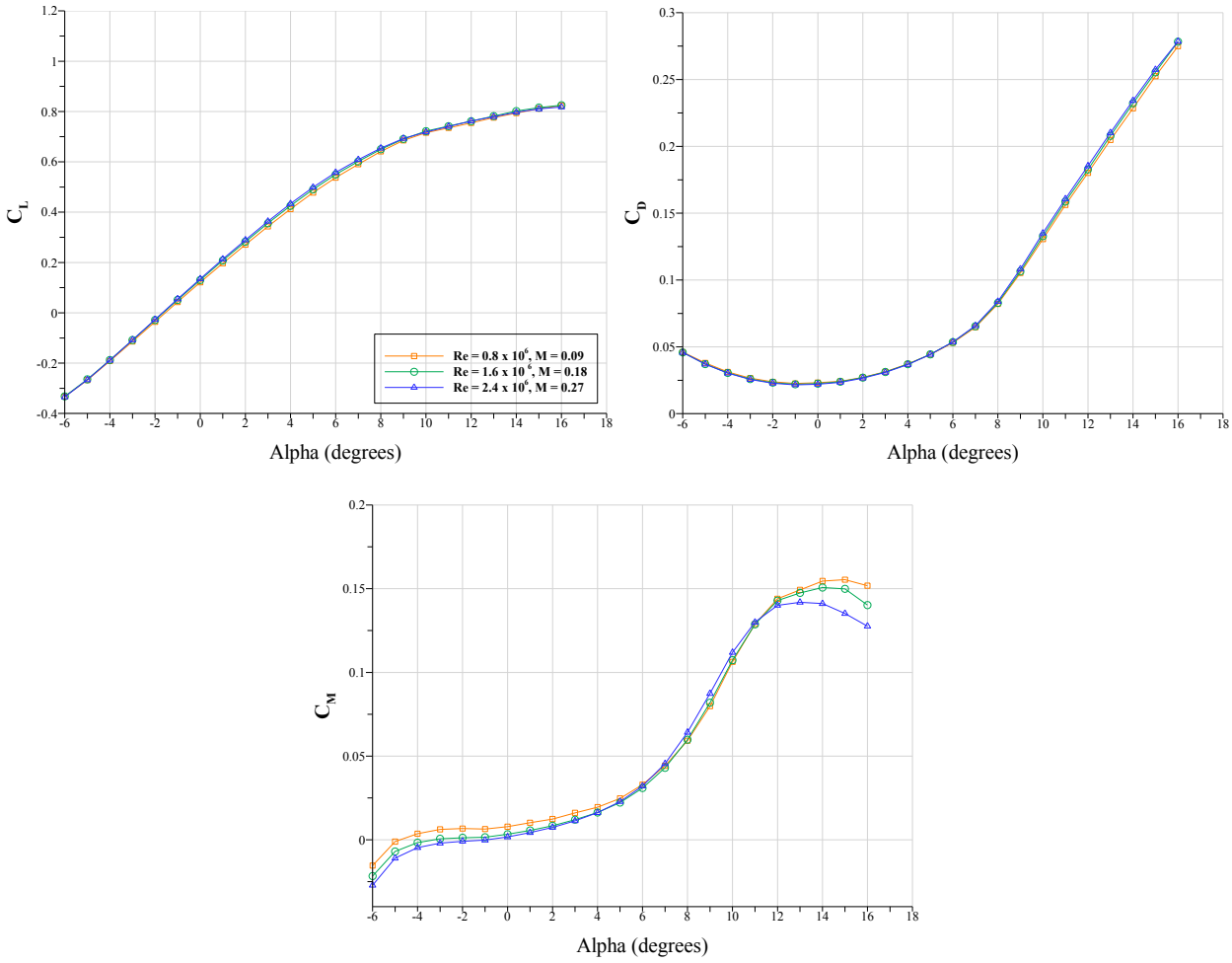

Fig. 3.5 Summary of aerodynamic performance data for the Maximum Scallop configuration with varying Reynolds and Mach numbers.

3.2.3 Ice shape selection for comparisons

Two of the goals of the low-Reynolds number wind tunnel tests were to determine how various high-fidelity ice shape geometries affect the aerodynamic performance of the swept-wing model and to investigate the fidelity needed to capture these effects in the wind tunnel tests. To study how various high-fidelity ice shape geometries affect the aerodynamic performance of the swept-wing model, 7 high-fidelity ice shape configurations were chosen to represent a large range of ice shape geometries. By selecting ice shape geometries that varied in horn height and void density, it was possible to study how much these features might have affected the aerodynamic performance of the wind tunnel model. Fig. 3.6

summarizes the lift, drag, and moment data for each of the high-fidelity ice shape configurations.

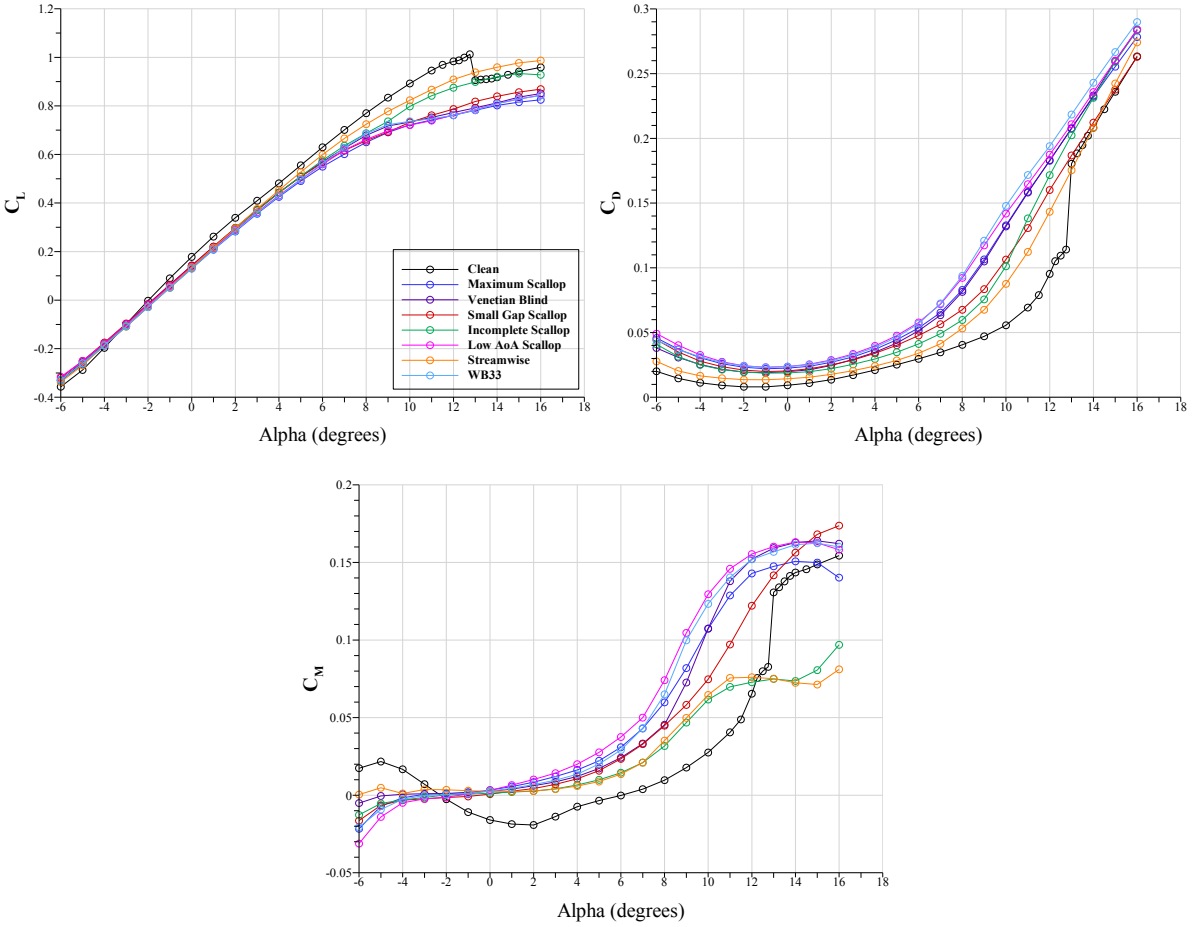

Fig. 3.6 Comparison of aerodynamic performance data for high-fidelity configurations at Re = 1.6 x 10⁶ and M = 0.18.

Because the results for many of the horn ice shapes containing scallop geometries, including the Maximum Scallop, Venetian Blind, Small Gap Scallop, Incomplete Scallop, and Low AoA Scallop, produced similar aerodynamic performance data as shown in Appendix C, a subset of the clean leading edge, the Streamwise, and the Maximum Scallop high-fidelity ice shapes will be compared in this chapter. The ice accretions for the midspan

of these configurations and a comparison of their maximum combined cross sections (MCCS) is shown in Fig. 3.7.

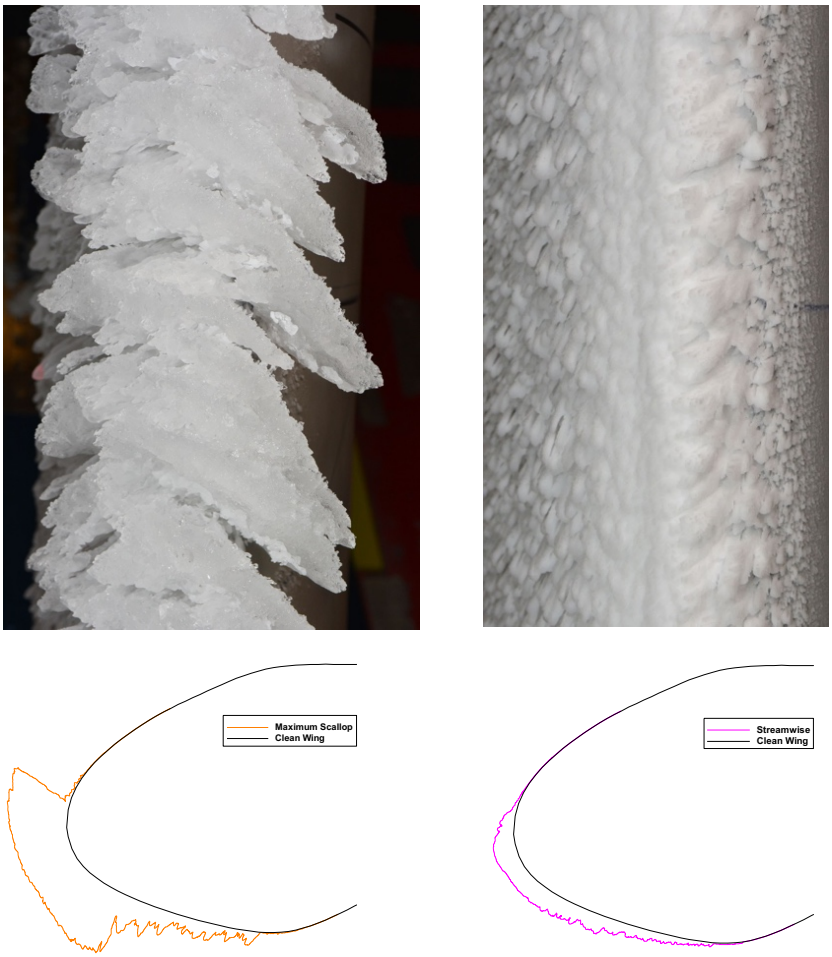

Fig. 3.7 Maximum Scallop and Streamwise experimental ice accretion including the maximum combined cross section (MCCS).

3.3 Streamwise configuration

3.3.1 High-fidelity Streamwise configuration

Surface oil-flow visualization was conducted for the Streamwise configuration for a Reynolds number of 1.6 x 10^6 and a Mach number of 0.18. Images were recorded over a range of angles of attack, however, the three presented in Fig. 3.8 at α = 6.9°, 9.0°, and 12.1° capture the aerodynamic features present as the model angle was increased.

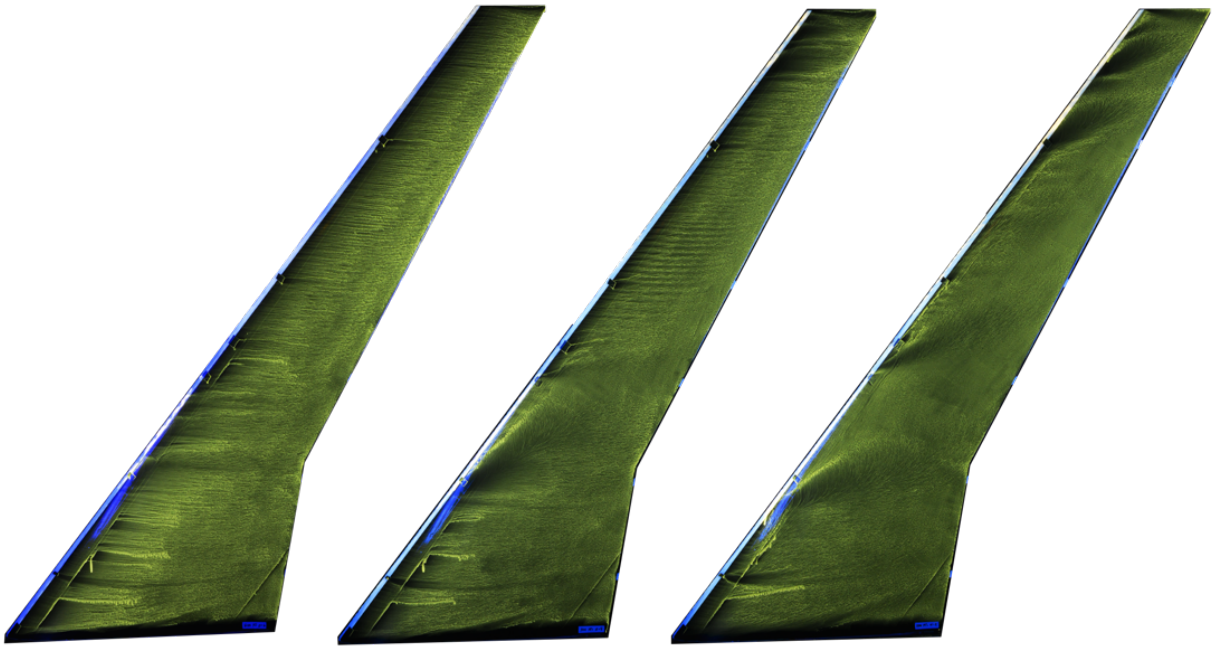

Fig. 3.8 Streamwise configuration oil-flow visualization at Re = 1.6 x 10^6 and M = 0.18 for α = 6.9°, 9.0°, and 12.1°, respectively.

Fluorescent mini-tuft visualization was conducted for the Streamwise configuration for a Reynolds number of 1.6 x 10^6 and Mach number of 0.18. This data provided an instantaneous snapshot of the flow at each angle of attack rather than a time average as in the oil-flow visualization. Images of the fluorescent mini-tuft visualization at the same angles of attack as the oil-flow visualization are shown in Fig. 3.9.

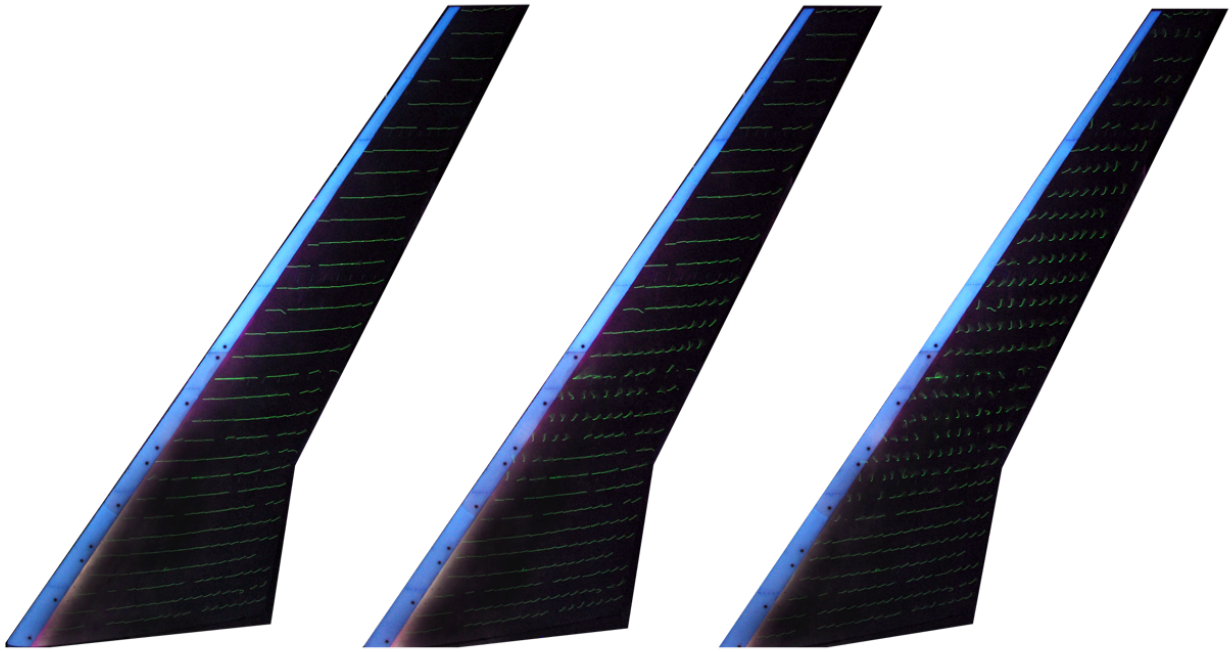

Fig. 3.9 *Streamwise configuration fluorescent mini-tuft visualization at Re = 1.6 x 10^6 and M = 0.18 for α = 6.9°, 9.0°, and 12.1°, respectively.*

In addition to oil-flow visualization and fluorescent mini-tuft visualization, pressure contour plots were created from surface pressure data collected during the same runs as the aerodynamic performance data. The pressure contour plots for the Streamwise configuration at α = 6.9°, 9.0°, and 12.1° are shown in Fig. 3.10.

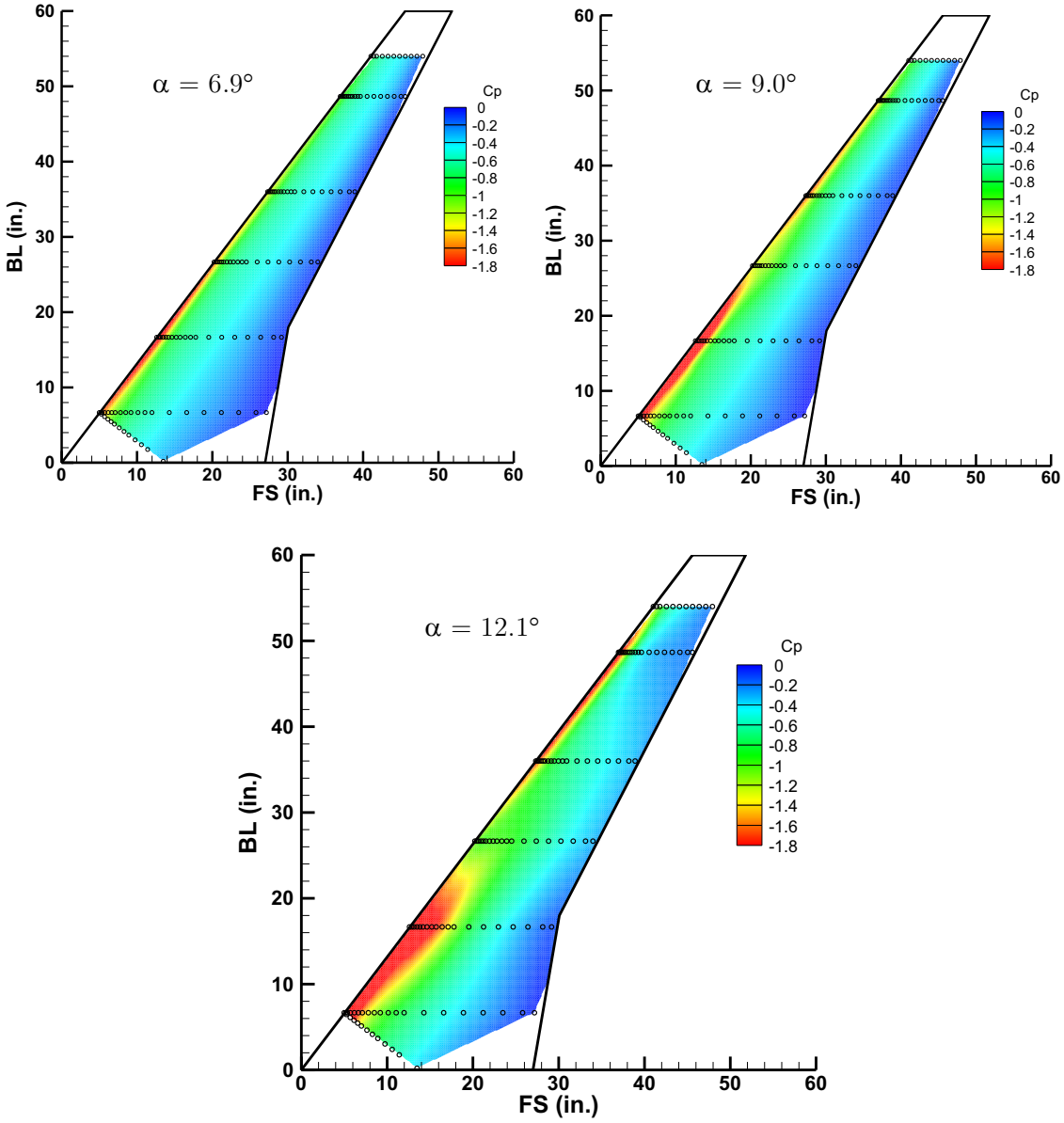

Fig. 3.10 Streamwise configuration pressure contour plots at Re = 1.6 x 10^6 and M = 0.18 for α = 6.9°, 9.0°, and 12.1°.

At α = 6.9°, the flow was characterized by a series of streamwise vorticies and the leading-edge vortex observed in the clean wing oil-flow visualization in Fig. 3.1 was not visible. Fig. 3.10 showed higher amounts of suction near the leading edge where the streamwise vorticies were present. The streamwise vorticies for the Streamwise configuration in Fig. 3.8 were evenly spaced along the leading edge near the outboard section of the wing,

but near the inboard larger gaps between some streamwise vorticies were present. These differences in spacing between the vorticies may have been a product of the Streamwise ice shape geometry or roughness. Minimal spanwise flow was observed near the trailing edge for this low angle of attack as almost all the tufts in Fig. 3.9 were oriented in the streamwise direction.

For high-fidelity ice shapes, the locations of streamwise vorticies and separation may be influenced by the ice shape geometry. The interpolation process described in Chapter 2 and Appendix B results in sections of repeated ice shape geometries. The effect of this periodicity in geometry was explored by Diebold [39]. Diebold [39] tested a scalloped ice shape geometry on a swept-wing model in the 3 ft x 4 ft wind tunnel at the University of Illinois Urbana-Champaign. The full-span ice shape was created by repeating the same scalloped ice shape geometry along the span of the leading edge rather than the interpolation process used in this research. Fig. 3.11 shows the leading-edge flowfield of the scalloped ice shape using oil-flow visualization at $\alpha = 3°$. The sections of repeated geometry are separated by the red lines and each section contained a pair of counter rotating vorticies.

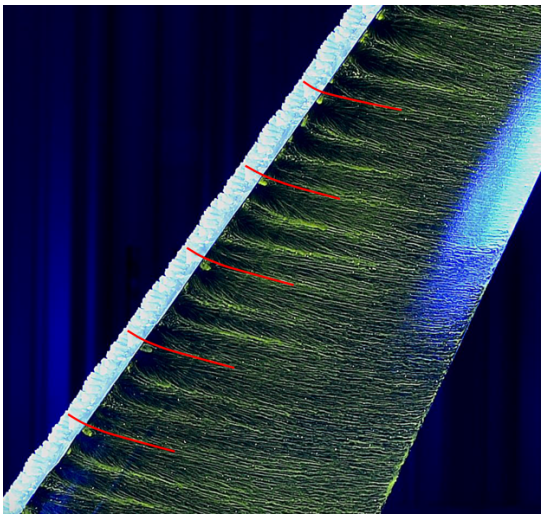

Fig. 3.11 Flowfield of repeated scallop ice shape geometry on subscale CRM65 geometry. Courtesy of Diebold. [39]

In Fig. 3.8 at $\alpha = 9.0°$, the streamwise vorticies near the inboard of the wing were replaced by areas of flow separation. This was observed as a dark area near the leading edge near the 25% span location in Fig. 3.8 and spanwise oriented tufts at this location in Fig. 3.9. This separation resulted from an area of high suction at the leading edge of the wing shown as an increase in the red area inboard of the 30% span location. Two smaller areas of separation developed near the 90% span location in Fig. 3.8, but were not observed in Fig. 3.9. Between the inboard and outboard areas of separated flow, the streamwise vorticies near the midspan section of the wing remained similar to the flow seen at the lower angle of attack in Fig. 3.8. This corresponded to the 40% span location where sudden increase in pressure was observed at the leading edge of the wing in Fig. 3.10. A small amount of spanwise flow was shown in the tufts in Fig. 3.9 at the trailing edge, inboard of the 50% span location.

At $\alpha = 12.1°$, almost all the streamwise vorticies were no longer visible in the oil-flow visualization, Fig. 3.8, and larger areas of separation appeared in four main areas along the leading edge of the wing. The areas of separation at approximately the 20% and 80% span locations corresponded to areas of high suction in Fig. 3.10. A significant amount of spanwise flow was present over the entire wing surface as shown in Fig. 3.9 as a majority of the tufts outboard of the 25% span location were oriented in the spanwise direction.

3.3.2 Low-fidelity Streamwise ice configurations

To achieve the objective of determining how ice shape fidelity affected the aerodynamic performance of the scaled CRM65 swept-wing model, low-fidelity versions of the Streamwise ice shape were compared to the high-fidelity version of the Streamwise ice shape. Low-fidelity ice shape geometries maintain the horn height and general shape of the high-fidelity ice shape geometries, but they do not model features such as scallops, voids, or roughness seen in the high-fidelity ice shape. The low-fidelity 2D smooth and 2D smooth

+ grit artificial ice shapes were created using the smoothed spline method previously described in Chapter 2. To determine how much ice shape roughness affected the aerodynamic performance of the model, silicon carbide grit was applied to the 2D smooth ice shape using double-sided tape. The Streamwise ice shape geometry was chosen for a fidelity comparison in this thesis based on the results presented in Appendix C. Many of the scalloped ice shapes produced similar force balance data to each other while the Streamwise ice shapes produced somewhat different characteristics.

3.3.2.1 Force balance data – Streamwise configurations

Force balance data were collected for the 2D smooth, 2D smooth + grit, and high-fidelity Streamwise configurations at a Reynolds number of 1.6 x 10^6 and Mach number of 0.18. These data were compared to the clean wing configuration and are summarized in Fig. 3.12.

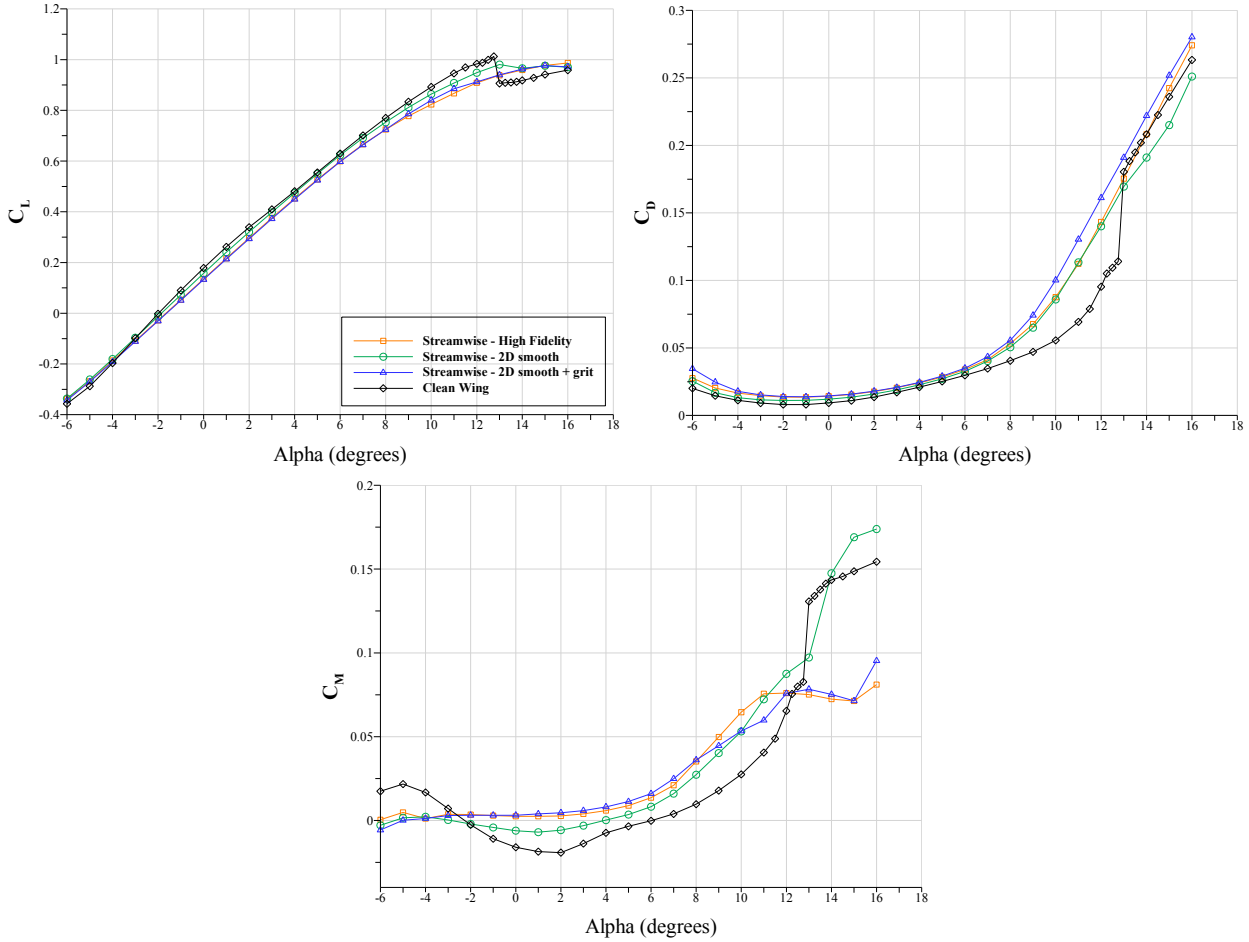

Fig. 3.12 Force balance data for the clean wing, 2D smooth, 2D smooth +grit, and high-fidelity Streamwise configurations for Re = 1.6 x 10^6 and M = 0.18.

While none of the iced-leading edge configurations had an abrupt stall point like the clean wing geometry, the 2D smooth Streamwise configuration showed a loss of lift at an angle of attack of approximately 13° and the 2D smooth + grit Streamwise configuration showed a loss of lift at angle of attack of approximately 15°. These losses in lift were confirmed by an increase in moment at 13° and 15° observed for the 2D smooth and 2D smooth + grit configurations, respectively. The high-fidelity Streamwise configuration continued to increase in lift until the end of the range of angles of attack tested. The high-fidelity Streamwise configuration showed separated flow at 9.0° which corresponded to a decrease in the lift curve slope and an increase in the moment curve slope at this angle of

attack. Overall, the 2D smooth + grit configuration predicted the high-fidelity lift, drag, and moment extremely well at lower angles of attack until 8° where the 2D smooth + grit configuration began over predicting the lift and drag generated by the high-fidelity ice shape.

3.3.2.2 2D smooth Streamwise configuration

Surface oil-flow visualization was conducted for the 2D smooth Streamwise configuration for a Reynolds number of 1.6 x 10^6 and Mach number of 0.18. Images were recorded over a range of angles of attack, however, the three presented in Fig. 3.13 at α = 6.9°, 9.0°, and 12.1° capture the aerodynamic features present as the model angle was increased.

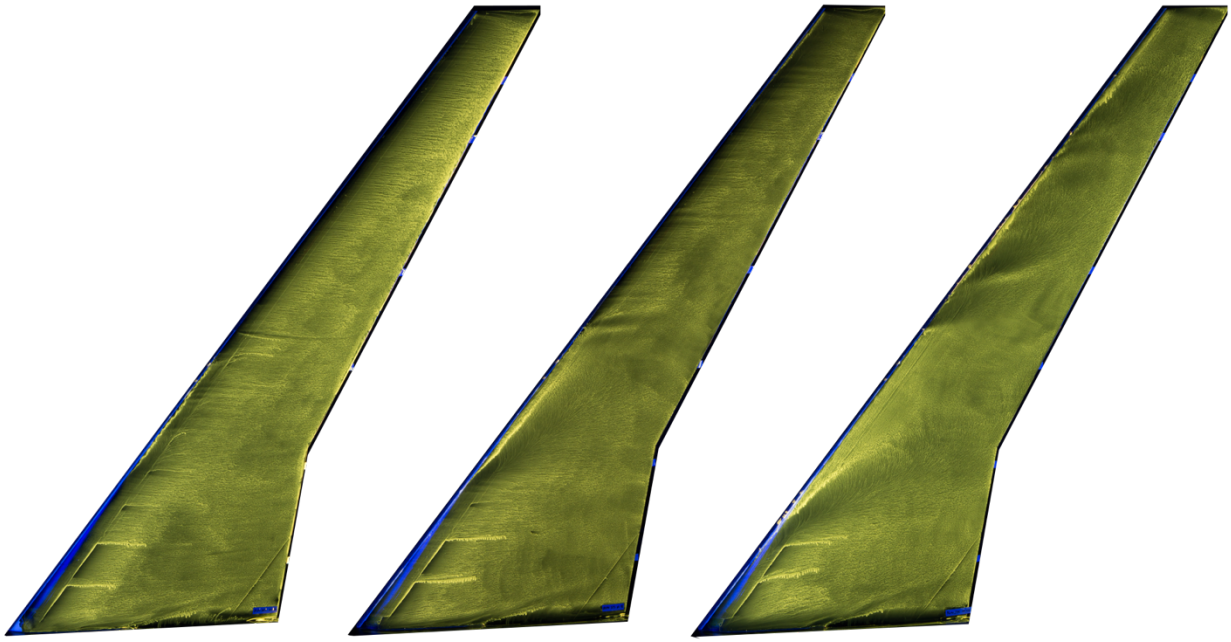

Fig. 3.13 2D smooth Streamwise configuration oil-flow visualization at Re = 1.6 x 10^6 and M = 0.18 for α = 6.9°, 9.0°, and 12.1°, respectively.

Fluorescent mini-tuft visualization was conducted for the 2D smooth Streamwise configuration for a Reynolds number of 1.6 x 10^6 and Mach number of 0.18. Images of the

fluorescent mini-tuft visualization at the same angles of attack as the oil-flow visualization are shown in Fig. 3.14.

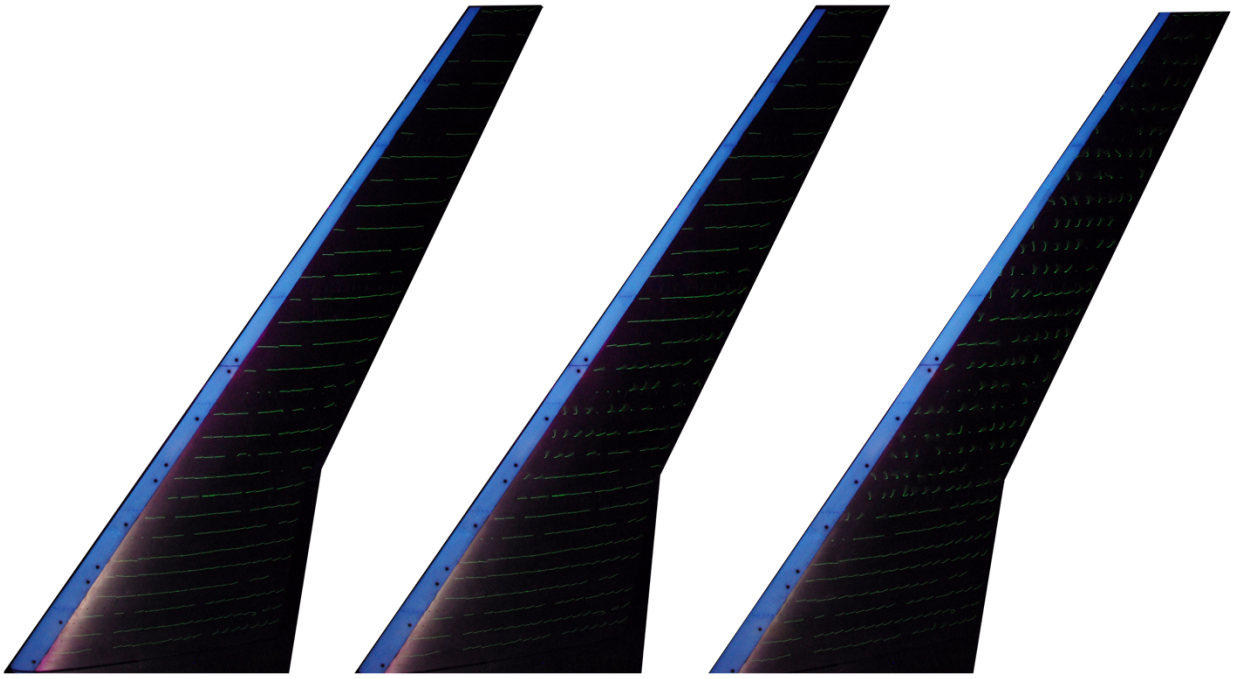

Fig. 3.14 2D smooth Streamwise configuration fluorescent mini-tuft visualization at Re = 1.6 x 10^6 and M = 0.18 for for α = 6.9°, 9.0°, and 12.1°, respectively.

In addition to oil-flow visualization and fluorescent mini-tuft visualization, pressure contour plots were created from surface pressure data collected during the same runs as the aerodynamic performance data. The pressure contour plots for the 2D smooth Streamwise configuration at the same angles of attack as the oil-flow and fluorescent mini-tuft visualization are shown in Fig. 3.15.

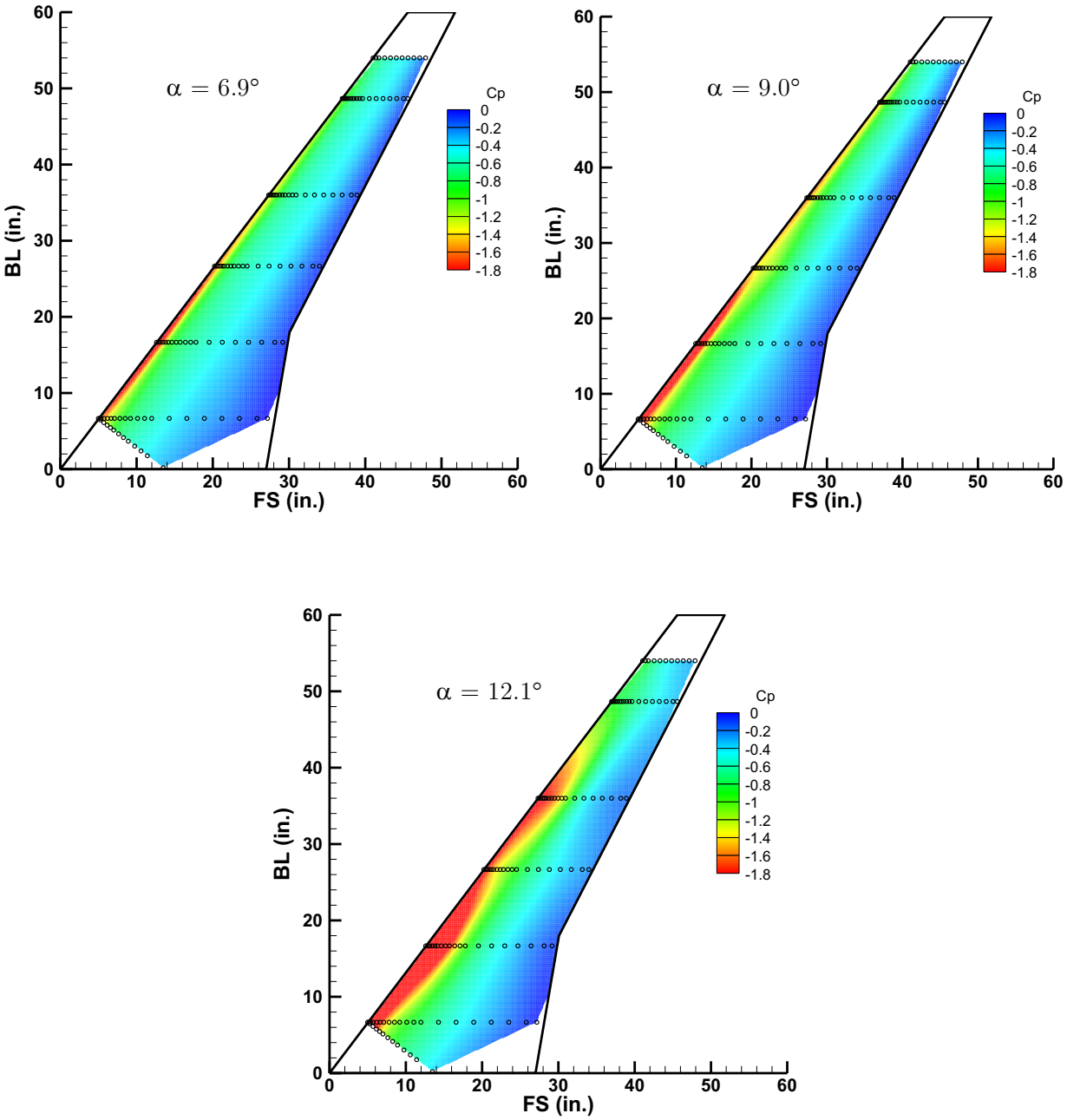

Fig. 3.15 2D smooth Streamwise configuration pressure contour plots at Re = 1.6 x 10^6 and M = 0.18 for α = 6.9°, 9.0°, and 12.1.

Although the oil-flow visualization did not show the streamwise vorticies for the 2D smooth Streamwise configuration that were observed in the high-fidelity Streamwise configuration in Fig. 3.8, the fluorescent mini-tuft data in Fig. 3.14 were extremely similar to the high-fidelity data in Fig. 3.9. At α = 9.0°, the leading-edge vortex was swept into

the wake at about the 30% span location for both ice shape configurations as shown in Figs. 3.9 and 3.14.

The pressure contour plots for the 2D smooth and high-fidelity Streamwise configurations agreed at the lower angles of attack, but showed some differences at α = 12.1°. Multiple areas of separation at the 20%, 50%, and 70% span locations for the 2D smooth Streamwise configuration were visible in Fig. 3.13 and 3.15 and almost all spanwise oriented tufts were observed outboard of the 25% span location in Fig. 3.14. While the 2D smooth Streamwise configuration maintained high amounts of suction near the inboard 30% of the leading edge, the area near the 50% span location showed much more suction for the 2D smooth Streamwise configuration in Fig. 3.15 than the high-fidelity Streamwise configuration in Fig. 3.10. This larger amount of suction near the leading edge of the wing may have led to the differences between the high-fidelity Streamwise configuration and 2D smooth Streamwise configuration in the force balance data.

3.3.2.3 2D smooth + grit Streamwise configuration

Oil-flow visualization data were not collected for the 2D smooth + grit Streamwise configuration. Fluorescent mini-tuft visualization was conducted for the 2D smooth Streamwise configuration for a Reynolds number of 1.6 x 10^6 and Mach number of 0.18. Images of the fluorescent mini-tuft visualization at α = 6.9°, 9.0°, and 12.1° are shown in Fig. 3.16.

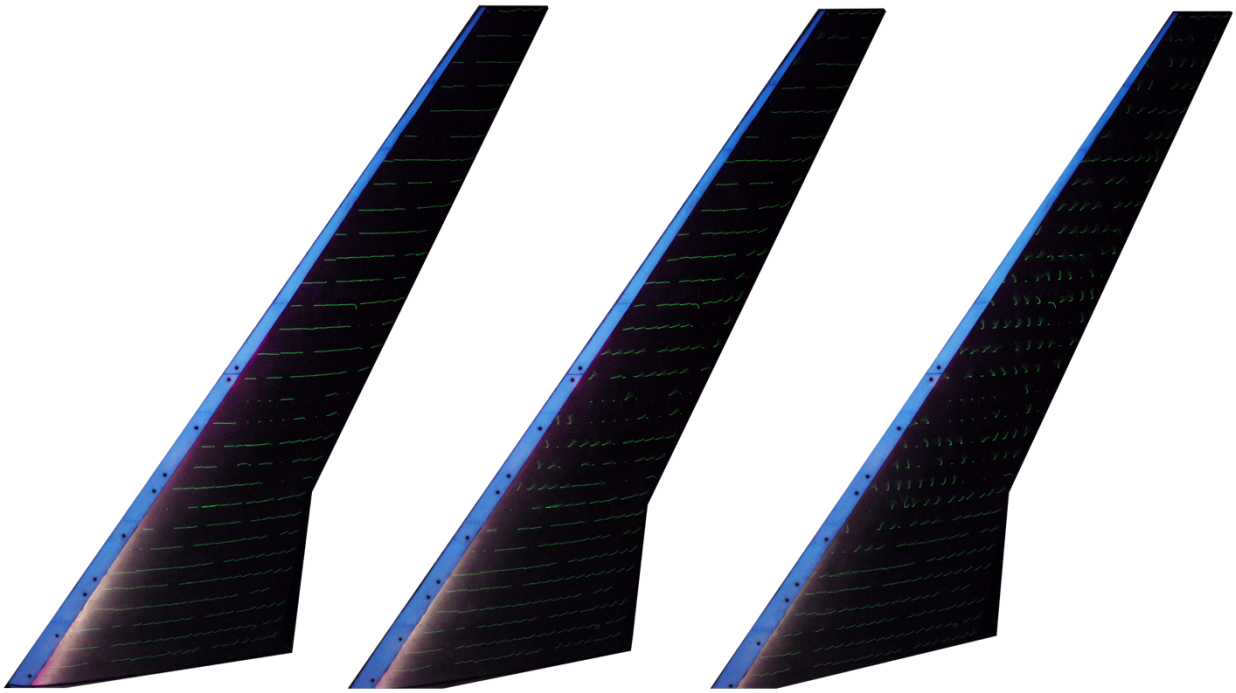

Fig. 3.16 2D smooth + grit Streamwise configuration fluorescent mini-tuft visualization at Re = 1.6 x 10^6 and M = 0.18 for for α = 6.9°, 9.0°, and 12.1°, respectively.

In addition to oil-flow visualization and fluorescent mini-tuft visualization, pressure contour plots were created from surface pressure data collected during the same runs as the aerodynamic performance data. The pressure contour plots for the 2D smooth + grit Streamwise configuration at the same angles of attack as the oil-flow and fluorescent mini-tuft visualization are shown in Fig. 3.17.

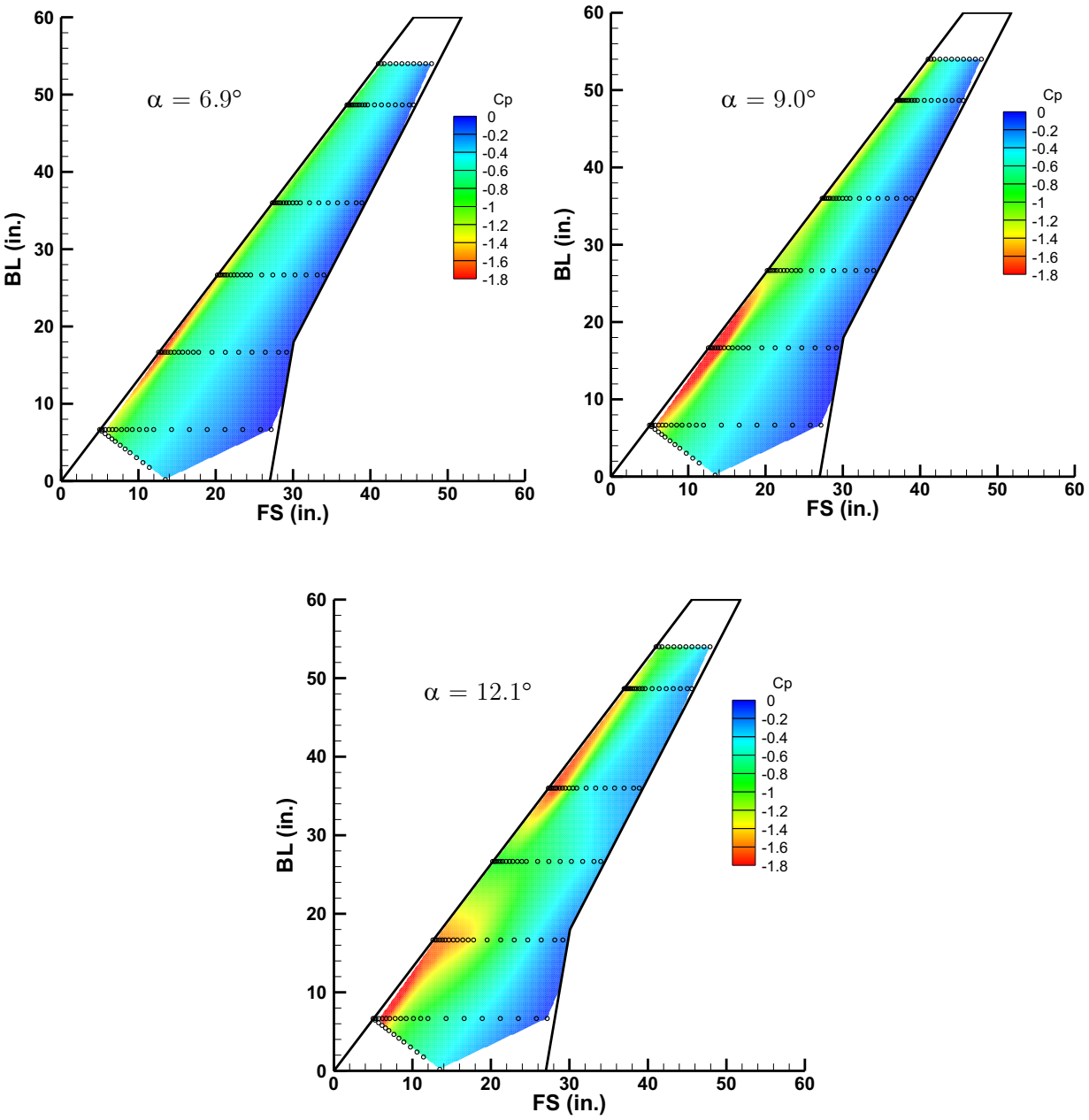

Fig. 3.17 2D smooth + grit Streamwise configuration pressure contour plots at Re = 1.6 x 10⁶ and M = 0.18 for α = 6.9°, 9.0°, and 12.1.

The mini-tuft visualization for the 2D smooth + grit Streamwise configuration was extremely similar to the mini-tuft visualization for the 2D smooth and high-fidelity Streamwise configurations. This showed that the fluorescent mini-tuft visualization was not detailed enough to discern differences in the flow between different ice shape fidelities. Because the force balance data previously presented proved that fidelity affected the

aerodynamics of the swept wing, it could not be assumed that similar mini-tuft visualization results proved a similar flowfield between the two configurations.

The pressure contour plots for the 2D smooth + grit Streamwise configuration showed patterns similar to the 2D smooth Streamwise and high-fidelity Streamwise configurations especially at the lower angles of attack. At $\alpha = 12.1°$ the plots for the 2D smooth + grit Streamwise configuration showed two distinct low pressure areas that were extremely similar to the high-fidelity Streamwise configuration pressure contour plots in Fig. 3.10. This similarity in pressure to the high-fidelity ice shape that was not seen in the 2D smooth Streamwise configuration may be why the force balance data for the 2D smooth + grit configuration better predicted the aerodynamic performance of the high-fidelity Streamwise ice shape.

3.4 Maximum Scallop configuration

3.4.1 High-fidelity Maximum Scallop configuration

Surface oil-flow visualization was conducted for the Maximum Scallop configuration for a Reynolds number of 1.6 x 10^6 and Mach number of 0.18. Images were recorded over a range of angles of attack, however, the three presented in Fig. 3.18 at $\alpha = 4.8°$, 7.9°, and 8.9° capture the aerodynamic features present as the model angle was increased.

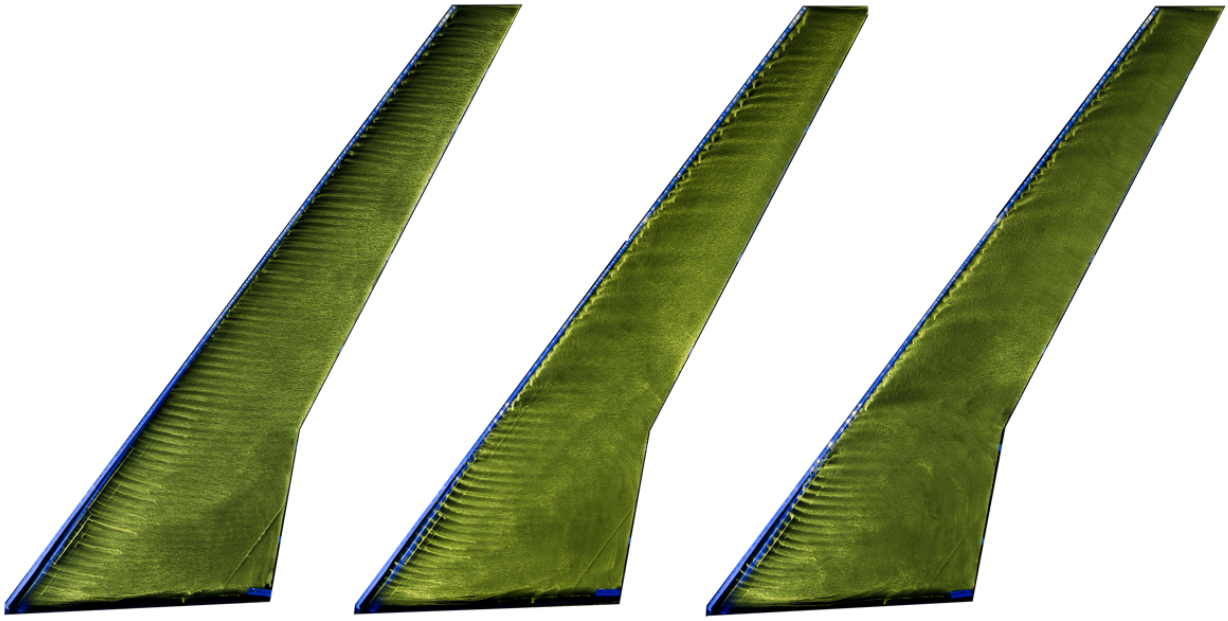

Fig. 3.18 Maximum Scallop configuration oil-flow visualization at Re = 1.6 x 10^6 and M = 0.18 for α = 4.8°, 7.9°, and 8.9°, respectively.

Fluorescent mini-tuft visualization was conducted for the Maximum Scallop configuration for a Reynolds number of 1.6 x 10^6 and Mach number of 0.18. Images of the fluorescent mini-tuft visualization at the same angles of attack as the oil-flow visualization are shown in Fig. 3.19.

Fig. 3.19 Maximum Scallop fluorescent mini-tuft visualization at Re = 1.6 x 10^6 and M = 0.18 for α = 4.8°, 7.9°, and 8.9°, respectively.

In addition to oil-flow visualization and fluorescent mini-tuft visualization, pressure contour plots were created from surface pressure data collected during the same runs as the aerodynamic performance data. The pressure contour plots for the Maximum Scallop configuration at α = 4.8°, 7.9°, and 8.9° are shown in Fig. 3.20.

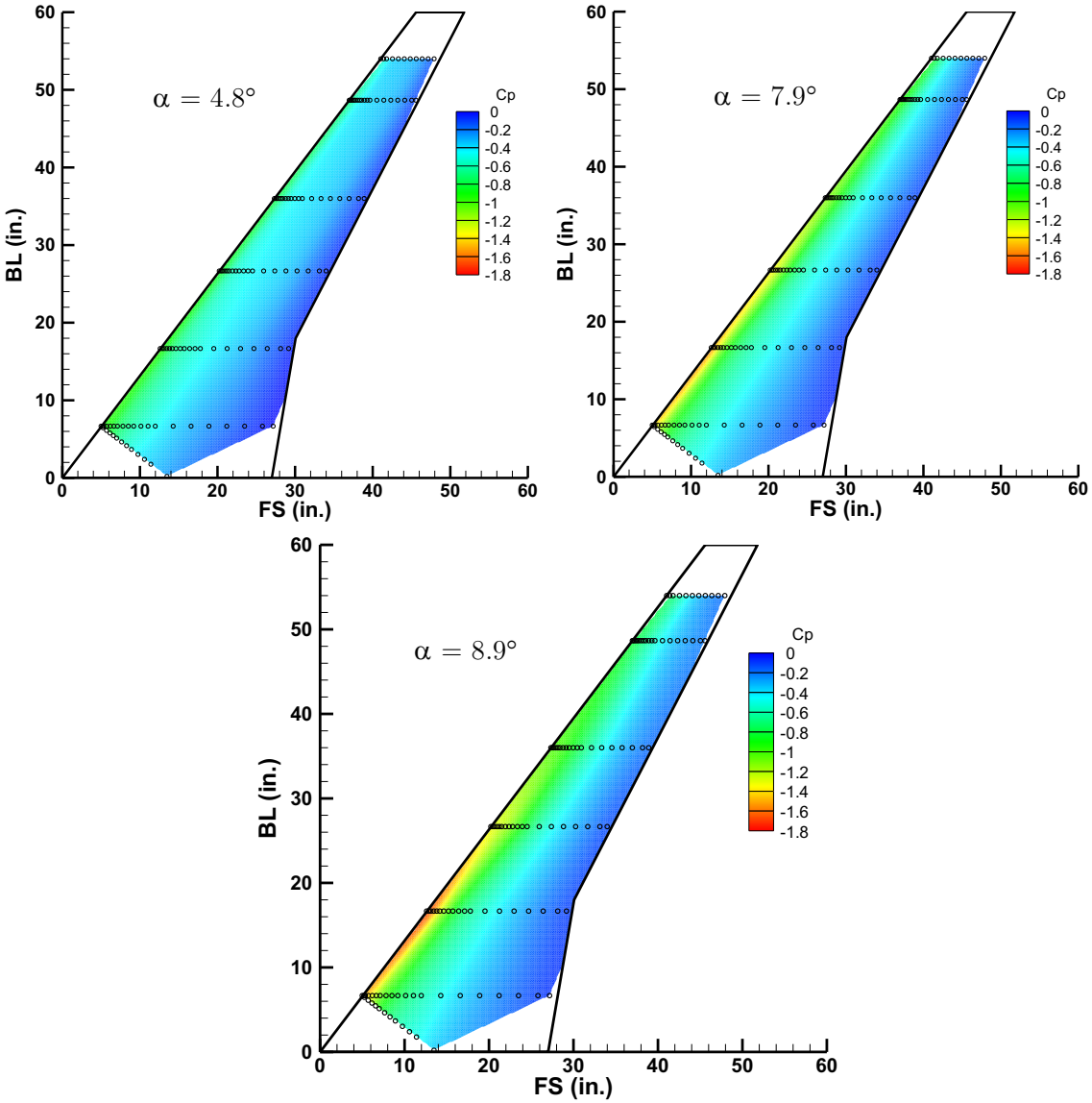

Fig. 3.20 Maximum Scallop configuration pressure contour plots at Re = 1.6 x 10^6 and M = 0.18 for α = 4.8°, 7.9°, and 8.9°.

At α = 4.8°, streamwise vorticies similar to those seen on the Streamwise configuration in Fig. 3.8 were present instead of the leading-edge vortex seen on the clean wing configuration in Fig. 3.1. While the leading-edge vortex may have been present for the Maximum Scallop configuration, it was not observed with the visualization methods used for these aerodynamic tests. The streamwise vorticies on the Maximum Scallop configuration in Fig. 3.18 were larger and more evenly spaced in the spanwise direction than

the Streamwise configuration and a low-pressure area was present in the same areas as the streamwise vorticies at the leading edge of the wing was observed in Fig. 3.20. The streamwise vorticies were most likely created by the gaps between the scallops on the Maximum Scallop geometry which acted like vortex generators. At this low angle of attack, little or no spanwise flow was observed at the trailing edge as almost all the mini-tufts were oriented in the streamwise direction in Fig. 3.19.

At $\alpha = 7.9°$, the streamwise vorticies were replaced by areas of spanwise flow near the midspan and outboard sections of the wing. Many of the tufts outboard of approximately the 50% span location were oriented in the spanwise direction in Fig. 3.19. At $\alpha = 8.9°$, almost all of the streamwise vorticies observed at the lower angles of attack in Fig. 3.11 had been replaced by spanwise flow and separation except for the inboard most section of the wing. This was confirmed in Fig. 3.19 as almost all the tufts were oriented in the spanwise direction everywhere on the wing except near the leading-edge of the inboard 25% of the wing.

3.4.2 Maximum Scallop fidelity comparison

To achieve the objective of determining how ice shape fidelity affected the aerodynamic performance of the scaled CRM65 swept-wing model, low-fidelity versions of the Maximum Scallop were compared to the high-fidelity version of the Maximum Scallop. Low-fidelity ice shape geometries maintain the horn height and general shape of the high-fidelity ice shape geometries, but they do not model features such as scallops, voids, or roughness seen in the full fidelity ice shape. The low-fidelity 2D smooth and 2D smooth + grit artificial ice shapes were created using the smoothed spline method previously described in Chapter 2. To determine how much ice shape roughness affected the aerodynamic performance of the model, silicon carbide grit was applied to the 2D smooth ice shape using double-sided tape. The Maximum Scallop geometry was chosen because it represents the

largest scallops and voids and therefore the largest geometric difference between the various fidelities. The high- and low-fidelity Maximum Scallop ice shapes installed on the swept-wing model in the wind tunnel are shown in Fig. 3.21.

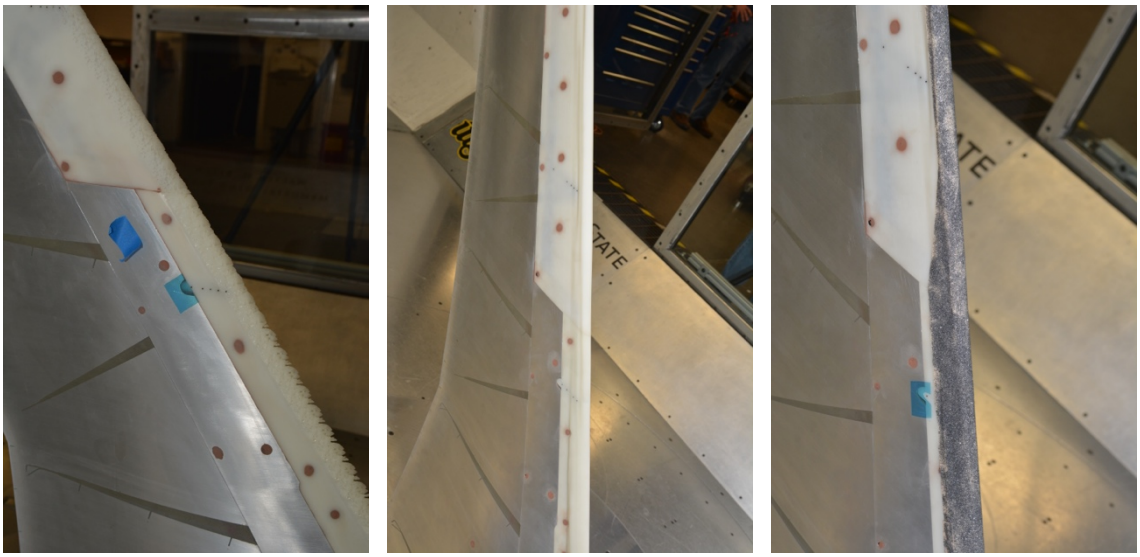

Fig. 3.21 Shown left to right; High fidelity, 2D smooth, and 2D smooth + grit Maximum Scallop artificial ice shapes installed on the 8.9% scale CRM65 wing.

3.4.2.1 Force balance data – Maximum Scallop fidelities

Force balance data were collected for the 2D smooth, 2D smooth + grit, and high-fidelity Maximum Scallop configurations at a Reynolds number of 1.6 x 10^6 and Mach number of 0.8. These data were compared to the clean wing configuration and is summarized in Fig. 3.22.

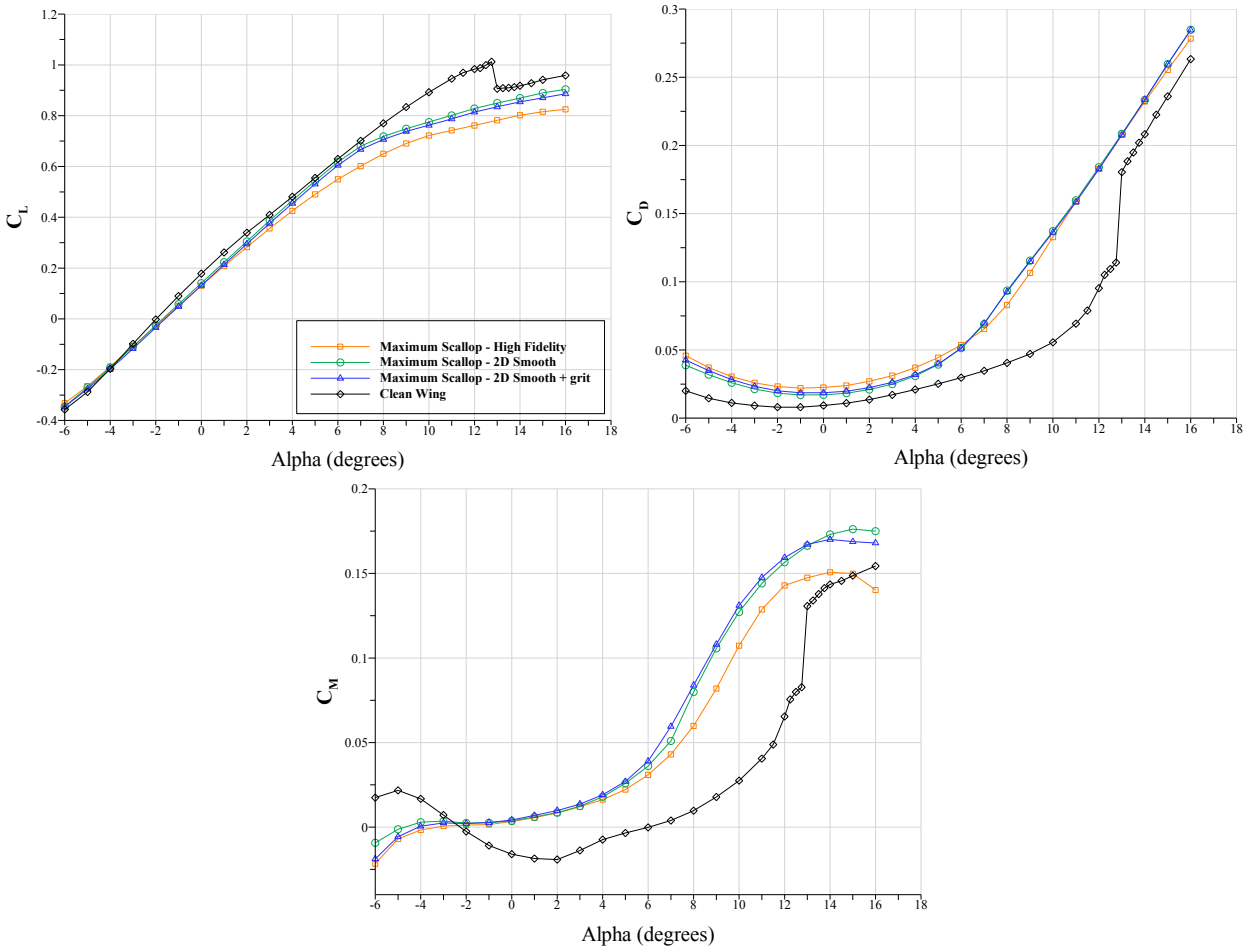

Fig. 3.22 Force balance data for the clean wing, 2D smooth, 2D smooth +grit, and high-fidelity Maximum Scallop configurations for Re = 1.6 x 10^6 and M = 0.18.

None of the Maximum Scallop configurations showed an abrupt stall point comparable to the clean model configuration, and for the iced configurations the lift increased with a gradual decrease in the slope until the highest angle of attack tested. While the general trends for the force balance data of all three fidelities of the Maximum Scallop geometry were similar, the low-fidelity versions were unable to produce the same aerodynamic performance. The performance of both the low-fidelity versions were extremely alike, especially for the drag performance at angles of attack greater than 6°. While the presence of the grit may have decreased the amount of lift generated, it did not greatly increase the amount of drag generated. At $\alpha = 7.9°$ the lift curve decreased in slope and

the drag and moment curves increased in slope for the low-fidelity Maximum Scallop configurations. These changes were similar to the decrease in lift curve slope and increase in drag and moment slopes for the high-fidelity Maximum Scallop configuration but they did not produce a conservative estimate for the lift generated. This angle of attack corresponded to the shedding of the leading-edge vortex into the wake near the midspan that was observed in the oil-flow visualization of the low-fidelity Maximum Scallop configurations in Figs. 3.23 and 3.27. At $\alpha = 8.9°$, flow separation and spanwise flow on the wing near the trailing edge of the wing may have led to the decrease in lift curve slope at this angle of attack. As the angle of attack was increased to $\alpha = 9.0°$ the slope of the lift curve continued decreasing and the slopes of the drag and moment continued increasing for the low-fidelity Maximum Scallop configurations. This was expected as the spanwise and separated flow over the wing continued to increase.

3.4.2.2 2D smooth Maximum Scallop configuration

Surface oil-flow visualization was conducted for the 2D smooth version of the Maximum Scallop geometry for a Reynolds number of 1.6 x 10^6 and a Mach number of 0.18. Images were recorded over a range of angles of attack, however, the three presented in Fig. 3.23 at $\alpha = 4.8°$, 7.9°, and 9.0° capture the aerodynamic features present as the model angle was increased.

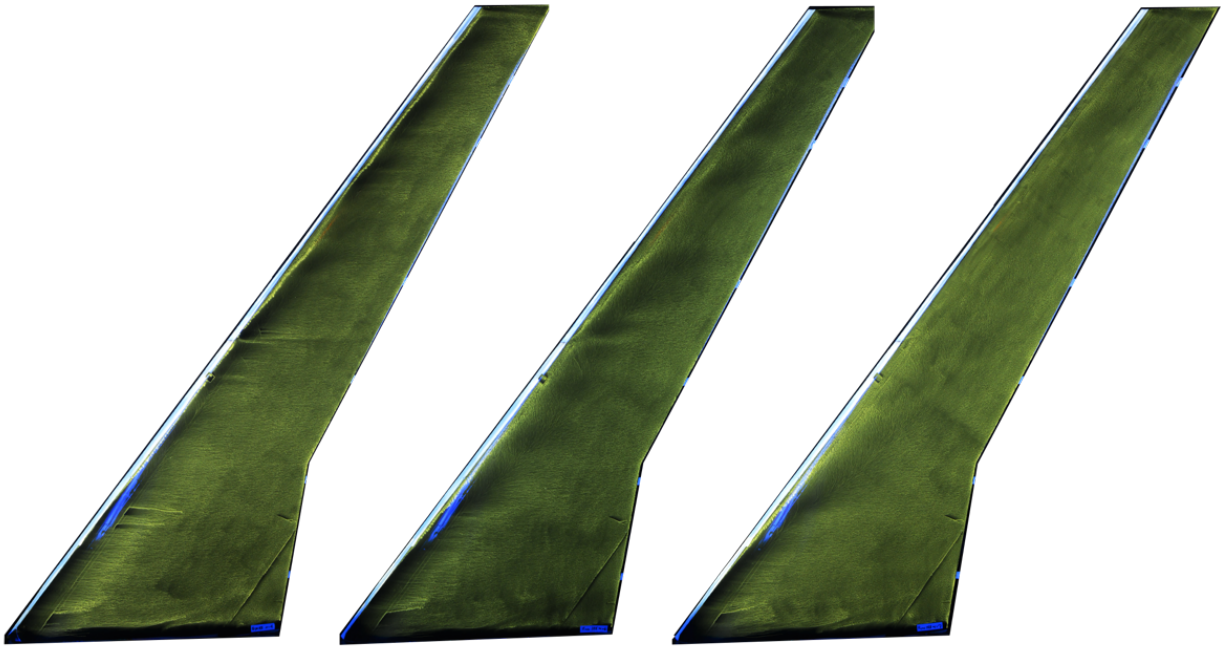

Fig. 3.23 2D smooth Maximum Scallop configuration oil-flow visualization at Re = 1.6 x 10^6 and M = 0.18 for α = 4.8°, 7.9°, and 9.0°, respectively.

Fluorescent mini-tuft visualization was conducted for the 2D smooth Maximum Scallop configuration for a Reynolds number of 1.6 x 10^6 and Mach number of 0.18. Images of the fluorescent mini-tuft visualization at the same angles of attack as the oil-flow visualization are shown in Fig. 3.24.

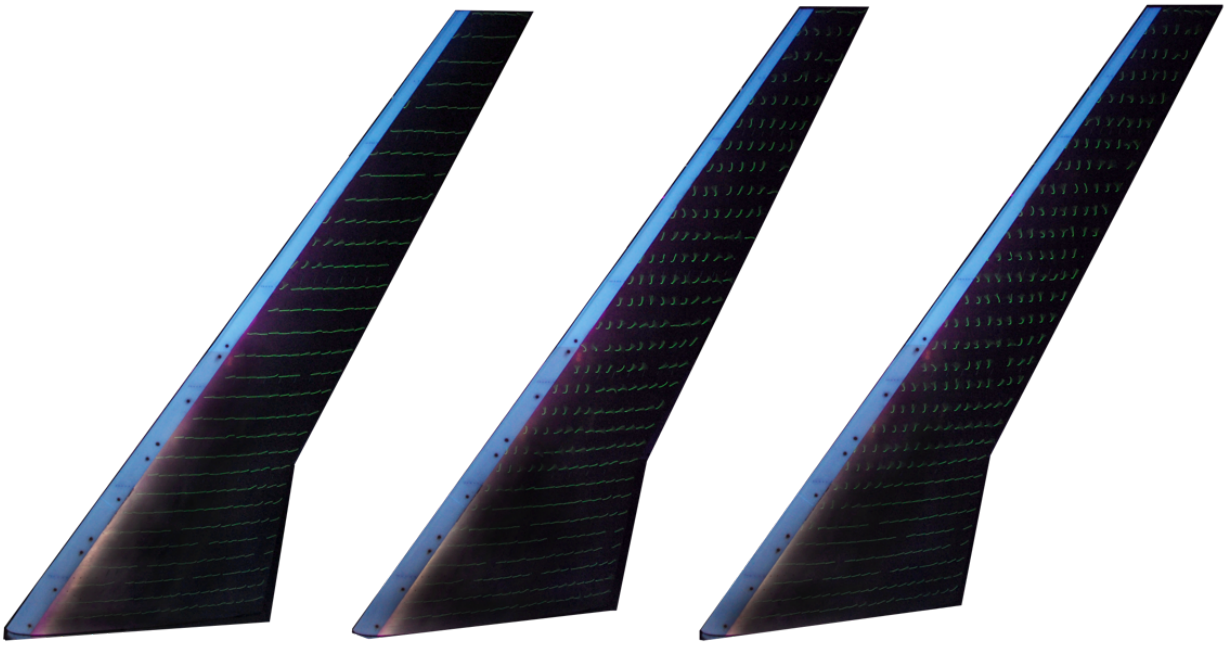

Fig. 3.24 2D smooth Maximum Scallop configuration fluorescent mini-tuft visualization at Re = 1.6 x 10^6 and M = 0.18 for α = 4.8°, 7.9°, and 9.0°, respectively.

In addition to oil-flow visualization and fluorescent mini-tuft visualization, pressure contour plots were created from surface pressure data collected during the same runs as the aerodynamic performance data. The pressure contour plots for the 2D smooth Maximum Scallop configuration at α = 4.8°, 7.9°, and 9.0° are shown in Fig. 3.25.

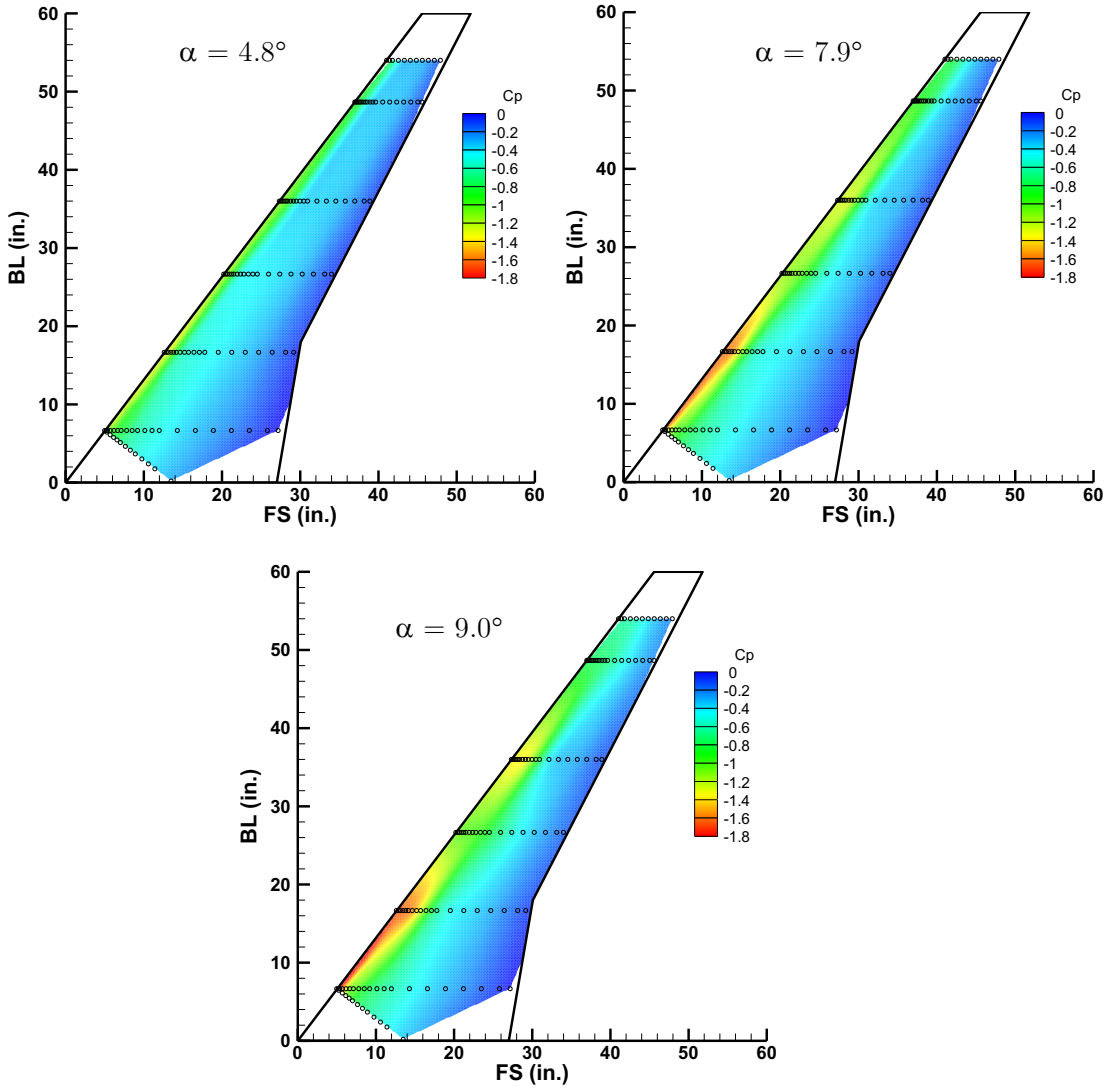

Fig. 3.25 2D smooth Maximum Scallop configuration pressure contour plots at Re = 1.6 x 10^6 and M = 0.18 for α = 4.8°, 7.9°, and 9.0°, respectively.

At α = 4.8°, separation at the leading edge of the wing rolled up to create a vortex that reattached downstream of the initial separation at about the 20% chord location. The leading-edge vortex was similar to the leading-edge vortex observed in the clean wing flow in Fig. 3.1, however, the radius of the leading-edge vortex for the 2D smooth Maximum Scallop configuration was large enough that the oil was not swept away by the shear forces near the reattachment line. A small area of tufts oriented in the spanwise direction was observed near the leading edge of the wing in Fig. 3.24 unlike the fluorescent mini-tuft

visualization for the high-fidelity Maximum Scallop configuration in Fig. 3.19. Because these spanwise oriented tufts were near the leading edge of the model they may have been a result of the larger radius of the leading-edge vortex for the 2D smooth Maximum Scallop flowfield seen in the oil-flow visualization in 3.23. The reattachment line was observed in Fig. 3.26 as the spanwise line near the leading edge of the model that divided flow moving upstream from flow moving downstream. The leading-edge vortex was depicted in the pressure contour plots in Fig. 3.25 as a green area of higher suction near the leading edge of the wing. When the leading-edge vortex reattached to the wing, the suction decreased in the flow near the trailing edge.

In addition to the reattachment line, some areas of "Secondary Separation" as defined by Poll [32] were observed as an accumulation of oil directly at the leading edge of the wing in Fig. 3.26. The boundary-layer flow upstream of the reattachment line and underneath the core of the vortex moved towards the leading edge of the wing and separated due to the favorable pressure gradient created by the spanwise leading-edge vortex. The features of the leading-edge vortex for the 2D smooth Maximum Scallop configuration at $\alpha = 4.8°$ are shown in Fig. 3.26.

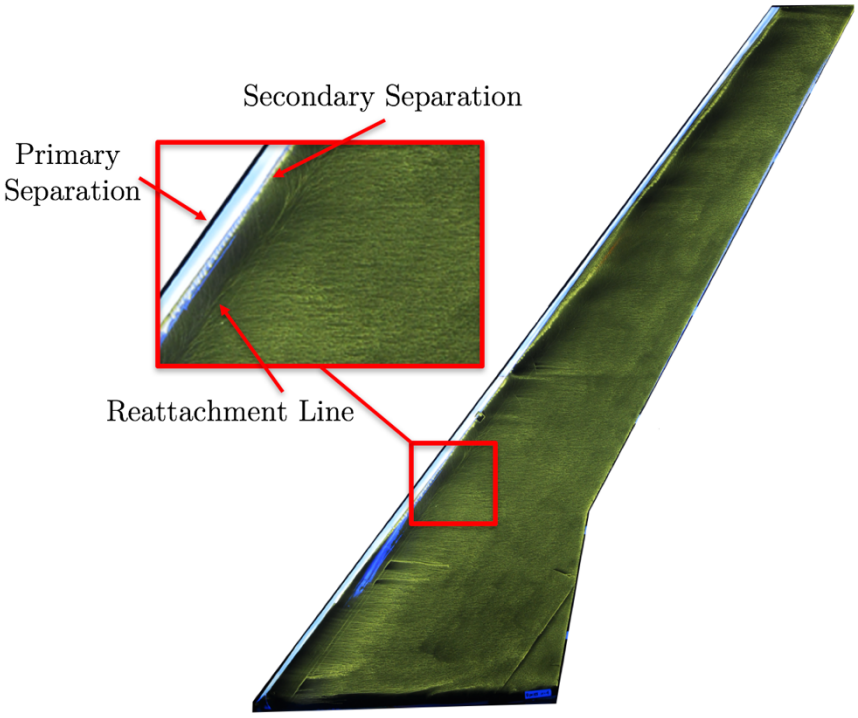

Fig. 3.26 Features of the leading-edge vortex on the 2D smooth Maximum Scallop configuration at Re = 1.6 x 10⁶ and M = 0.18 for α = 4.8°

A few streamwise vorticies were present along the leading edge of the wing in Fig. 3.23 especially near the tip, but the flow appeared to be dominated by the leading-edge vortex. Because the 2D smooth version of the Maximum Scallop configuration did not contain the voids between scallops, the streamwise vorticies did not appear at regular intervals along the span of the wing. Instead, the streamwise vorticies may have been created from other changes in geometry of the 2D smooth Maximum Scallop configuration.

At $\alpha = 7.9°$, the radius of the leading-edge vortex and the reattachment line moved downstream to about the 30% chord location as the angle of attack was increased. This was shown in the pressure contour plots in Fig. 3.25 as an increased area of green on the wing surface, and an increase in suction appeared near the wing inboard leading edge as an area of orange. This increased suction near the inboard was much more pronounced for the 2D smooth Maximum Scallop configuration than for the high-fidelity Maximum Scallop

configuration. The leading-edge vortex was swept into the wake near the 40% span location of the wing. This was shown in Fig. 3.24 by spanwise oriented tufts outboard of the 40% span location. Although the leading-edge vortex was swept into the wake near the midspan, the continued presence of high suction near the leading edge of the outboard section of the wing could potentially be attributed to the streamwise vorticies.

At $\alpha = 9.0°$, the leading-edge vortex was swept into the wake near the inboard of the wing at approximately the 20% span location and a majority of the wing surface showed spanwise or separated flow in Fig. 3.24. No streamwise vorticies were present in the oil-flow visualization in Fig. 3.23 at this high angle of attack however the suction near the inboard of the wing increased even more. Even though Fig. 3.24 depicted spanwise flow and separation along most of the wing area in the tufts, the pressure contour plots showed that some of the streamwise vorticies may have been present at the areas of high-suction shown in green in Fig 3.25 near the leading edge of the wing. If the leading-edge vortex had been swept into the wake and no streamwise vorticies were present, the leading edge may have returned to a lower suction state outboard of the turning point of the leading-edge vortex that was previously seen in Fig. 3.2 for the clean wing configuration.

3.4.2.3 2D smooth plus grit Maximum Scallop configuration

Surface oil-flow visualization was conducted for the 2D smooth + grit version of the Maximum Scallop geometry for a Reynolds number of 1.6 x 10^6 which corresponded to a Mach number of 0.18. Images were recorded over a range of angles of attack, however, the three presented in Fig. 3.27 at $\alpha = 4.8°$, 7.9°, and 9.0° capture the aerodynamic features present as the model angle was increased.

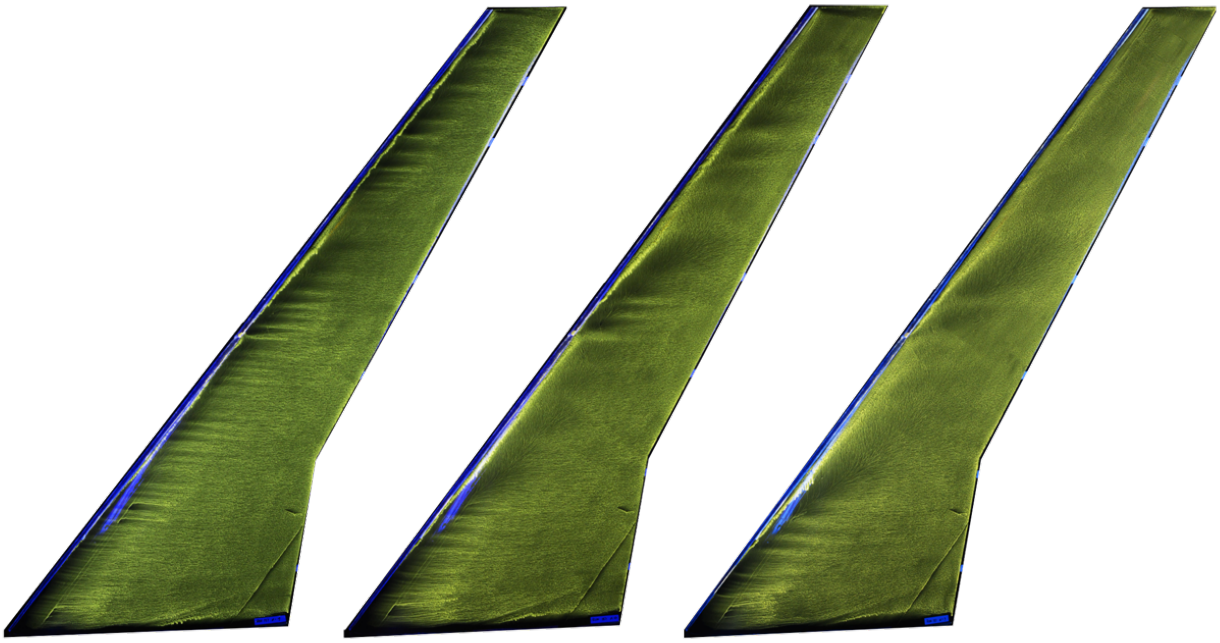

Fig. 3.27 2D smooth +grit Maximum Scallop configuration oil-flow visualization at Re = 1.6 x 10^6 and M = 0.18 for α = 4.8°, 7.9°, and 9.0°, respectively.

Fluorescent mini-tuft visualization was conducted for the 2D smooth + grit Maximum Scallop configuration for a Reynolds number of 1.6 x 10^6 and Mach number of 0.18. Images of the fluorescent mini-tuft visualization at the same angles of attack as the oil-flow visualization are shown in Fig. 3.28.

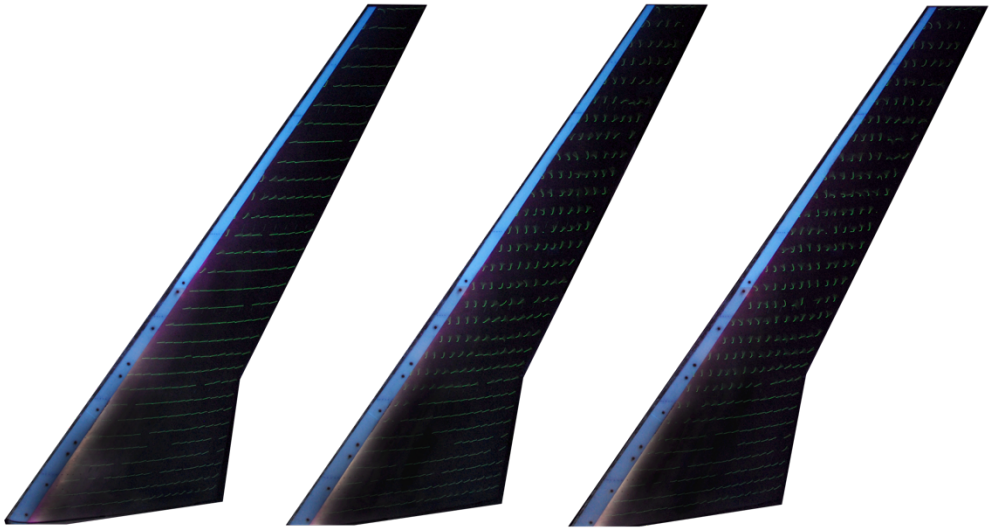

Fig. 3.28 2D smooth + grit Maximum Scallop configuration fluorescent mini-tuft visualization at Re = 1.6 x 10^6 and M = 0.18 for α = 4.8°, 7.9°, and 9.0°, respectively.

In addition to oil-flow visualization and fluorescent mini-tufts, pressure contour plots were created from surface pressure data collected during the same runs as the aerodynamic performance data. The pressure contour plots for the 2D smooth + grit Maximum Scallop configuration at $\alpha = 4.8°$, 7.9°, and 9.0° are shown in Fig. 3.29.

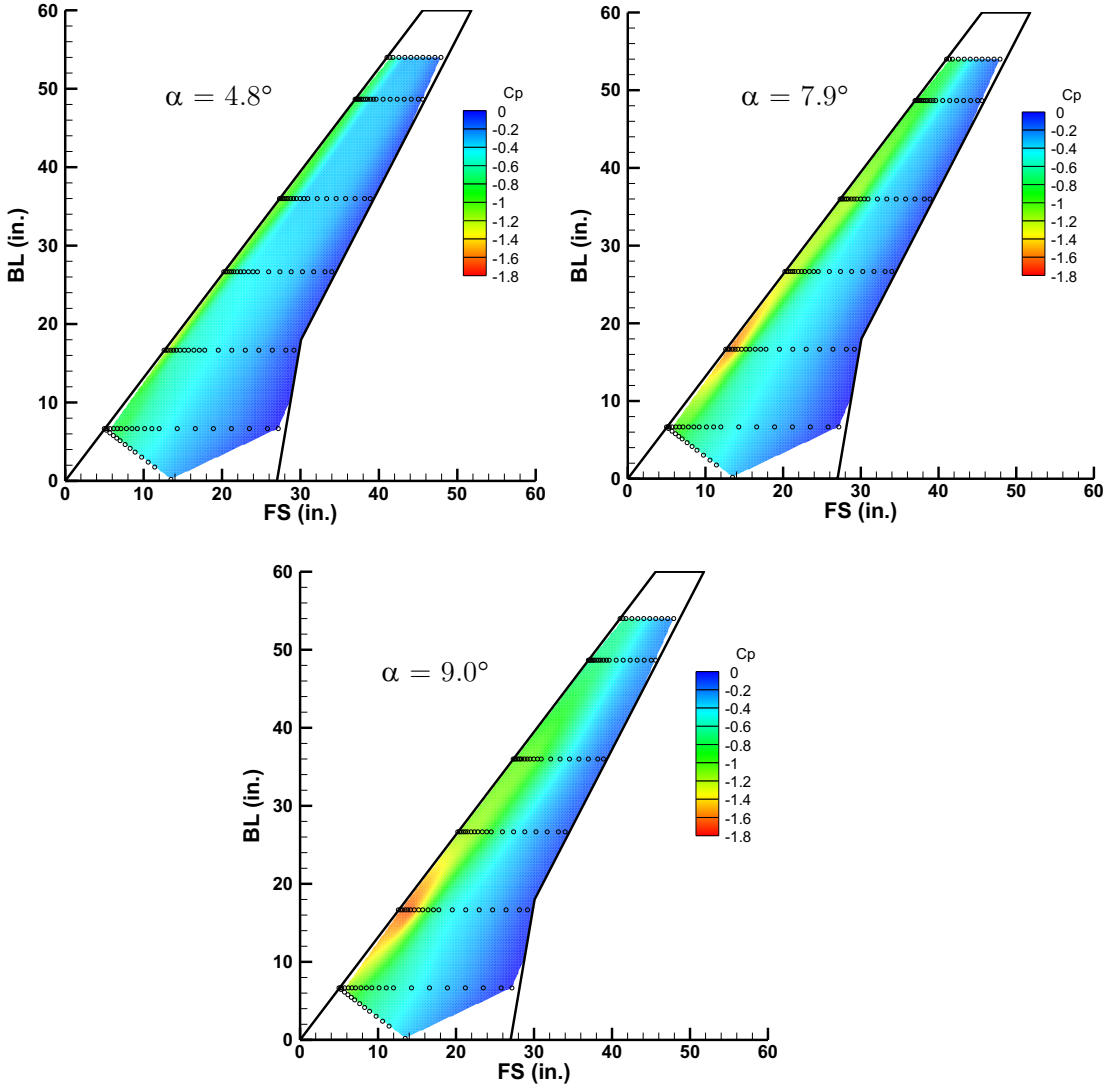

Fig. 3.29 2D smooth +grit Maximum Scallop configuration pressure contour plots at Re = 1.6 x 10^6 and M = 0.18 for α = 4.8°, 7.9°, and 9.0°, respectively.

At $\alpha = 4.8°$, a larger number of streamwise vorticies were present in the leading-edge flow than the 2D smooth Maximum Scallop configuration. This showed that the ice

shape roughness simulated by grit played a role in creating the streamwise vorticies. The leading-edge vortex and spanwise vorticies observed in the oil-flow visualization in Fig. 3.27 were also present in the pressure contour plots in Fig. 3.29 as an area of low pressure along the leading edge of the wing. The leading-edge vortex was still present and the reattachment line was visible in some areas between the streamwise vorticies. The oil accumulation indicating the "Secondary Separation" line was visible along the span of the wing in Fig. 3.27.

At $\alpha = 7.9°$, the streamwise vorticies were replaced with areas of separation which was similar to the changes in oil-flow visualization of the Streamwise configuration in Fig. 3.8 as the angle of attack was increased. The leading-edge vortex was also swept into the wake at approximately the 25% span location as indicated by an increase in spanwise oriented tufts in Fig. 3.28. As the leading-edge vortex was swept into the wake at the higher angles of attack, the areas of separation maintained higher amounts of suction at the leading edge of the wing than the trailing edge in Fig. 3.29. A few key separation areas emerged in Fig. 3.27 as dark areas where the increased shear forces pushed the oil away and the streamwise vorticies in the inboard 25% of the wing appeared to remain constant.

At $\alpha = 9.0°$, the leading-edge vortex was swept into the wake of the wing at about the 20% span location where a large dark area indicated flow separation in Fig. 3.27. This location corresponded to a sudden decrease in the suction at the leading edge of the wing in Fig. 3.29. A majority of the wing surface showed spanwise flow over the area after the leading-edge vortex was swept into the wake in Fig. 3.28 as spanwise oriented tufts. Although there were some key differences in the oil-flow visualization between the 2D smooth + grit and 2D smooth Maximum Scallop configurations, their pressure contour plots and fluorescent mini-tuft visualization results were similar. Therefore, the detailed

differences seen in the oil-flow visualization between the two low-fidelity ice shapes were not captured in the pressure contour plots or fluorescent mini-tuft data.

Chapter 4 Summary, Conclusions, and Recommendations

4.1 Summary

A method to create and fabricate full-span, artificial ice shapes from limited experimental ice shape accretion data was developed and applied for low Reynolds number wind tunnel testing. Ice accretion data were obtained from previous icing wind tunnel tests for sections of the CRM65 wing geometry in the NASA Glenn Research Center IRT using hybrid models. Hybrid models are wing section models of the CRM65 that retained a full-scale leading edge but included a truncated aft section that was designed to maintain the same leading-edge flowfield and ice accretion properties as the full-scale geometry. Ice accretion data from these tests were digitally documented and post-processed so an interpolation and extrapolation process could be applied to create a full-span, high-fidelity artificial ice shape. The full-span, high-fidelity artificial ice shape was scaled to fit the removable leading of an 8.9% scale CRM65 wing and merged to create a solid geometry for rapid prototyping. This process was repeated for a variety of ice accretion categories to capture as many ice accretion features as possible for aerodynamic testing. These differences in geometry were used to determine how high-fidelity ice shape features affected the aerodynamic performance of the swept-wing model. Low-fidelity versions of the full-span, high-fidelity artificial ice shapes were created to determine how much fidelity was required to obtain the same flowfield as the high-fidelity artificial ice shapes. 60-grit silicon carbide was adhered to the low-fidelity models to simulate ice shape roughness. Aerodynamic performance testing of the high- and low-fidelity ice shapes was conducted for Reynolds numbers of 0.8 x 10^6, 1.6 x 10^6, and 2.4 x 10^6 which correspond to Mach numbers of 0.09, 0.18, and 0.27. Angle of attack sweeps

ranged from -6° to 16°. Force balance, surface pressure, and mini-tuft visualization data were collected and after a review of these data, oil-flow visualization data were collected for a subset of the artificial ice shape configurations. Oil-flow visualization, pressure contour plots, and force balance data were summarized for the clean wing and a Reynolds number and Mach number comparison was presented. The differences and similarities between the flowfields and aerodynamic data for the low- and high-fidelity versions of the Maximum Scallop and Streamwise ice shapes were determined using the available data.

4.2 Conclusions

The objectives of this work were to develop a method for creating full-span ice shapes from a limited set of experimental data and to compare how ice shape fidelity affected the aerodynamics of a scaled, swept-wing model at low Reynolds numbers. Conclusions from analysis of the low-Reynolds number wind tunnel test results were:

1. The interpolation and extrapolation method created a repeated ice shape pattern.

    a) A method was developed to produce representative, at least qualitatively, full-span high-fidelity ice shapes from limited experimental data.

    b) The experimental data accounted for approximately 3 ft of the 56 ft wing of the CRM65 so about 53 ft of the leading edge was created from averages of extremely similar ice shape geometries.

    c) Repeated patterns in the streamwise vorticies were observed in the oil-flow visualization of the iced leading edge configurations.

2. Reynolds number and Mach number changes did not have a significant effect on the aerodynamic performance of the set of ice-leading edges tested.

3. The flow visualization techniques conducted did not provide a comprehensive view of the flow features.

a) Leading-edge vortex features on the clean wing were inferred to be in areas of oil swept away by high shear forces near the leading edge of the wing.

b) The high-fidelity Max-Scallop ice shape did not produce a leading-edge vortex visible in the oil-flow visualization. This may have been due to the streamwise vortices generated by the high-fidelity ice shape.

4. Low-fidelity ice shapes did not produce a conservative simulation of a high-fidelity ice shapes.

a) Low-fidelity ice shapes over-predicted the lift generated by the high-fidelity ice shapes.

b) Simulating ice shape roughness by adding grit to a low-fidelity ice shape did not significantly alter the force balance data even though it produced some different flowfield features.

c) Flowfield differences were observed between low- and high-fidelity ice shapes may account for these differences.

4.3 Recommendations

The following recommendations summarize ways to improve the testing and analysis of the iced leading edges used for these tests:

1. Improve analysis of flowfield features to increase our understanding of the flow and aerodynamics of ice shape simulations.

a) Improve current flow visualization techniques or implement new methods to better capture flow features.

b) Wake survey results may provide more insight to the presence of specific flowfield features not visible in the oil-flow or fluorescent mini-tuft visualization.

c) The locations where the leading-edge vortex was swept into the wake of the wing and other areas of flow separation were inferred from the visualization techniques but wake survey data would be able to confirm these results.

2. Compare low-fidelity results to high-fidelity results for other ice shape geometries.

a) Not all the low-fidelity results were compared to the high-fidelity results in this thesis due to the similarity of the data collected between the many configurations.

b) Further exploring the effects of fidelity may help design other low-fidelity ice shapes in the future.

3. Compare other techniques for creating low-fidelity ice shapes.

a) The 2D smooth and 2D smooth + grit low-fidelity ice shapes did not produce a conservative estimate for the high-fidelity configuration.

b) The 2D smooth and 2D smooth + grit low-fidelity ice shapes did not produce similar streamwise vorticies to those observed in the high-fidelity ice shapes.

c) The effect of the streamwise vorticies on the aerodynamic performance of the swept-wing model should be explored using other methods for creating low-fidelity ice shapes. If the flowfield is better understood including the role of the streamwise vortices, simple geometric variation spanwise may be able to be used to better reproduce the high-fidelity flowfield and thus the aerodynamic performance.

4. Conduct high Reynolds number wind tunnel testing for the same ice shapes to understand how Reynolds number and Mach number influences the effects of ice shape fidelity on the aerodynamics of a swept wing.

Appendix A Post Processing Laser Scanned Ice Shape Data

The raw ice shape laser scan data were initially digitally documented as millions of data points. This format was determined by Geomagic Studio [15] which was used to collect the data from the Romer Absolute system [14]. This appendix will describe the process used to transform these data point clouds into a single mesh surface.

The first step was to align each separate data scan. Each ice shape was scanned in multiple overlapping sections because the Romer Absolute system [15] was not able to scan the entire ice shape geometry at once and to ensure there were no gaps between each scanned section. The series of scans were aligned using the "Global Registration" function in the Alignment tools. This function is shown in Fig. A.1. An example of an ice shape scan before and after the "Global Registration" process can be seen in Fig. 2.16.

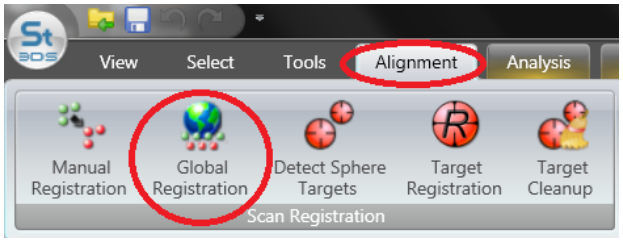

Fig. A.1 "Global Registration" function.

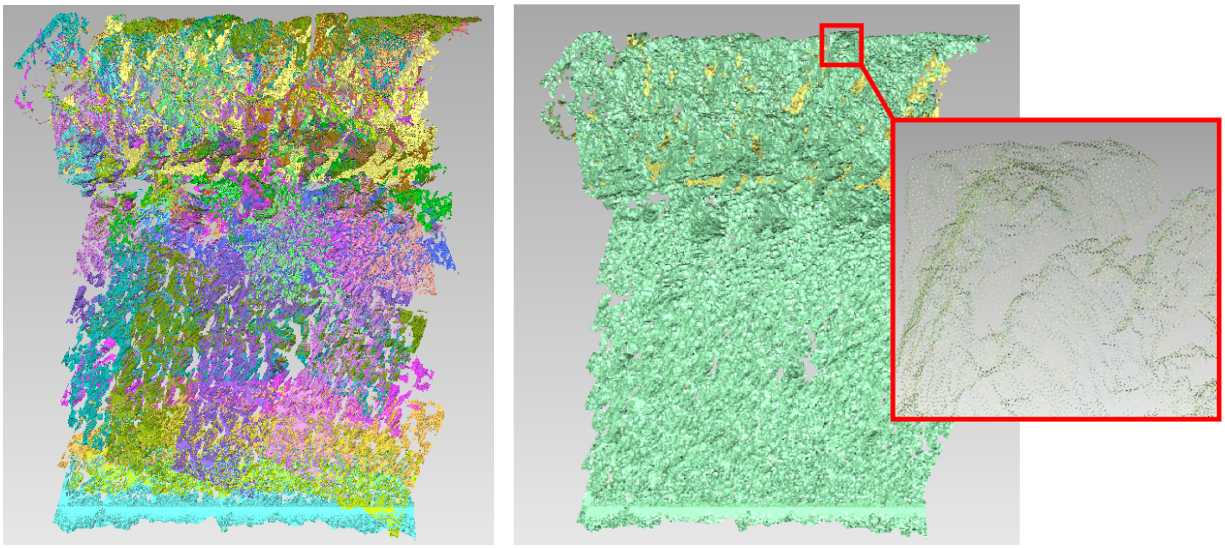

a) *b)*

Fig. 2.16 a) Raw ice shape laser scan data b) Reduced and evenly distributed data points of ice shape geometry.

Next, the separate scans must be combined in a way that removes overlapping data. The "Combine Point Objects" function in the Points tools was used to achieve this by making sure the "Remove Overlap" and "Retain Normals" options were selected. This function is shown in Fig. A.2.

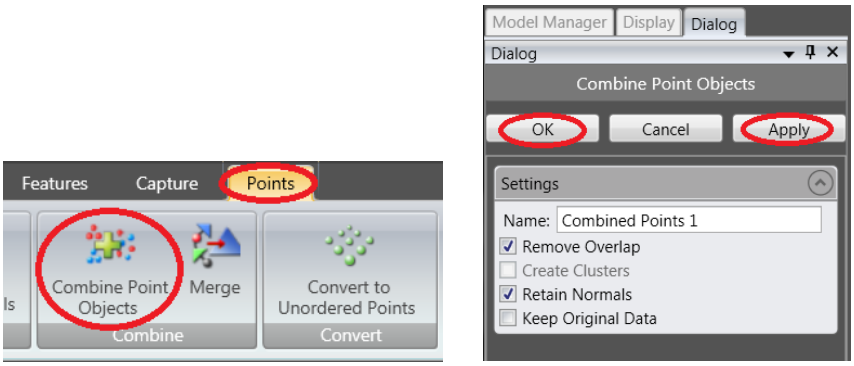

Fig. A.2 "Combine Point Objects" function.

At this point, the data point set still contained millions of points which needed to be reduced. The computing capabilities used for this research were unable to use this many data points for the morphing process described in Chapter 2 and Appendix B to create a full-span ice shape and standard graphics cards could not render the geometries quickly.

Furthermore, because the end goal for these ice shapes was to rapid prototype them, the high level of detail available with millions of data points was unnecessary due to the precision capabilities of rapid prototyping machines. Therefore, the number of data points were reduced and distributed evenly across the geometry of the ice shape. This was done using the "Uniform" function in the Points tools. This function is shown in Fig. A.3. The spacing of the data points was defined by a reduction target of 1,000,000 data points.

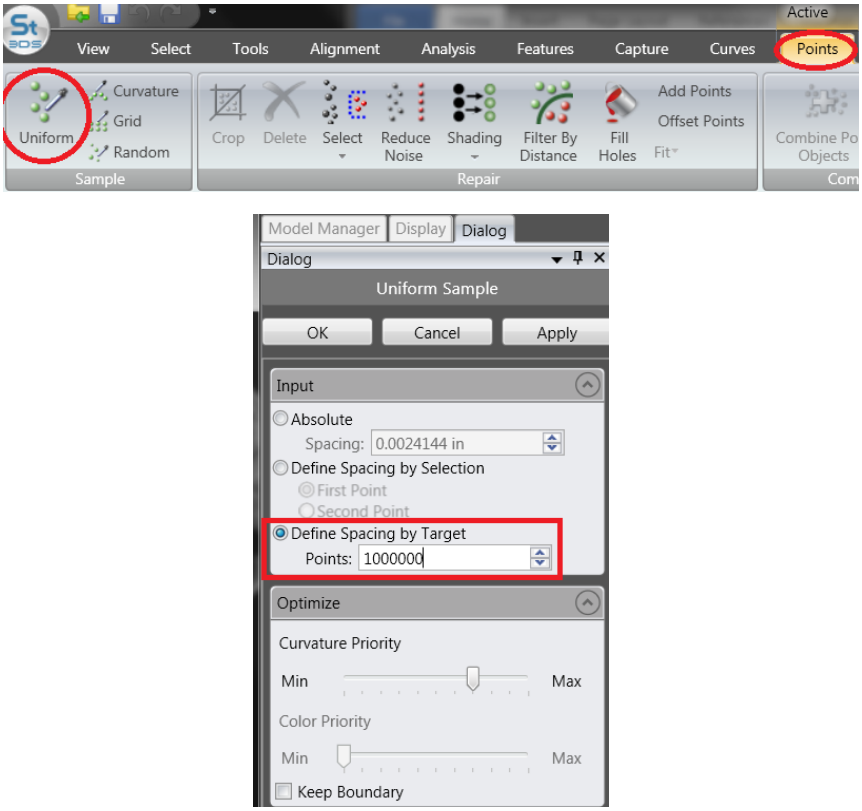

Fig. A.3. "Uniform" data points function.

Then, a triangular mesh surface was created from the uniform set of data points using the "Wrap" function in the Points tools. To ensure as much ice shape detail as possible was captured in the surface creation, no noise reduction was applied and small components were not deleted. The maximum number of triangles was set to 2,500,000 for the same

reasons that the number of data points was reduced. This function is shown in Fig. A.4. An example of an ice shape triangular mesh surface is shown in Fig. 2.17.

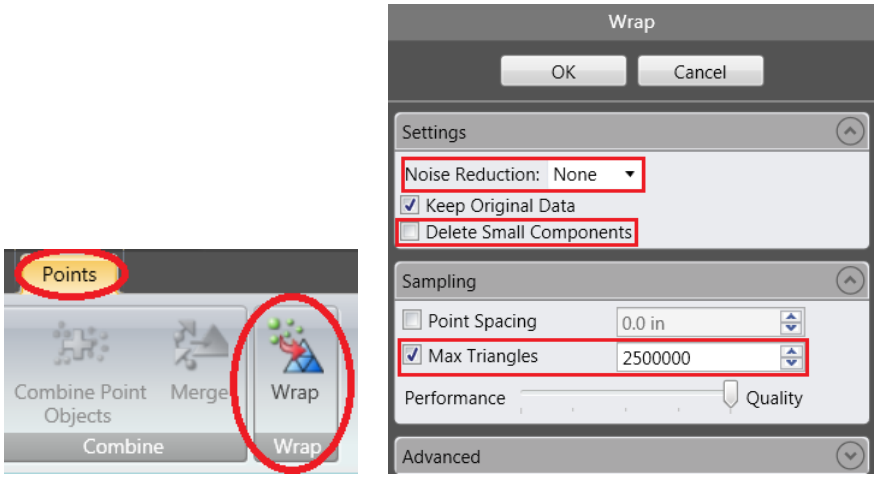

Fig. A.4 "Wrap" function to create a triangular mesh surface.

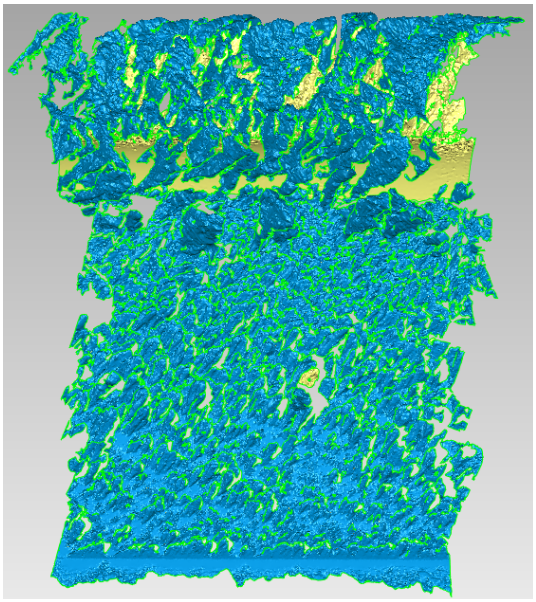

Fig. 2.17 Triangular mesh created from data points.

To apply the hole-filling process previously described in Chapter 2 to create a single mesh surface, the "Fill Single" function in the Polygons tools was used. Depending on the type of hole that needed to be filled a combination all three hole-filling types were used. For all holes filled, the "Tangent Mesh" option was used to create a smooth transition between the existing ice shape meshes. The "Fill Single" function is shown in Fig. A.5.

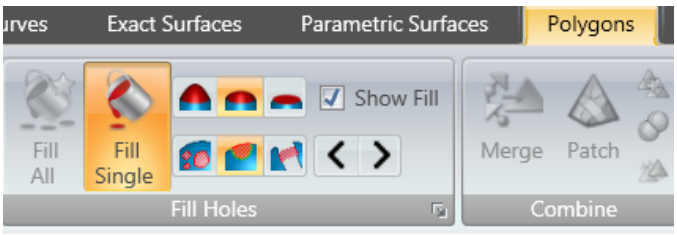

Fig. A.5 "Fill Single" function.

Finally, once all the gaps in the triangular mesh surface were filled, other small defects were fixed using the "Mesh Doctor" function in the Polygons tools. This tool identified and removed imperfections. The "Highly Creased Edges" and "Spikes" were not removed because it was discovered that they generally removed important ice shape features such as roughness. After this step, the ice shape was a single, water-tight surface. This function is shown in Fig. A.6.

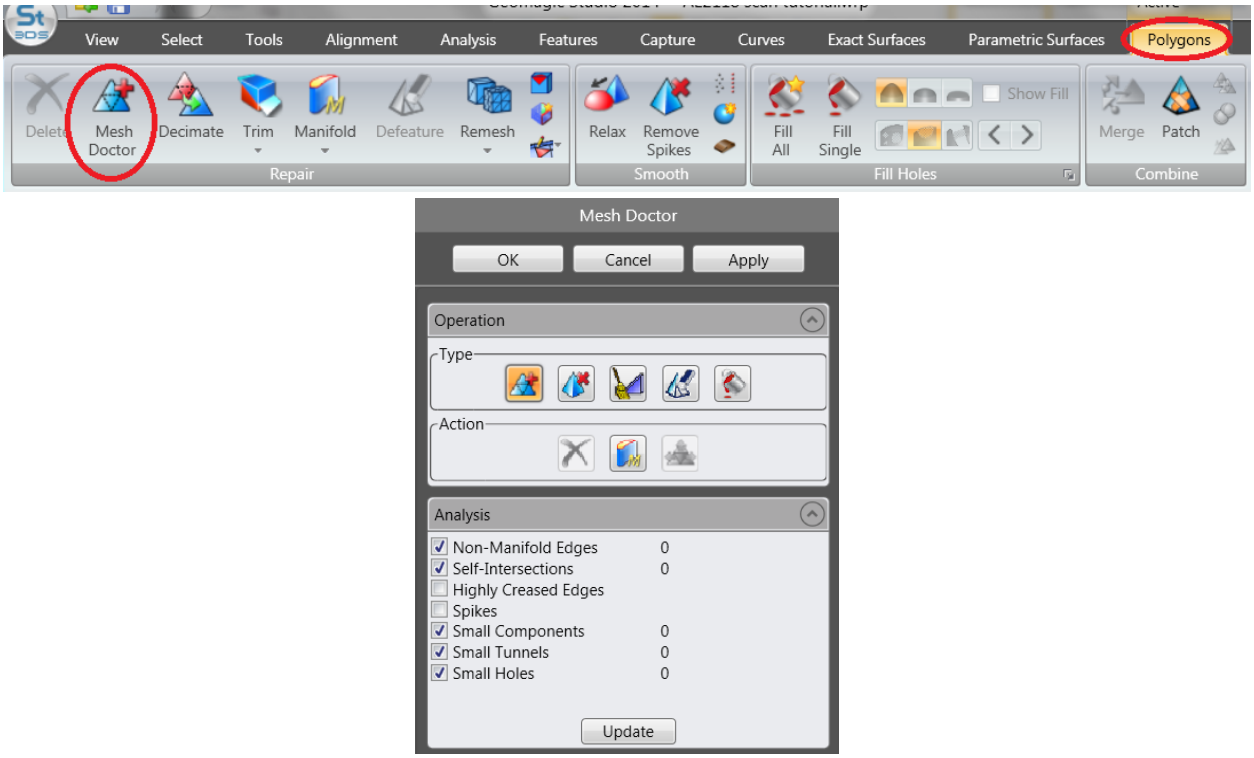

Fig. A.6 "Mesh Doctor" function.

Appendix B Ice Shape Interpolation Process

To create ice shape geometries between the post-processed, water-tight Inboard, Midspan, and Outboard stations of the leading edge of the CRM65, an interpolation method was developed. For this example, a Midspan ice shape, labeled here as "1", and an Outboard ice shape, labeled here as "15" was used. The 13 ice shape geometries between the Midspan and Outboard ice shapes were created using the following process. First, the two post-processed, water-tight ice shapes were loaded into the same file and both moved to the origin location using the "Move - to Origin" option in the "Tools" section shown in Fig. B1 so they would be aligned. Fig. B.2 shows an aligned Inboard and Outboard ice shape. The outer surface of the Outboard ice shape is shown in blue while the inner surface of the Outboard ice shape is shown in yellow because it is selected in Fig. B.2. The Midspan ice shape is shown in grey because it is not selected in the "Model Manager".

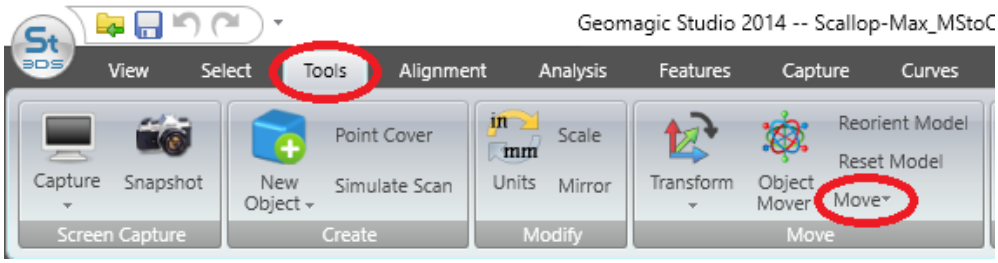

Fig. B.1 "Move – to Origin" function in the "Tools" section.

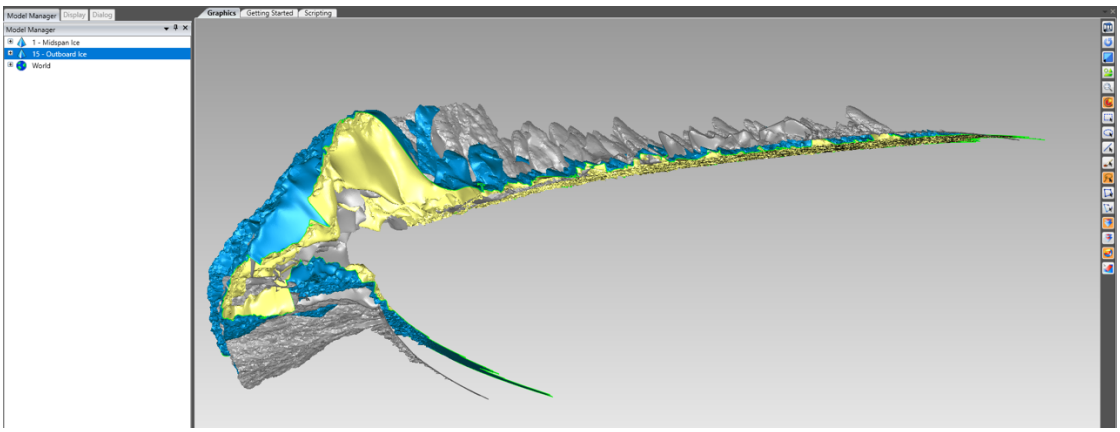

Fig. B.2 Aligned Inboard and Outboard ice shapes at origin.

To create the first interpolated ice shape, 4 copies of the Midspan ice shape were created in the "Model Manager". This is shown in Fig. B.3.

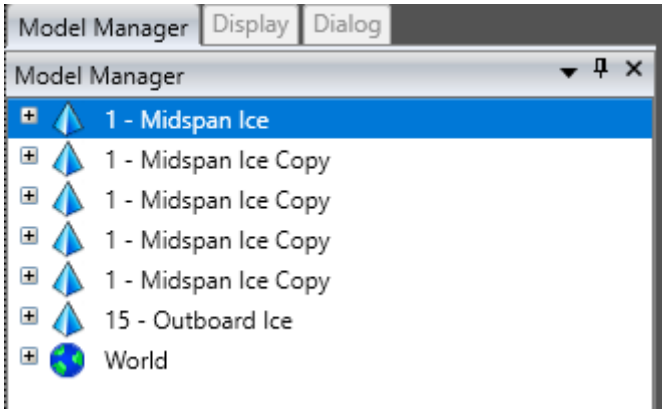

Fig. B.3 Copies of the Midspan ice shape for interpolation.

The 5 Midspan ice shapes and the one Outboard ice were selected and the "Average" function in the "Polygons" section was applied to create the first interpolated ice shape. The "Average" function applied to all the ice shape geometries is shown in Fig. B.4.

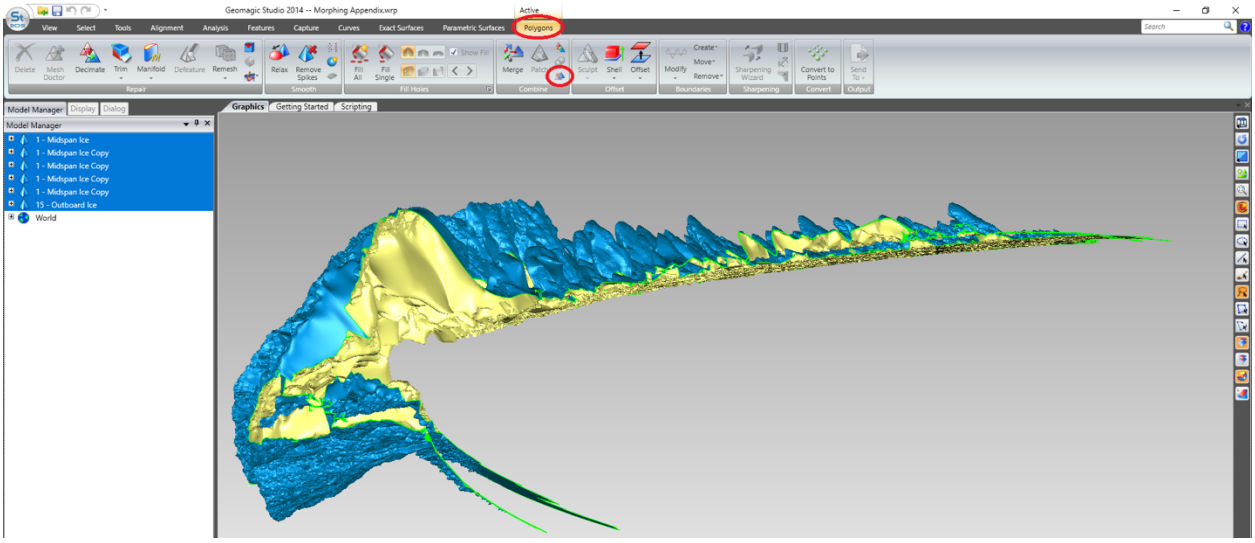

Fig. B.4 Application of "Average" function to Midspan ice shape copies and Outboard ice.

In the options for the "Average" function, the first interpolated ice shape was renamed to "2" since it was the closest in geometry to the Midspan ice shape which has been labeled as "1" for this interpolation example. Make sure to "Apply" the average then exit the options with "Ok".

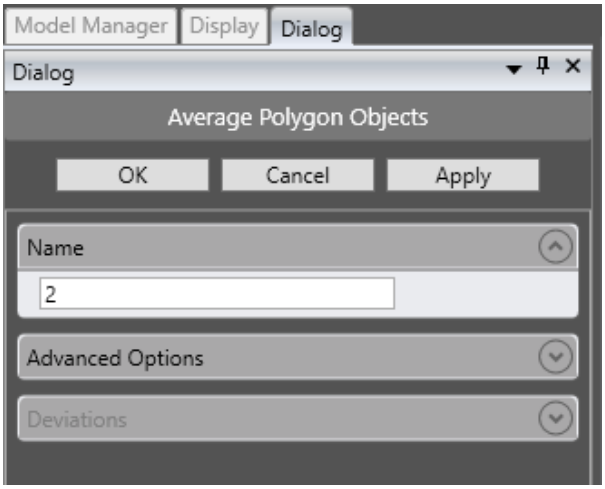

Fig. B.6 "Average" function options.

Once the "Average" function was applied, the new interpolated ice shape contained imperfections such as spikes or overlapping geometries. These were eliminated by using the "Mesh Doctor" function. The interpolated ice shape with imperfections is shown in Fig. B.7.

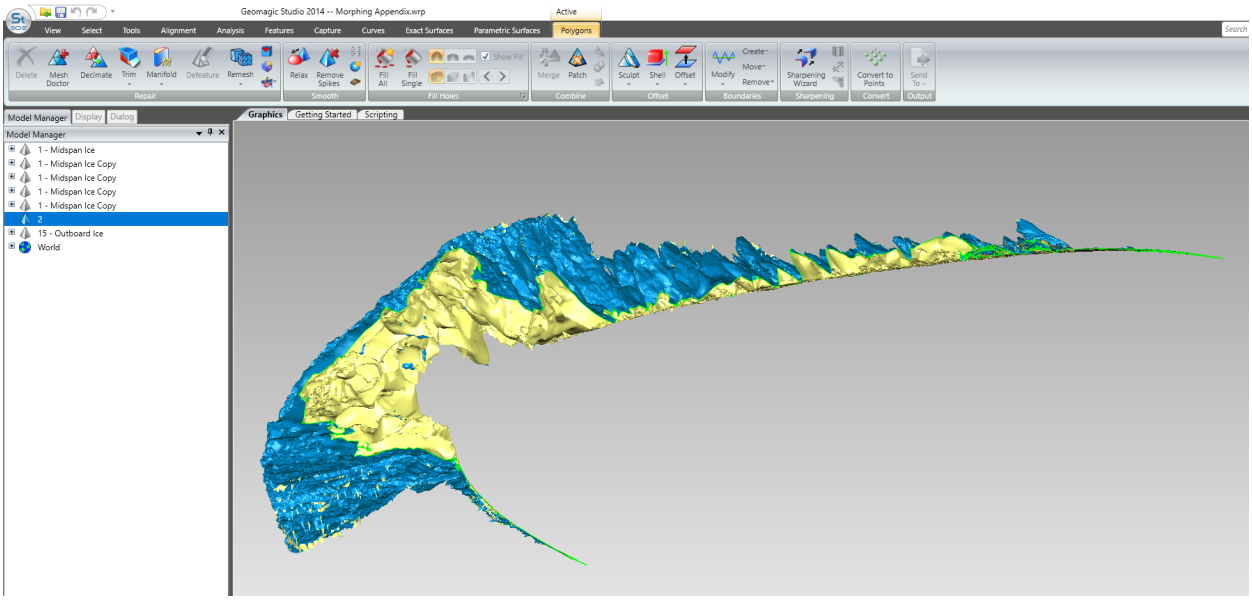

Fig. B.7 Interpolated ice shape before the "Mesh Doctor".

In the options for the "Mesh Doctor" the "Analysis" lists each imperfection on the interpolated ice shape which are now highlighted in red on the ice shape in Fig. B.8. In the type of operation applied section, select the "Automatic" removal and repair and apply the "Mesh Doctor. Repeat the "Mesh Doctor" process until there are no imperfections listed as shown in Fig. B.9 and the ice shape is a water-tight surface.

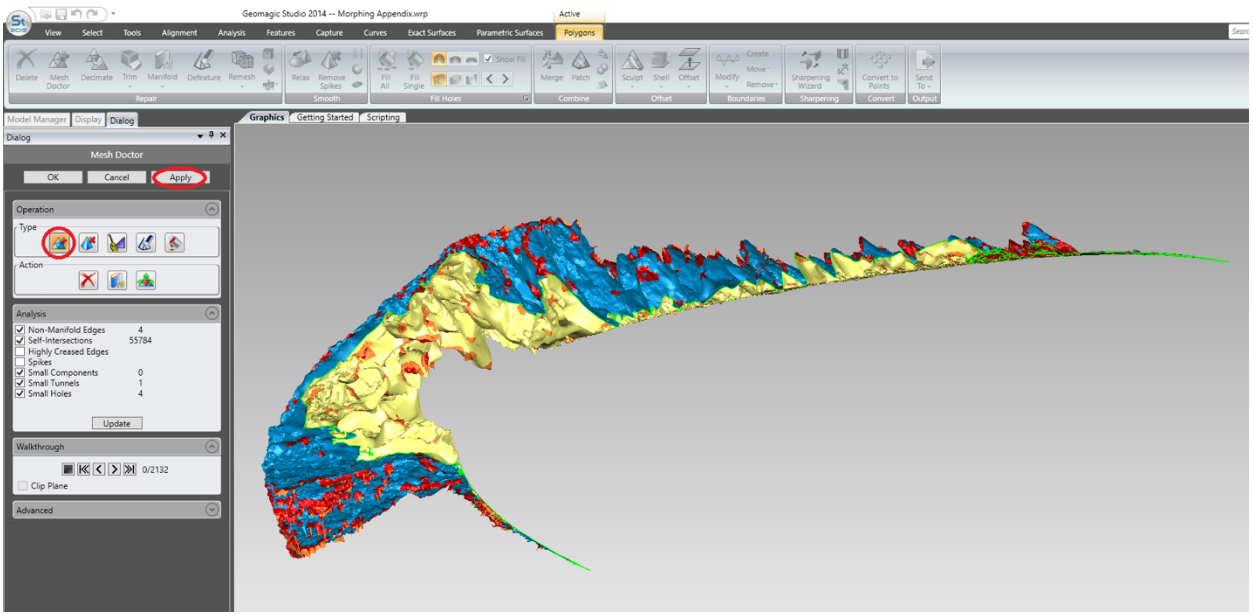

Fig. B.8 "Mesh Doctor" options.

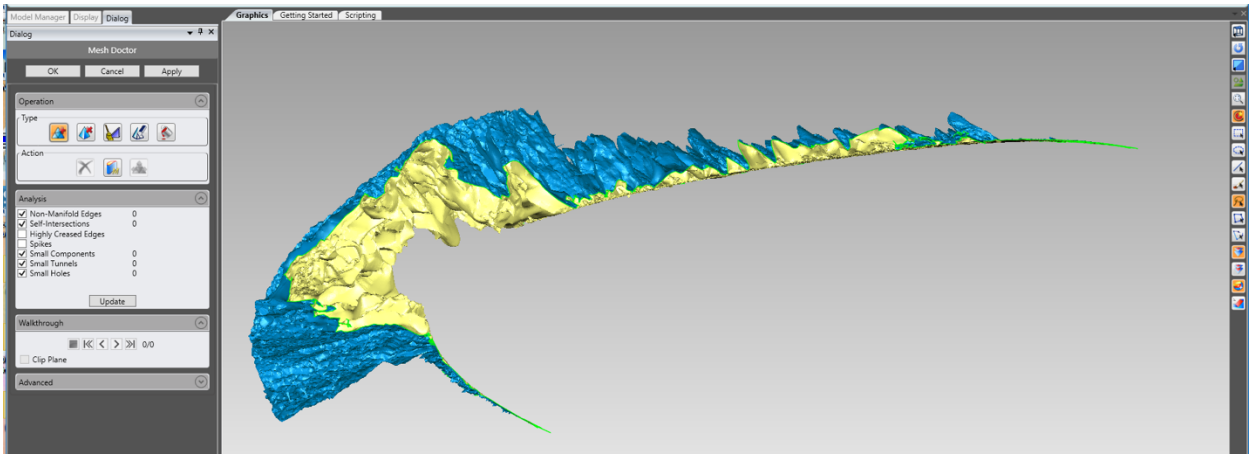

Fig. B.9 Water-tight ice shape surface after "Mesh Doctor" is applied.

At this point, the Midspan "1", "2", and Outboard "15" ice shapes should all be water-tight geometries. To create the second interpolated ice shape, which was named "14", 4 copies of the Outboard ice shape were averaged with 1 copy of ice shape "2" rather than the Midspan ice shape as shown in Fig. B.10. While this process may have produced errors, the averaging function in Geomagic was not accurate enough to create a unique ice shape geometry for each averaged ice shape along the leading edge of the wing using only the experimental ice accretion data.

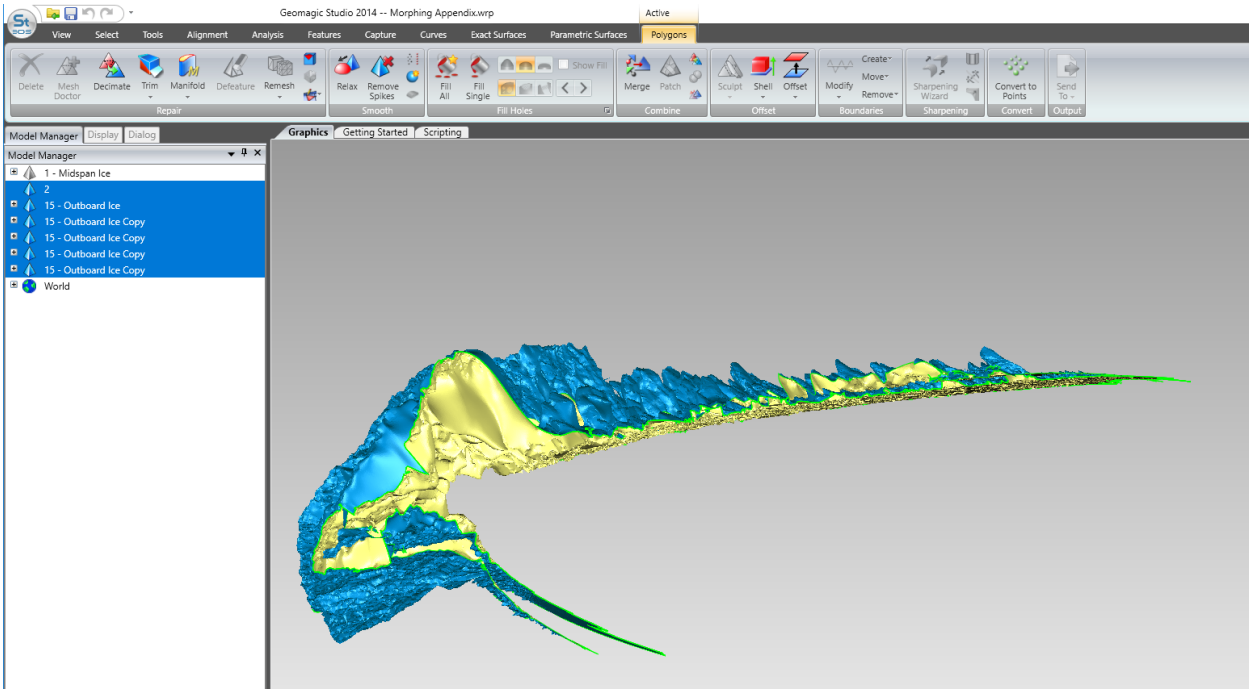

Fig. B.10 Ice shapes to average to create ice shape "14".

The "Mesh Doctor" function was then applied to ice shape "14" and the process was repeated until ice shapes 2-14 were created using the interpolation method. For example, to create ice shape "3", 4 copies of ice shape "2" were averaged with one copy of ice shape "14". Each ice shape was then placed using the leading edge of the CRM65 wing model as a guide with the "Object Mover" function in the "Tools" section. This function is shown in Fig. B.11. The interpolated ice shape pieces placed using the CRM65 leading edge as a guide is shown in Fig. B.12.

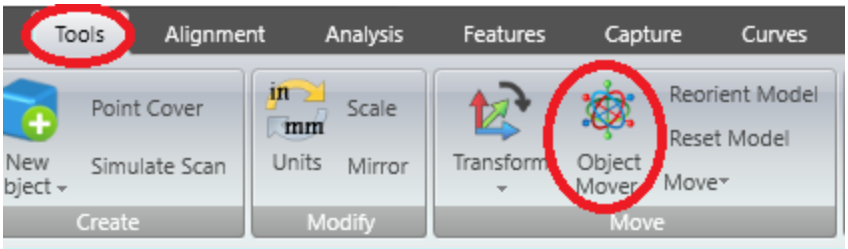

Fig. B.11 "Object Mover" function.

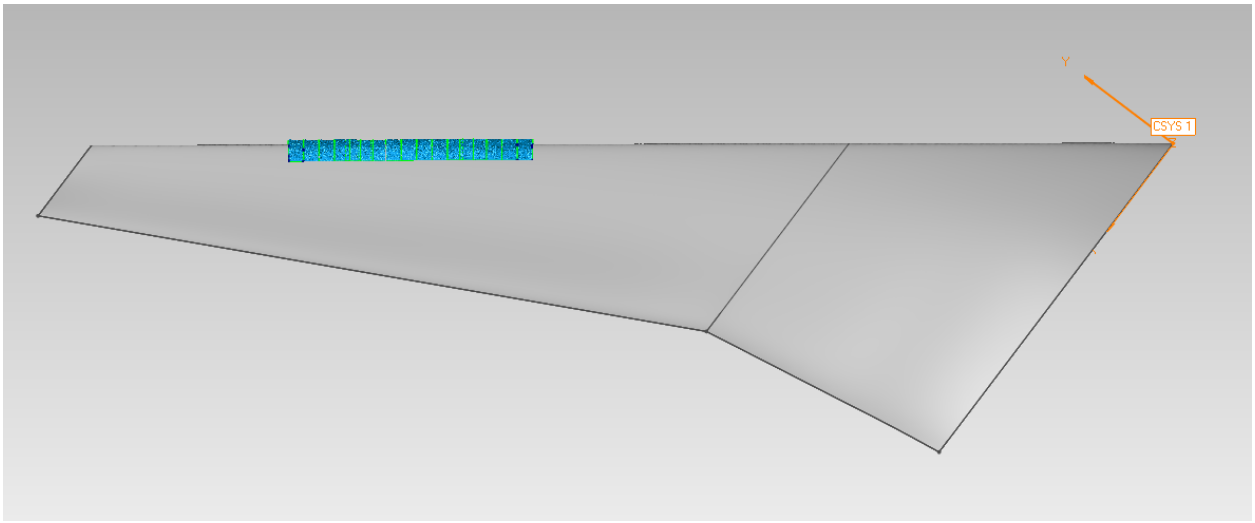

Fig. B.12 Interpolated geometries between the Midspan and Outboard ice shapes.

This entire process was repeated between the experimental ice shape data and the extrapolated wing root and wing tip ice shapes described in Chapter 2. Because each piece was interpolated and placed separately, this resulted in gaps between the ice shapes. These gaps were filled using the hole-filling functions described in Chapter 2 and Appendix A to create a full-span ice shape geometry.

Appendix C Ice Shape Fidelity Force Balance Data Comparisons

This appendix shows the force balance data for each high-fidelity ice shape compared to its corresponding low-fidelity ice shapes and the clean wing. Overall, most of the high-fidelity scalloped ice shapes had extremely similar force balance data results. The Streamwise and Small Gap Scallop high-fidelity configurations had results most similar to the clean wing. The Streamwise low- and high-fidelity configurations were chosen for a fidelity comparison because the force balance results showed differences in aerodynamic performance from the scalloped ice shape configurations while the Maximum Scallop low- and high-fidelity configurations were chosen for a fidelity comparison because they had the largest difference in geometry between the low- and high-fidelity ice shapes. Figures C.1 to C.5 were used to determine which ice shapes were compared in this thesis.

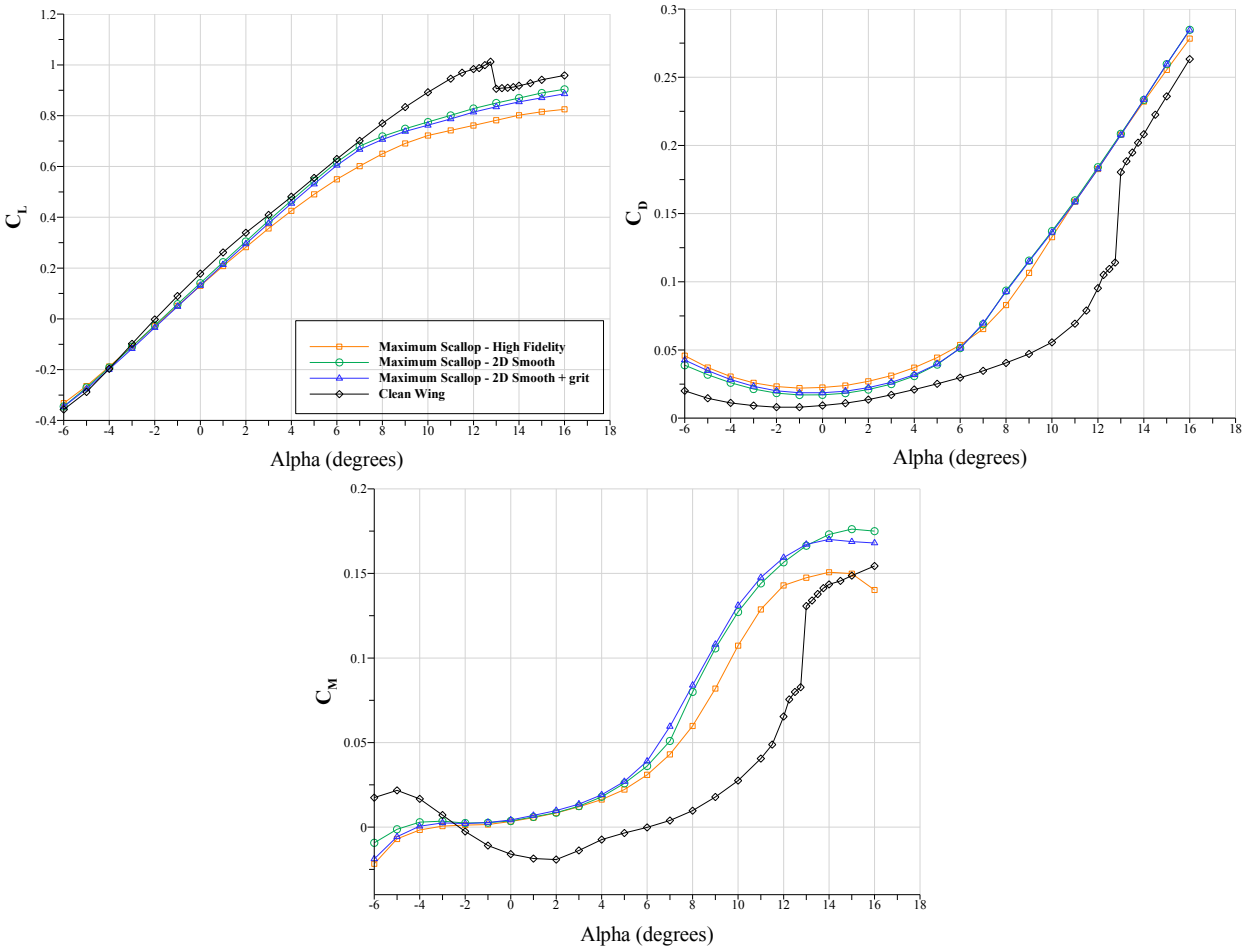

Fig. C.1 Force balance data for the 2D smooth, 2D smooth +grit, high-fidelity Maximum Scallop, and clean wing configurations for Re = 1.6 x 10^6 and M = 0.18.

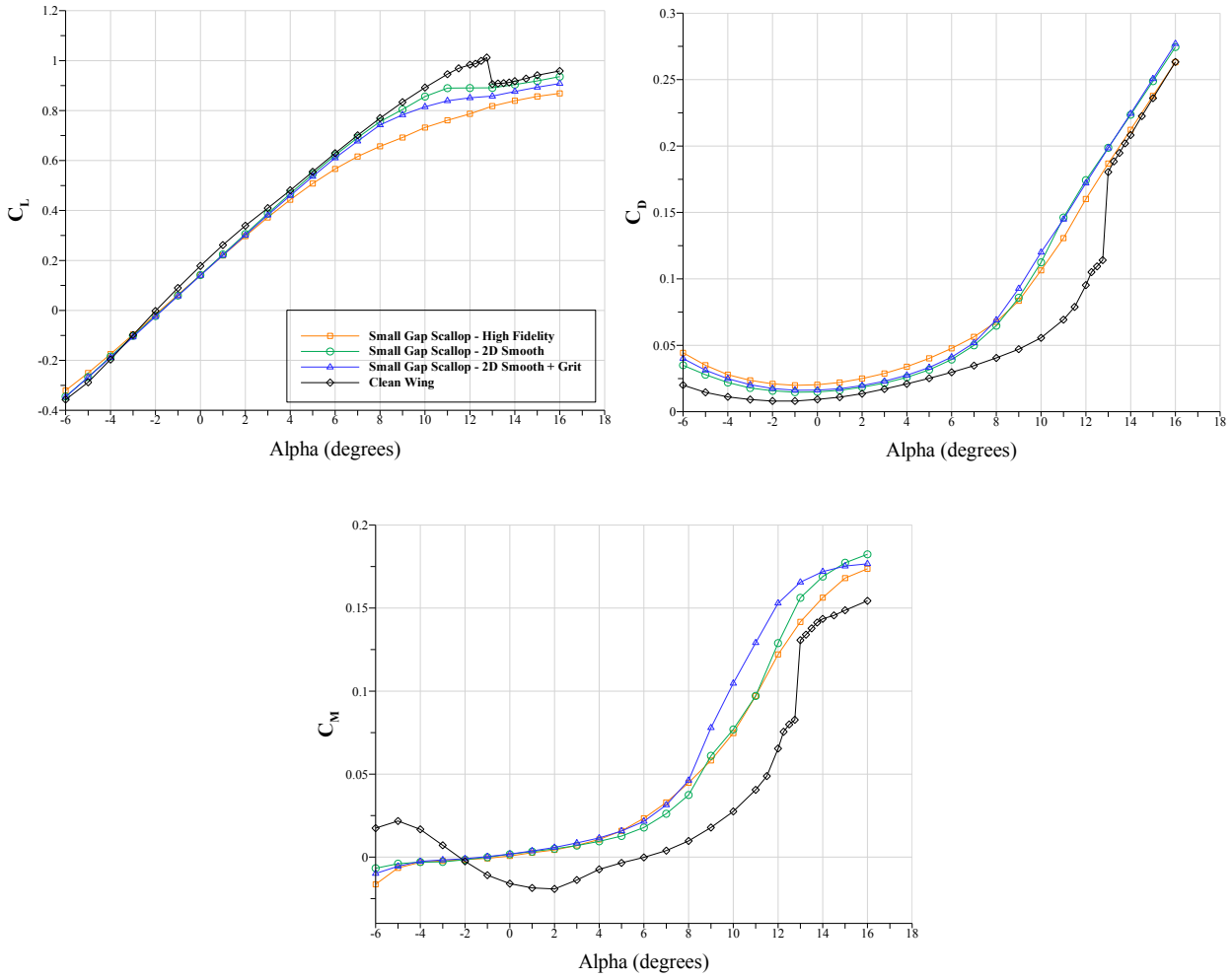

Fig. C.2 Force balance data for the 2D smooth, 2D smooth + grit, high-fidelity Small Gap Scallop, and clean wing configurations for Re = 1.6 x 10^6 and M = 0.18.

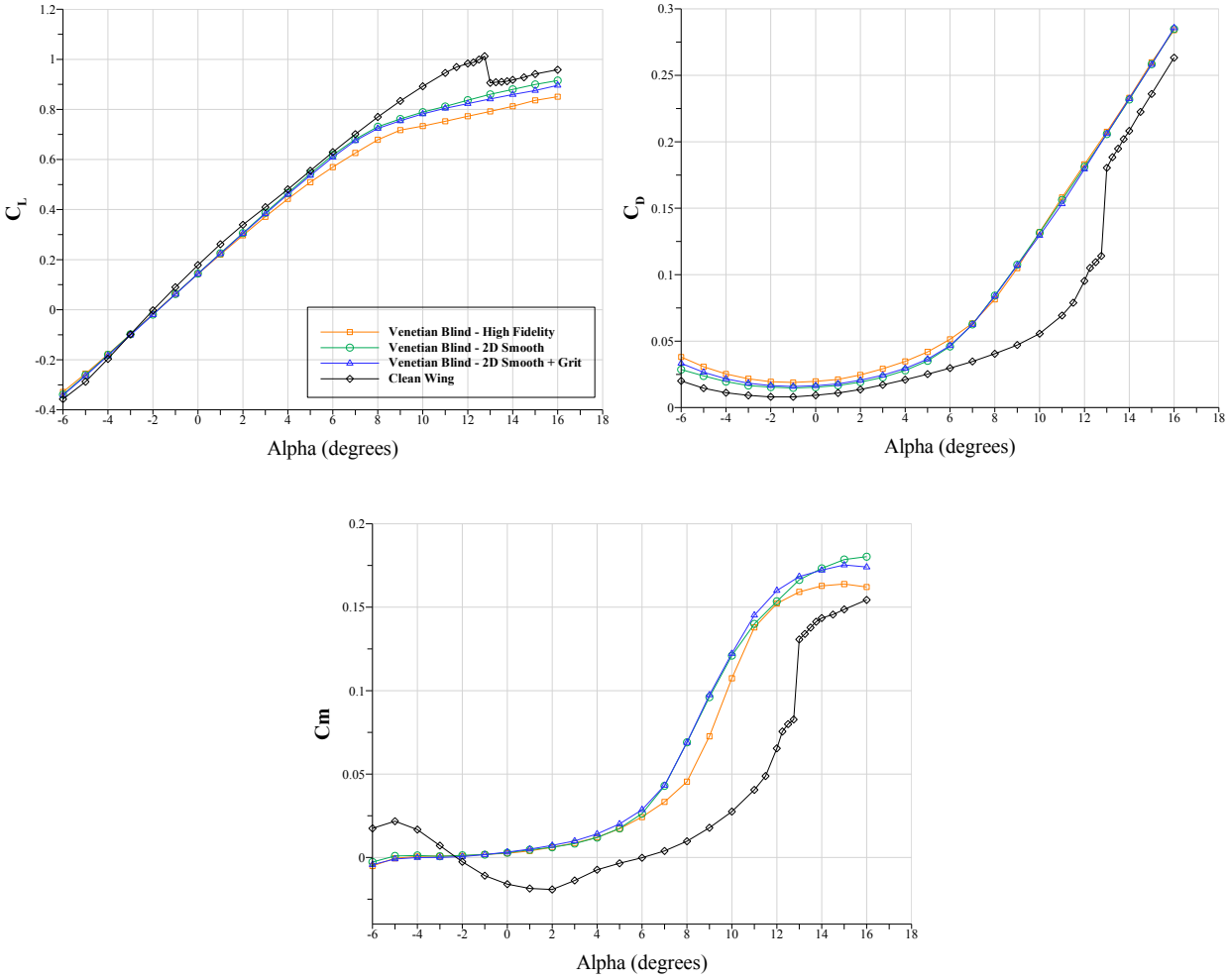

Fig. C.3 Force balance data for the 2D smooth, 2D smooth + grit, high-fidelity Venetian Blind, and clean wing configurations for Re = 1.6 x 10^6 and M = 0.18.

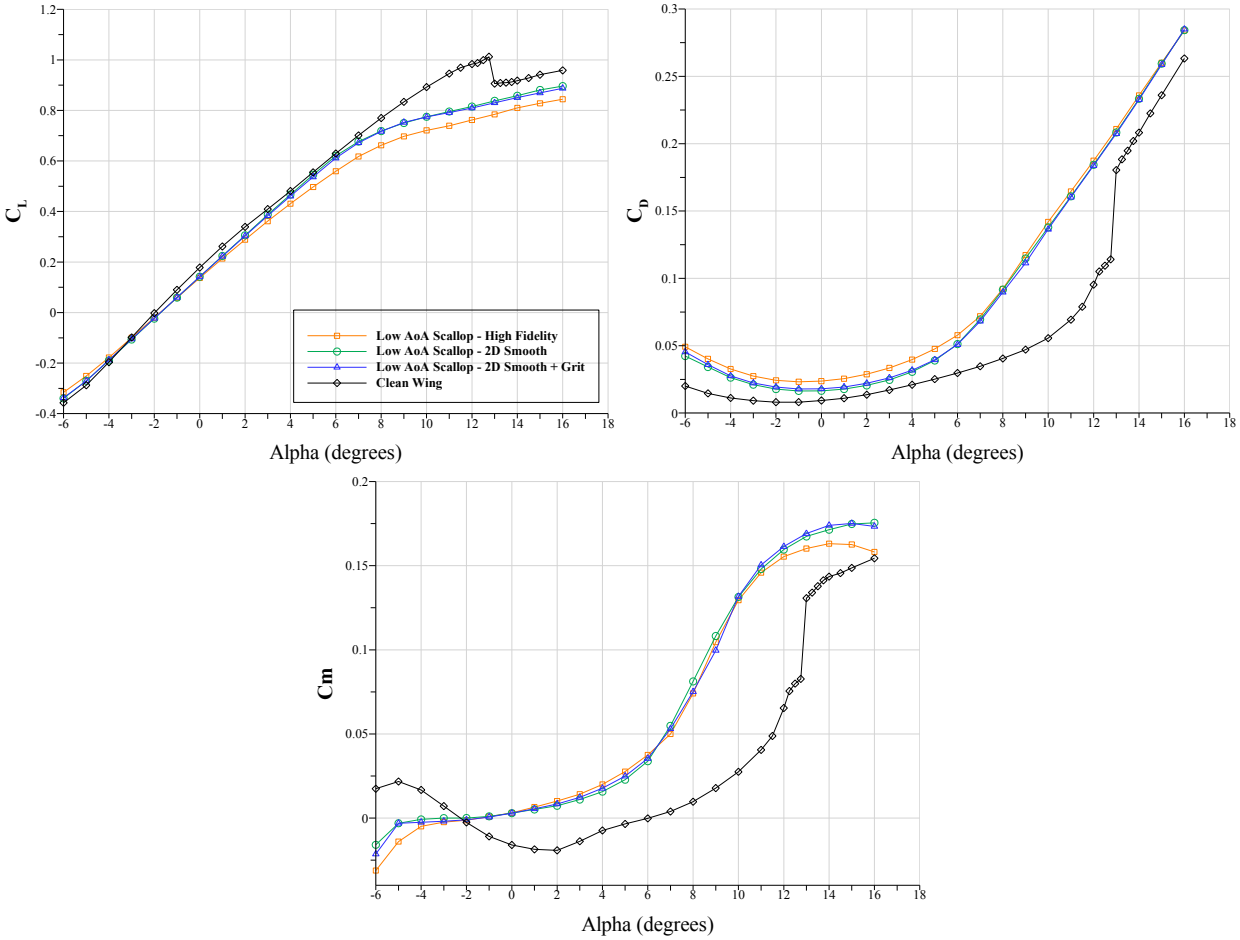

Fig. C.4 Force balance data for the 2D smooth, 2D smooth + grit, high-fidelity Low AoA Scallop, and clean wing configurations for Re = 1.6 x 10^6 and M = 0.18.

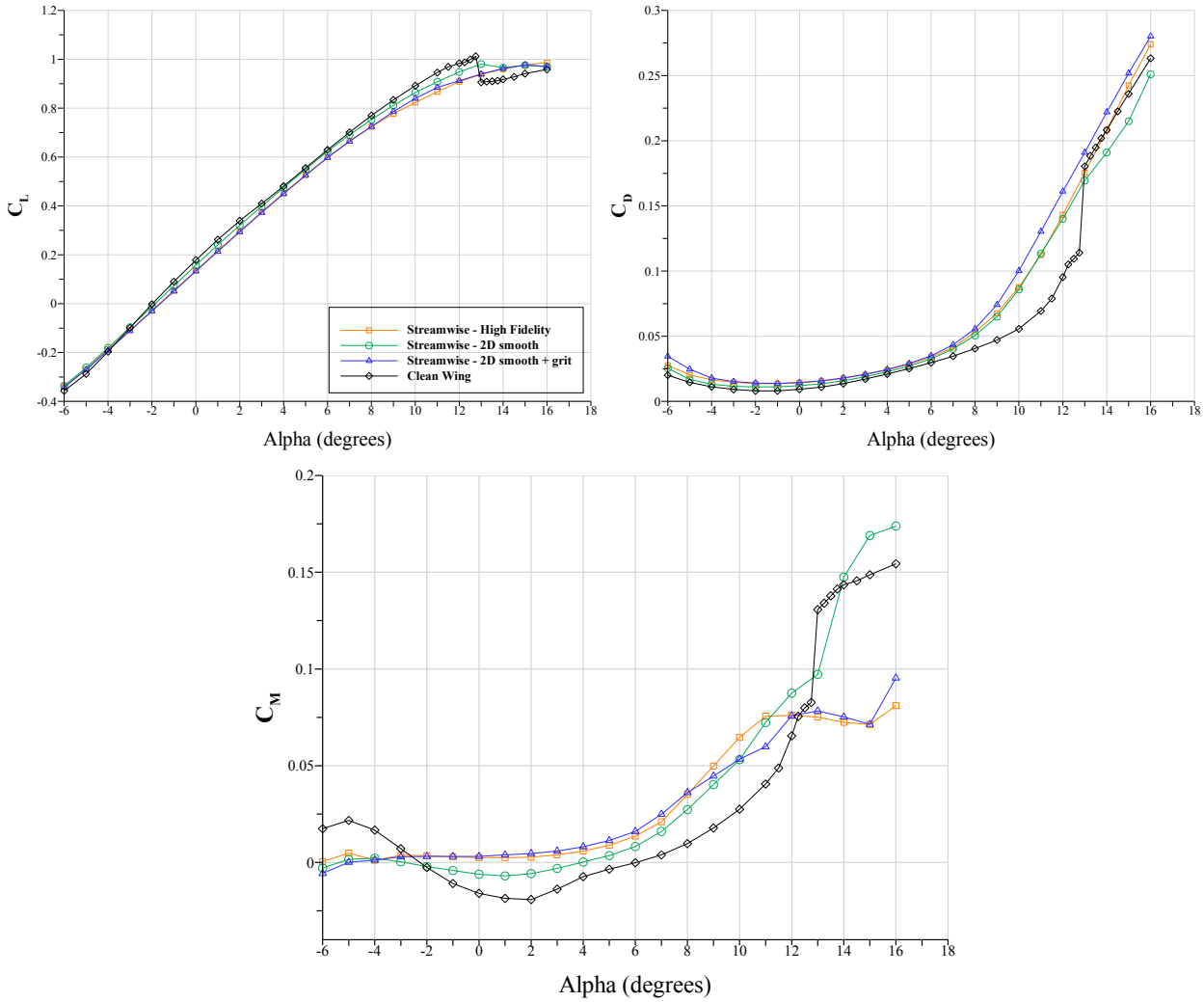

Fig. C.5 Force balance data for the 2D smooth, 2D smooth + grit, high-fidelity Streamwise, and clean wing configurations for Re = 1.6 x 10^6 and M = 0.18.

References

[1] Bragg, M.B., Broeren, A.P., Addy, H.E. Jr., Potapczuk, M.G., Guffond, D., Montreuil, E., "Airfoil Ice-Accretion Aerodynamics Simulation," AIAA Paper 2007-0085, January 2008, also NASA TM—2008-214830.
[2] Busch, G.T., "Experimental study of full-scale iced-airfoil aerodynamic performance using sub-scale simulations," Ph.D. thesis, Dept. of Aerospace Eng., Univ. of Illinois, Urbana, IL 2010.
[3] Broeren, A.P., Potapczuk, M.G., Riley, J.T., Villiedieu, P., Moens, F., Bragg, M.B., "Swept-Wing Ice Accretion Characterization and Aerodynamics," AIAA Paper 2013-2824, June 2013, also NASA TM—2013-216555, Sept. 2013.
[4] "NASA's Aeronautics Test Program: Icing Research Tunnel" URL: https://facilities.grc.nasa.gov/documents/TOPS/TopIRT.pdf
[5] "LEWICE 3D," NASA, URL: https://icebox.grc.nasa.gov/design/lewice3d.html
[6] Lee, S., Barnhart, B., and Ratvasky, T.P., "Dynamic Wind-Tunnel Testing of a Sub-Scale Iced S-B Viking," AIAA Atmospheric and Space Environments Conference, August 2-5, 2010, Toronto, Canada, AIAA Paper 2010-7986.
[7] Bosetti,C., Krueger, F.N., Gunter, I.M., and Walters, D., United States Patent Application Publication, US 2016/0076968A1, March 17, 2016.
[8] Broeren, A.P., Lee, S., Shah, G.H., and Murphy, P.C., "Aerodynamic Effects of Simulated Ice Accretion on a Generic Transport Model," SAE International Conference on Aircraft and Engine Icing and Ground Deicing, June 13-17, 2011, Chicago, IL, SAE Paper 2011–38–0065, NASA TM 2012-217246.
[9] Diebold, J., Broeren, A., and Bragg, M., "Aerodynamic Classification of Swept-Wing Ice Accretion," Atmospheric and Space Environments Conference: Aircraft Icing, American Institute of Aeronautics and Astronautics, 2013.
[10] Bragg, M.B., Broeren, A.P., and Blumenthal, L.A., "Iced-Airfoil Aerodynamics," Progress in Aerospace Sciences, Vol. 41, No. 5, Jul. 2005, pp. 323-418.
[11] Monastero, M., "Validation of 3-D Ice Accretion Documentation and Replication Method Using Pressure-Sensitive Paint," MS Thesis, Dept. of Aerospace Engineering, Urbana, IL 2014.
[12] Lee, S., Broeren, A.P., Addy, H.E., Sills, R., and Pifer, E., "Development of 3D Ice Accretion Measurement Method," AIAA 4th Atmospheric and Space Environments Conference, New Orleans, LA, June 25-28, 2012, AIAA Paper 2012-2938.
[13] Reehorst, A.L. and Richter, G.P., "New Methods and Materials for Molding and Casting Ice Formations," NASA TM-100126, 1987.
[14] "Product Catalog: Romer Absolute Arm," Hexagon Metrology, URL: http://www.hexagonmi.com
[15] "Geomagic: Reverse Engineering Software," Geomagic®, URL: http://www.geomagic.com
[16] Bidwell, C.S., and Potapczuk, M.G., "User's Manual for the NASA Lewis Three-Dimensional

Ice Accretion Code (LEWICE3D)," NASA TM 105974, December 1993.
[17] Broeren, A.P., Potapczuk, M.G., Riley, J.T., Villiedieu, P., Moens, F., Bragg, M.B., "Swept-Wing Ice Accretion Characterization and Aerodynamics," AIAA Paper 2013-2824, June 2013, also NASA TM—2013-216555, Sept. 2013.
[18] Vassberg, J.C., DeHann, M.A., Rivers, S.M., and Wahls, R.A., "Development of a Common Research Model for Applied CFD Validation Studies," AIAA Paper 2008-6919, Aug. 2008.
[19] Rivers, M.B., Dittberner, A., "Experimental Investigation of the NASA Common Research Model," AIAA Paper 2010-4218, June 2010.
[20] Fujiwara, G. E., Bragg, M. B., Camello, S., and Lum, C., "Computational and Experimental Ice Accretions of Large Swept Wings in the Icing Research Tunnel", 8th AIAA Atmospheric and Space Environments Conference, AIAA AVIATION Forum, AIAA 2016-3734, June 2016. http://dx.doi.org/10.2514/6.2016-3734
[21] Anderson, D.N., "Manual of Scaling Methods," NASA CR-2004-21287.
[22] Tsao, J.C, Lee, S., "Evaluation of Icing Scaling on Swept NACA 00 Airfoil Models," NASA/CR, National Aeronautics and Space Administration, 2012.
[23] Fujiwara, G. E. C., Wiberg, B. D., Woodard, B., and Bragg, M., "3D Swept Hybrid Wing Design Method for Icing Wind Tunnel Tests", 6th AIAA Atmospheric and Space Environments Conference, AIAA AVIATION Forum, AIAA 2014-2616, June 2014. http://dx.doi.org/10.2514/6.2014-2616
[24] Broeren, A.P., Potapczuk, M.G., Lee, S., Malone, A.M. Paul, B.P. Jr., Woodard, B.S., "Ice-Accretion Test Results for Three Large-Scale Swept-Wing Models in the NASA Icing Research Tunnel," AIAA 8th Atmospheric and Space Environments Conference, Washington D.C., June 13-17, 2016.
[25] Camello, S.C., Lee, S., Lum, C., Bragg, M.B., "Generation of Fullspan Leading-Edge 3D Ice Shapes for Swept-Wing Aerodynamic Testing," AIAA 8th Atmospheric and Space Environments Conference, Washington D.C., June 13-17, 2016.
[26] Broeren, A.P., Bragg, M.B., Addy, H.E., Lee, S., Moens, F., and Guffond, D., "Effect of High-Fidelity Ice Accretion Simulations on the Performance of a Full-Scale Airfoil Model," 46th AIAA Aerospace Sciences Meeting and Exhibit, January 7-10, 2008, Reno, Nevada, AIAA Paper AIAA 2008-434.
[27] Woodard, B.S., Broeren, A.P., Diebold, J.M., Bragg, M.B., "Preliminary Assesment of Low-Reynolds Number Aerodynamics for a Swept Wing with Artificial Ice Roughness" (to be published)
[28] Diebold, J.M., Woodard, B.S., Camello, S.C., Bragg, M.B., "Effect of Ice Accretion of Full-Scale, Swept-Wing, Aerodynamic Performace and Control Effects," (to be published)
[29] "Product Data Sheet: Somos® NeXt," Somos®, URL: https://www.dsm.com/
[30] Pope, A., Rae, W.H., and Barlow, J.B., "Low-Speed Wind Tunnel Testing," John Wiley & Sons, Inc., 3rd ed., 1999.
[31] "Data Reduction System: Boundary Corrections," Walter H. Beech Memorial Wind Tunnel Engineering Process Description, 2014.

[32] Poll, D.I.A., “Spiral Vortex Flow Over a Swept-Back Wing,” Aeronautical Journal, May 1986.
[33] Harper, C.W., and Maki, R.L., “A Review of the Stall Characteristics of Swept Wings,” NASA TN D-2373 , July 1964.
[34] Diebold, J.M., “Aerodynamics of a Swept Wing with Leading-Edge Ice at Low Reynolds Number,” MS Thesis, Dept. of Aerospace Engineering, Urbana, IL 2012.
[35] Reeves, G., “Smooth2a,” Mathworks: File Exchange, 13 Mar 2009, https://www.mathworks.com/matlabcentral/fileexchange/23287-smooth2a
[36] Broeren, A.P., Addy, H.E. Jr., Bragg, M.B., “Flowfield Measurements About an Airfoil With Leading-Edge Ice Shapes,” AIAA 2004-0559
[37] Bragg, M.B., Broeren, A.P., Blumenthal, L.A., “Iced-Airfoil Aerodynamics,” Progress in Aerospace Sciences, Volume 41, Issue 5, Pages 323-362, July 2005.
[38]Papadakis, M., Yeong, H.W., Wong, S.C., Vargas, M., Potapczuk, M.G., “Aerodynamic Performance of a Swept Wing with Ice Accretions,” AIAA 2003-0731.
[39] Diebold, J.M., unpublished images.